Doctoral Dissertation

Structure-Dependent Electrical Conductance of Suspended Graphene Nanoribbon by In-situ Transmission Electron Microscopy Observation

Liu Chunmeng

Supervisor: Professor Yoshifumi Oshima

Graduate School of Advanced Science and Technology

Japan Advanced Institute of Science and Technology

[Materials Science]

September 2020

Abstract

Structure-Dependent Electrical Conductance of Suspended Graphene Nanoribbon by In-situ Transmission Electron Microscopy Observation

Liu Chunmeng

s1720432

In this thesis, the structure-dependent electronic properties of suspended graphene nanoribbons (GNRs) are investigated by in situ transmission electron microscopy (TEM) observation to obtain structural information and simultaneous current-voltage (I-V) curve measurements.

The suspended GNR devices are fabricated with the width from ca. 100 to 800 nm. After careful cleaning by current annealing, the suspended ribbon sculpt by convergent electron beam followed by a high bias annealing. During the thinning process, the measured I-V curves indicate that the electrical conductivity of ribbon change from metallic to semiconducting behavior, with the reduction of GNR width. When the width become very narrow (usually < 4 nm), the energy gap start to be opened. A transport gap of 300 and 700 meV is estimated for 1.5 nm wide AGNR and ZGNR, respectively. Most of important, the I-V curves for the zigzag edge GNRs (ZGNRs) are obviously different from those for the armchair edge GNRs (AGNRs) and mixture of both zigzag and armchair edges GNRs (MGNRs) as follows. (1) The ZGNRs showed a sharp increase at the threshold voltage in differential conductance-voltage curves. (2) The band gaps measured for ZGNRs were smaller than the band gaps calculated using the GW approximation. (3) The threshold voltage increased with the GNR length. These features support the previously simulated current-driven magnetic-insulator and nonmagnetic-metal nonequilibrium phase transitions by the application of a bias voltage.

In addition, we also carefully observe the restructure of monolayer and few layer GNRs under different applied bias voltage. When a stable 1.0 V bias voltage is applied on monolayer GNR, it only affect the edge structure; the rough and curve edge restructure into straight and smooth edge, without changing the width of ribbon. However, when the bias voltage is increased, it not only affect edge structure, but also width and layer number of GNR. Under a high bias voltage, the thickness and width of ribbon shrinks sharply with the edge restructure at the same time. Moreover, we found that the conductance improve by structure recrystallization during reconstruction process, even with the decrease of ribbon width.

In conclusion, our ability to fabricate ultra-narrow GNRs with controlled width, layer number and edge structure opens a door systematic investigation the structure dependent electrical property of GNR. The unique I-V characterization of narrow and short ZGNR represents the potential for further nanosized switching devices.

Keywords: structure-dependent electronic properties, suspended graphene nanoribbons, in-situ TEM observation, nonequilibrium phase transitions, restructure

Table of Contents

Abstract ..... **I**

Chapter 1 Background **1**

Introduction 1

1.1 Graphene and graphene nanoribbon 2

1.1.1 The basic introduction of graphene 2

1.1.2 Graphene nanoribbon and its electrical property 4

1.1.3 The preparation of graphene nanoribbon 8

1.2 Basis of transmission electron microscopy and characterization 9

1.3 The previous investigation of GNR: A brief review 12

1.4 Purpose and method of present research 16

1.5 Conclusion 17

Reference 19

Chapter 2 Experimental setup and sample preparation **24**

Introduction 24

2.1 Experimental setup 25

2.2 The design of in-situ TEM holder 26

2.3 The design of custom TEM chip 28

2.4 The fabrication of GNR device 29

2.4.1 List of equipment used for fabrication 29

2.4.2 The overall process of fabrication 34

2.4.3 Electrodes fabrication 36

2.4.4 Fabrication of nano-gaps on the electrode 40

2.4.5 Transfer and pattering of graphene 43
2.5 Characterization of fabricated GNRs 47
2.6 Conclusion 49
References 50

Chapter 3 Graphene cleaning methods 52
Introduction 52
3.1 Consideration on cleaning of graphene 53
3.2 Dry-cleaning with adsorbents 54
3.3 Two-step annealing in gas environment 58
3.4 Thermal annealing in vacuum 61
3.5 In-situ current induced-annealing 65
3.5.1 The damage of GNR under electron beam before cleaning 65
3.5.2 Current annealing process of GNR 66
3.5.3 The mechanism of in-situ current annealing 69
3.5.4 Finite element method simulation of suspended GNR devices 74
3.6 Conclusion 80
References 81

Chapter 4 Nano-sculpting and in-situ electrical measurement of graphene nanoribbons 84
Introduction 84
4.1 Rough nano-sculpting of the GNR device 85
4.2 Precise thinning process and I-V measurement of narrow GNR 88
4.2.1 The thinning process of GNR by applying a high bias voltage 88
4.2.2 In-situ I-V measurements during thinning process 90

4.2.3 Formation of ultra-narrow zigzag edge-graphene nanoribbon 92
4.2.4 Different configurations in GNR and simulated TEM images 94
4.3 Resistance measurement of GNR with different widths 97
4.4 Structure-dependent electronic properties of ultra-narrow AGNR and ZGNR 98
4.4.1 The electrical conductance properties of AGNRs 98
4.4.2 I-V curves for ultra-narrow ZGNRs 100
4.4.3 Interpretation of I-V curves for ZGNRs 103
4.5 Conclusion 107
References 108

Chapter 5 Restructure of graphene nanoribbon under bias voltage 113
Introduction 113
5.1 Edge recrystallization of monolayer GNR 114
5.2 Improvement of conductance for monolayer GNR during reconstruction 120
5.3 Layer sublimation and reorganization of few layer GNR 123
5.4 Conclusion 126
References 128

Chapter 6 Summary 130

Appendix A 133

Acknowledgements 136

List of Publications 138

Presentation 139

Chapter 1 Background

Introduction

The first chapter will introduce the mainly investigated topic of this thesis-graphene nanoribbon, and explains how to use in-situ transmission microscopy to study this material.

In Chapter 1.1, we introduce what is graphene and graphene nanoribbon, and how to make the ribbon. In Chapter 1.2, we show the construction and working principle of a transmission electron microscopy and explain how it works in this experiment. In Chapter 1.3, we give a brief overview of recent theoretical and experimental progress about the investigation of graphene nanoribbon. In Chapter 1.4, we show the mainly method and purpose in this thesis.

1.1 Graphene and graphene nanoribbon

1.1.1 The basic introduction of graphene

Graphene- a two dimensional (2D) allotrope of carbon- has attracted widely attention due to the unique properties and applications. It consists of one atom thick carbon film, which arranges in a honeycomb structure made out of hexagons, shown in Figure 1.1(a). Although it's the basic of other carbon materials: fullerenes, carbon tubes and graphite, it was discovered long time later after its invention. The reason is that, the limit of equipment to search for one-atom-thick flakes and no one believe graphene can stable exist in the free state.

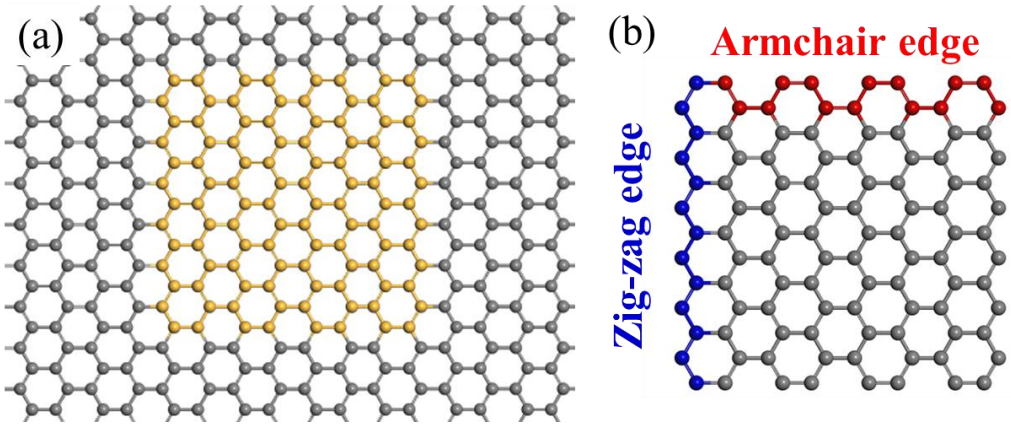

Figure 1.1 Models of graphene and graphene nanoribbon. (a) Graphene is 2D building materials for graphene nanoribbon by cutting the main crystallographic axis. The yellow part indicate the obtained ribbon. (b) Graphene nanoribbon along zigzag (blue color) or armchair (red color) directions.

Until 2004 year, Geim and Novoselov[1] successfully peel off single graphitic plane with the tape from graphite and place it on a silicon /silicon dioxide (Si/SiO_2) substrate, which allow its observation with an ordinary optical microscopy.[2-4] This discovery not only gained the Noble Prize in physics in 2010, but also opens up a new research topic of 2D materials in material physics. The fascination with graphene has been growing very rapidly and the physics of graphene is becoming one of the most interesting and fast-moving topics in condensed-matter physics. Many of the interesting physical phenomena appearing in graphene are governed by a very peculiar band structure, which the other 2D materials do not have. Its unique band structure equivalent to a relativistic massless particle gives rise to unusual electronic properties quite different from those of conventional systems. With a simple tight-binding calculation,[5] we see that there are two special points in the Brillouin Zone (BZ), called K and K', where the energy dispersion is linear with the momentum, with zero gap between the conduction and valence bands. The position where the conduction band and valence band touch at is so-called Dirac point.[6-8] It corresponds to a topologically singular point around which an electronic states acquires a geometrical phase factor called Berry's phase. It is responsible for the peculiar behavior in the transport properties, such as the minimum conductivity,[9] the dynamical conductivity,[10] and the localization effect.[5, 11] The high

speed massless, fermionic quasiparticles in graphene which travel at the Fermi velocity of v_F = 106 m/s (300 times slower than light), lead to the chiral tunneling and Klein paradox and the anomalous integer quantum Hall effect.[5]

1.1.2 Graphene nanoribbon and its electrical property

However, being a zero band gap material, perfect graphene is not suitable for semiconductor electronic devices. For example, when we plan to fabricate a Field Effect Transistor (FET) with graphene, it is impossible to turn off the electronic current flowing in the channel as a switch. This should be a fundamental requirement of a logic gate. Therefore a band gap should be induce into graphene, and keep its intrinsic unique characteristics, such as high electron mobility, thermal conductivity, mechanical strength and low noise.

One of the possible method is making graphene into nanometer-scale graphene nanoribbon (GNR) with either armchair or zigzag edges,[12, 13] as shown in Figure 1.1(b). Both the first principle calculation and experiments have shown that a band gap could be opened in nano-scaled armchair-GNRs (AGNRs) or zigzag-GNRs (ZGNRs). The origin of the band gap is dependent on the edge structure, i.e., zigzag or armchair. Although the mechanisms of this bandgap is different between AGNR and ZGNR, both the scales of band gap as the inverse of the ribbon width. The band gap of AGNR has

been reported to be caused by quantum confinement, while that of ZGNR is caused by spin polarization around the zigzag edges.[14]

Since the electrical conduction property of GNR is strongly dependent on the structure (especially edge state), it is important to investigate the relationship between them. It has been theoretically pointed out that when the width of ribbon width is 10 nm or less, the contribution of the edge state to the electric conduction becomes extremely important. Graphene nanoribbons correspond to a structure in which carbon nanotubes (CNT) are cut open along their axes. This edge structure can be defined by a chiral vector corresponding to the circumference of the carbon nanotube, and the vector perpendicular thereto corresponds to the edge of the ribbon. Assuming the basic lattice vectors with angle of 60°are as shown in Figure 1.2 (a), the chiral vector is defined as follows.

$$\boldsymbol{C_h} = n\boldsymbol{a} + m\boldsymbol{b}, \qquad 1\text{-}1$$

and $(n,\ m)$ is called the chiral index. The edges of both sides of the single-walled carbon nanotube are connected, which means they have a periodic boundary condition with a period of the chiral vector. On the other hand, graphene nanoribbons are terminated by edges on both sides, and have a boundary condition having the width of the chiral vector.

Figure 1.2 (b) shows the extended Brillouin zone of graphene, the wave vector

corresponding to the chiral vector period of single-walled carbon nanotubes $\boldsymbol{K_1}$, and $\boldsymbol{K_2}$which vector is perpendicular to $\boldsymbol{K_1}$. As mentioned above, the electronic state of graphene has no energy gap only at $\boldsymbol{K}$ and $\boldsymbol{K'}$. From this, if the group of line segments parallel to the wave vector just intersects with $\boldsymbol{K}$ and $\boldsymbol{K'}$, such single-walled carbon nanotubes have no energy gap and show metallic properties. Otherwise, it has a semiconductor-like property.

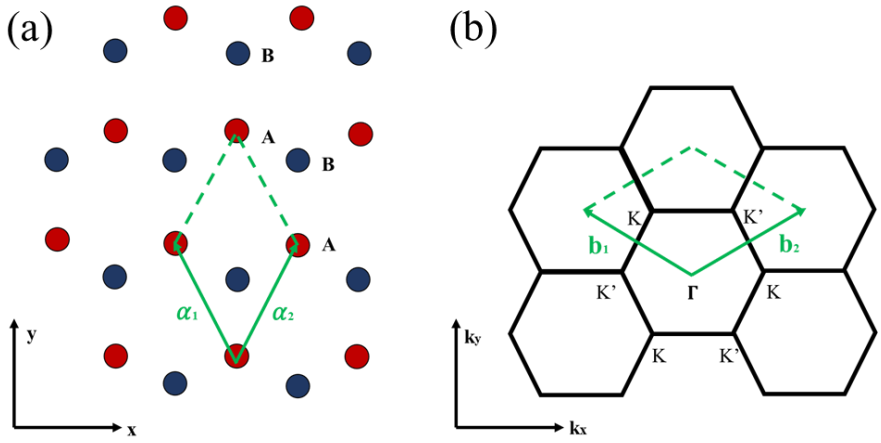

Figure 1.2 (a) Unit cell of graphene and (b) Extended Brillouin zone

The condition for showing metallic properties should be as below,

$$\boldsymbol{K}\cdot\frac{\boldsymbol{K_1}}{|\boldsymbol{K_1}|}=n|\boldsymbol{K_1}| \quad \text{or} \quad \boldsymbol{K'}\cdot\frac{\boldsymbol{K_1}}{|\boldsymbol{K_1}|}=n|\boldsymbol{K_1}| \qquad \text{(n; integer)} \tag{1-2}$$

Let us express the vector in the reciprocal lattice space in Figure 1.2 (b) by the basic vector $\mathbf{a_1}$, $\mathbf{a_2}$ in the real space. The basic vector in reciprocal lattice as shown:

$$\boldsymbol{b_1}=\frac{2}{3a^2}(2\boldsymbol{a_1}-\boldsymbol{a_2}), \qquad \boldsymbol{b_2}=\frac{2}{3a^2}(-\boldsymbol{a_1}+2\boldsymbol{a_2}) \tag{1-3}$$

Wave vector $\boldsymbol{K_1}$ corresponding to the chiral vector period can be expressed as:

$$\boldsymbol{K_1} = \frac{1}{|\boldsymbol{C_h}|^2}\boldsymbol{C_h} = \frac{1}{a^2(n^2+nm+m^2)}(n\boldsymbol{a_1} + m\boldsymbol{a_2}) \quad 1\text{-}4$$

$$|\boldsymbol{K_1}| = \frac{1}{a\sqrt{n^2+nm+m^2}} \quad 1\text{-}5$$

$\boldsymbol{K}$ and $\boldsymbol{K'}$ can express as:

$$\boldsymbol{K} = \frac{1}{3}(2\boldsymbol{b_1} + \boldsymbol{b_2}) = \frac{2}{3a^2}\boldsymbol{a_1} \quad 1\text{-}6$$

$$\boldsymbol{K'} = \frac{1}{3}(\boldsymbol{b_1} + 2\boldsymbol{b_2}) = \frac{2}{3a^2}\boldsymbol{a_2} \quad 1\text{-}7$$

From above calculation, equation 1-2 can be expressed as:

$$\boldsymbol{K} \cdot \frac{\boldsymbol{K_1}}{|\boldsymbol{K_1}|^2} = \frac{2n+m}{3} \quad 1\text{-}8$$

$$\boldsymbol{K'} \cdot \frac{\boldsymbol{K_1}}{|\boldsymbol{K_1}|^2} = \frac{n+2m}{3} \quad 1\text{-}9$$

Therefore, from equation 1-8 and 1-9, when $2n + m$ or $n + 2m$ becomes an integer multiple of 3, cutting line intersects $\boldsymbol{K}$ point or $\boldsymbol{K'}$ point. From the above, it can be found that the electrical property of CNT becomes a metal when $n - m$ becomes a multiple of 3.

This result also can apply to GNR. As we said above, the edge structure of GNR is divided into two typical types, which are called zigzag edges (blue line in Figure 1.1(b)) and armchair edges (red line in Figure 1.1(b)). For a zigzag edge, its chiral exponent $(n,\ m)$ has the relationship of $n = m$. In other words, when "$n - m$ becomes a multiple of 3" is satisfied, it is expected that the zigzag edge GNR has metallic properties. In the case of an armchair edge, the chiral index $(n,\ m)$ has the relationship of $n = 0$ or $m = 0$ or $n = -m$. When the condition "$n - m$ becomes a multiple of

3” is satisfied or not satisfied, it is expected that the metal or semiconductor properties will be obtained depending on the chiral index. On the other hand, it has been reported that, when the spin is taken into consideration, the result is different from the above result.

1.1.3 The preparation of graphene nanoribbon

In experiments, there are many different methods used to fabricate GNRs. Among them, it can be mainly separated into two kinds, bottom-up and top-down. Although bottom-up method can fabricate GNR with long length and atomically sharp edges by chemically synthetization from basic organic molecules, the synthesized ribbon have a contact with metal substrate, which influence the intrinsic property of GNR. In another top-down method, the ribbon could be fabricated from a large graphene flake. With this method, the undesired parts can be removed by many methods, such as: atomic force microscope (AFM) direct lithography,[15] scanning tunnel microscope (STM) lithography,[16] plasma etching (usually oxygen and hydrogen),[13, 17] and catalytic etching (usually metal partials).[18] Recently, another new top-down method has been achieved, with the development of in situ transmission electron microscopy (TEM) / scanning transmission electron microscopy (STEM) technology. In this method, electron beam in

TEM directly used to sculpt graphene and pattern it into desired ribbons. Since this method was also used in this thesis, we will explained it more detail and deeply in the following chapters.

1.2 Basis of transmission electron microscopy and characterization

Transmission electron microscope is a modern comprehensive large-scale analytical instrument, which is widely used in the research and development of modern science and technology. Just as the name implies, the so-called electron microscope is a microscope that uses an electron beam as a light source. The electron beam can bend under the effect of an external magnetic field or electric field, forming a refraction phenomenon similar to that when visible light passes through glass. Then this physical phenomenon was used to create the "lens" of the electron beam, and developed the electron microscope. The special feature for TEM is that the image is formed by the electron beam which go through the sample. That is the difference from the scanning electron microscope (SEM). Since the wavelength of the electron wave is much shorter than the wavelength of visible light (the wavelength of an electron wave of 100 kV is 0.0037 nm, and the wavelength of violet light is 400 nm), according to optical theory, we can expect that the resolving power of an electron microscope should be much better than that of an optical microscope. In fact, the resolving power of modern electron

microscopes has reached 0.1 nm.

Now we will briefly introduce the components and working principle of TEM. The schematic of a TEM is shown in Figure 1.3 (a), which is helpful for the visualization of components inside it. The explanation start from the top of TEM-electron gun, then we follow the path of it inside the microscope. The electrons come from the gun and accelerated at high energies, then go through 1^{st} and 2^{nd} condenser lens in order to focus on the sample. After interacting with the sample, the scattered electrons continue go through objective, intermediate and projector lens for magnifying the image and finally reach the image detector, as shown in Figure 1.3 (b). Since the real structure of the TEM is too complex, we only show the main components which related with our experiment.

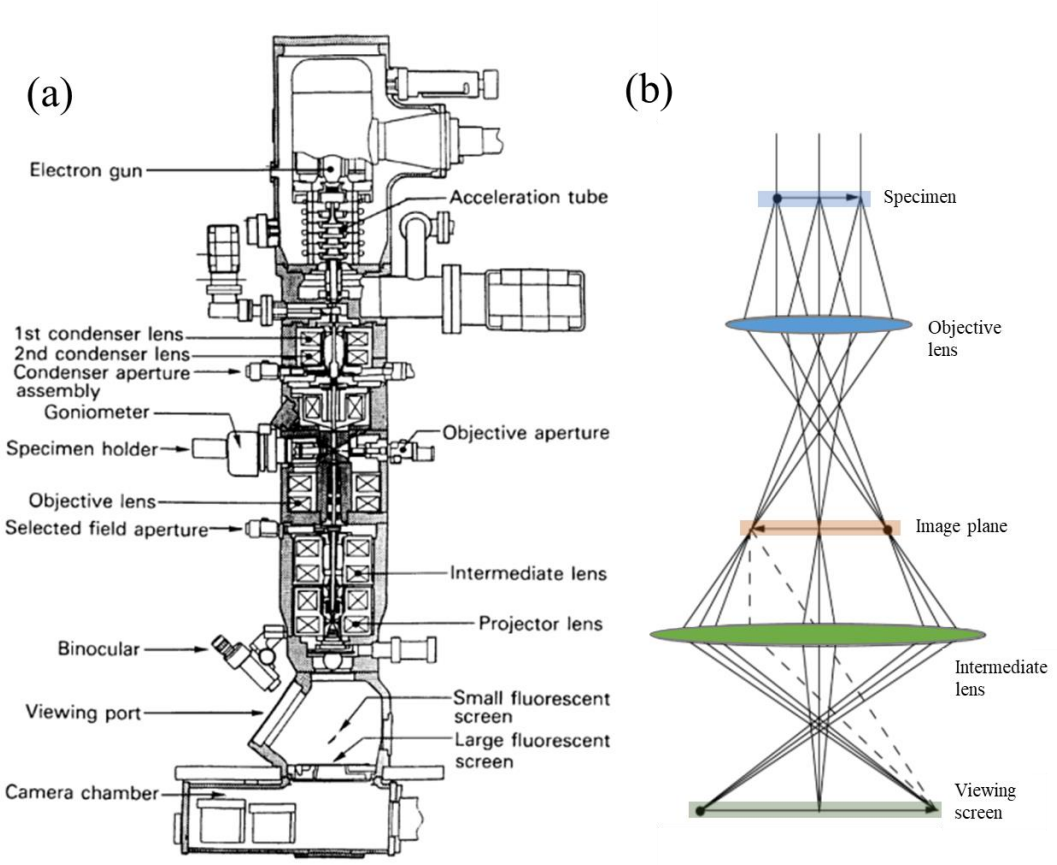

Figure 1.3 (a) Schematic of the cross section for a typical TEM, produced by JEOL Ltd., (b) Schematic of the microscopy in image mode.

As we know, TEM has been one of the useful tools for the characterization of materials. Usually, it can be used to observe the structure, analyze the element, measure the thickness and so on. Since TEM can provide some much useful information, even crystallographic orientation and atomic structure, the "classic" characterization methods, such as Raman spectroscopy or AFM microscopy didn't use throughout this thesis. In this experiment, the focused electron beam in TEM was used for nano-sculpting of graphene, as we discussed above, and the Fast Fourier Transform (FFT)

was used to distinguish monolayer and multilayer graphene, which based on the number of the diffraction spots. In conclusion, TEM is the most suitable tool for investigating the structure-dependence of electrical conductance properties for GNRs.

1.3 The previous investigation of GNR: A brief review

The structural dependence of band gap in GNRs has been investigated energetically.[13, 20-22] Yang et al.[22] calculated the band structure including the interaction between electrons based on the GW approximation (first-principles calculation including exchange interaction among electrons (in the case of fermions like electrons, it is related to Pauli exclusion rule)) and obtained a band gap of 1-3 eV for GNRs with widths of 2-1 nm. As shown in Figure 1.4, the band gap for AGNRs is inversely proportional to the ribbon width. However, the band gap for ZGNRs is not only dependent on the width, but also on the spin polarization along the zigzag edge. Magda et al.[23] fabricated GNRs with either zigzag or armchair edges under control with a nanolithographic technique using STM, as shown in Figure 1.5. In the case of AGNR, a clear inverse proportionality was revealed between the width and band gap, which was consistent with simulation results. However, in the case of ZGNR, the band gap was inversely proportional to the width for widths less than 7 nm, and then became metallic above 7 nm. All of these results indicate that both the edge structure and width

of the ribbon affect the band gap.

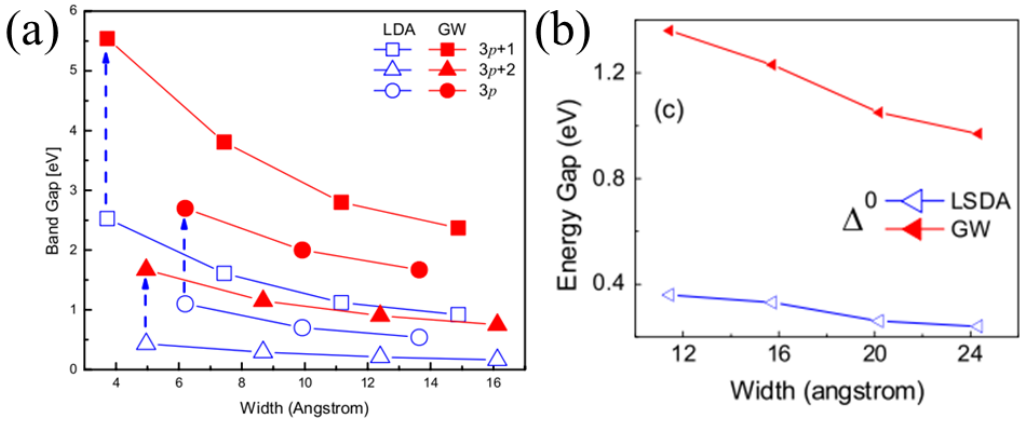

Figure 1.4 Variation of band gaps with the width of AGNR (a) and ZGNR (b).[22]

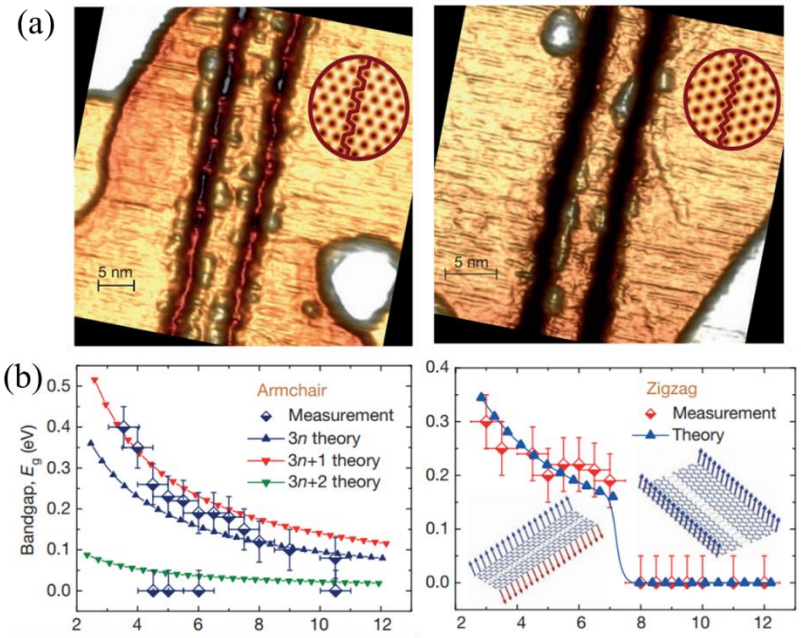

Figure 1.5 (a) Fabrication of graphene nanoribbons by using STM. (b) The bandgap measured by tunnelling spectroscopy as a function of ribbon width in armchair and zigzag ribbons.[23]

Recently, Areshkin and Nikolić [24] predicted that passing a sufficiently large tunneling current along ZGNRs may result in the destruction of spin polarization around the zigzag edges. Therefore, the current in the I-V curve may sharply increase at a critical value for ZGNRs due to the destruction of spin polarization. However, there have been no experimental results reported to suggest this. One of the reasons is that the I-V curves of GNRs in previous research have mainly been investigated with a silicon oxide film. With such a condition, the transport gap was predicted to be reduced due to dielectric-screening[25] and it is thus difficult to detect a sharp current increase in the I-V curve. Therefore, it would be desirable to obtain I-V curves for suspended ZGNRs.

The electrical conductance behavior of suspended GNRs should be measured with simultaneous identification of the ribbon structure. In situ TEM is thus a power tool to achieve this purpose. Drndić's group fabricated silicon chips for TEM observation that could bridge GNRs between electrodes and measured the electron conductance behavior with two-[26, 27] or three-terminal[28] methods, as shown in Figure 1.6. They reported that conductance of sub-10 nm wide GNR bilayers or monolayers was almost proportional to the width. Wang et al.[28] also achieved similar in situ TEM observations of suspended GNRs and reported that GNRs with a width of 1.6 nm showed a large transport gap of 400 meV from the I-V curve, as shown in Figure 1.7. However, the

edge structure dependence of the electrical conductance behavior has not been clarified by in situ TEM observations.

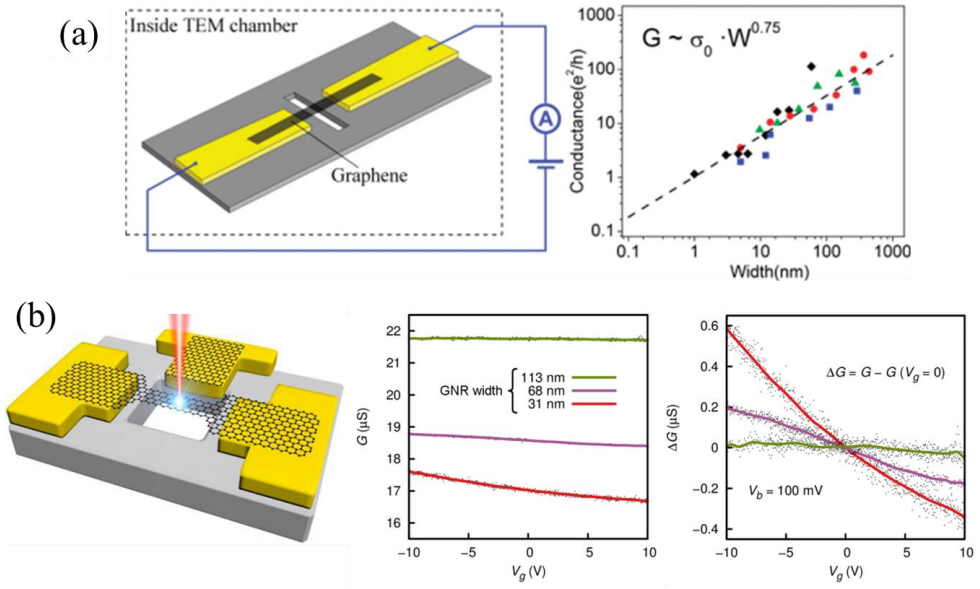

Figure 1.6 Schematic of suspended GNR with two- (a) and three-terminal (b) method and corresponding width dependent of conductance.[26,28] The change of conductance with different gate voltage under different bias voltage shown in Figure (b).

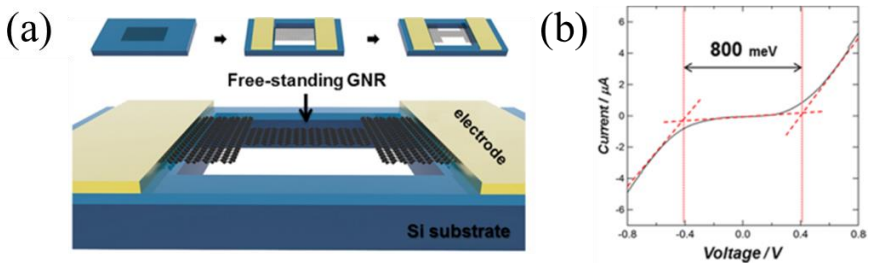

Figure 1.7 (a) Schematic of a two-terminal suspended GNR. (b) Current as a function of bias voltage, which shows a large transport gap.[29]

1.4 Purpose and method of present research

To address above issues, we have developed a suspended GNR device that can realize a controllable GNR structure with an electron beam in aberration-corrected TEM (AC-TEM) and measure the width and electronic properties in situ. In-situ TEM method is achieved because it is the most suitable and powerful tool to investigate the property of GNR with nanoscale, as we discussed in previous Chapter 1.2 and 1.3.

The complete process is shown as below: firstly, we fabricated suspended GNR devices and cleaned it by current annealing in TEM, then sculpted the ribbon by focused electron beam followed by the application of a high bias voltage. During the whole process, we performed in-situ electrical conductance measurements. Finally, we analyzed the structure dependent of electrical conductance property for GNR.

As mentioned above, other works[26, 27, 29-31] have already been done by similar methods and achieving remarkable results. But, our work distinguishes from five key elements:

1. Based on our fabricated GNR device and developed TEM holder, we have successfully identified the edge structure of the GNR for the first time.
2. Many GNRs with different layer numbers, length, width, and edge structure have been investigated, giving a good comparison of their electrical conductance

properties.

3. Restructure of GNR under different bias voltage has been investigated, including the layer number, width, edge structure of ribbon. The results indicated that ultra-narrow GNRs with well-defined edge structures can be fabricated by convergent electron beam nanosculpting followed by annealing with a high bias voltage.
4. The current-voltage (I-V) curves was measured during the whole thinning process, which could be used to find the voltage of opening the energy gap. It is useful to investigate the different formation mechanism of band gap between AGNR and ZGNR.
5. The fabricated narrow width and short length suspended ZGNR showed a sharp increase (almost discontinuous change) at the threshold voltage in the differential conductance curve as a function of bias voltage, which could be explained by a current-driven nonequilibrium transition from a magnetic-insulator phase to a nonmagnetic-metal phase, which only predicted in theory.

1.5 Conclusion

In this chapter, we introduce graphene and graphene nanoribbon, which is mainly investigated in this thesis, and explain the benefits of using in-situ TEM observation to understand the influence of the edge structure to the electrical conductance property.

Then we explain the component and working principle of a TEM, which can be used to count the layer numbers of graphene based on the analysis of electron diffraction pattern. After that, we give a brief overview of recent theoretical and experimental progress about the investigation of electrical conductance properties for GNR by transmission electron microscopy. Finally, we point out our research method and purpose.

Reference

[1]. Novoselov, K. S.; Geim, A. K.; Morozov, S. V.; Jiang, D.; Zhang, Y.; Dubonos, S. V., et al., Electric field fffect in atomically thin carbon films. *Science* 2004, 306 (5696), 666–669.

[2]. Kotakoski, J.; Santos-Cottin, D.; Krasheninnikov, A. V., Stability of graphene edges under electron beam: equilibrium energetics versus dynamic effects. *ACS Nano* 2012, 6 (1), 671–676.

[3]. Blake, P.; Hill, E. W.; Neto, A. H. C.; Novoselov, K. S.; Jiang, D.; Yang, R., et al., Making graphene visible. *Applied Physics Letters* 2007, 91 (6), 063124.

[4]. Casiraghi, C.; Hartschuh, A.; Lidorikis, E.; Qian, H.; Harutyunyan, H.; Gokus, T., et al., Rayleigh imaging of graphene and graphene layers. *Nano Letters* 2007, 7 (9), 2711–2717.

[5]. Castro Neto, A. H.; Guinea, F.; Peres, N. M. R.; Novoselov, K. S.; Geim, A. K., The electronic properties of graphene. *Reviews of Modern Physics* 2009, 81 (1), 109–162.

[6]. McClure, J. W., Diamagnetism of graphite. *Physical Review* 1956, 104 (3), 666–671.

[7]. DiVincenzo, D. P.; Mele, E. J., Self-consistent effective-mass theory for intralayer screening in graphite intercalation compounds. *Physical Review B*

1984, 29 (4), 1685–1694.

[8]. Uryu, S.; Ando, T., Prominent exciton absorption of perpendicularly polarized light in carbon nanotubes. *AIP Conference Proceedings* 2007, 893 (1), 1033–1034.

[9]. Shon, Nguyen H.; Ando, T., Quantum transport in two-dimensional graphite system. *Journal of the Physical Society of Japan* 1998, 67 (7), 2421–2429.

[10]. Zheng, Y.; Ando, T., Hall conductivity of a two-dimensional graphite system. *Physical Review B* 2002, 65 (24), 245420.

[11]. Suzuura, H.; Ando, T., Phonons and electron-phonon scattering in carbon nanotubes. *Physical Review B* 2002, 65 (23), 235412.

[12]. Jacobse, P. H.; Kimouche, A.; Gebraad, T.; Ervasti, M. M.; Thijssen, J. M.; Liljeroth, P., et al., Electronic components embedded in a single graphene nanoribbon. *Nature Communications* 2017, 8 (1), 119.

[13]. Han, M. Y.; Ozyilmaz, B.; Zhang, Y.; Kim, P., Energy band-gap engineering of graphene nanoribbons. *Physics Review Letters* 2007, 98 (20), 206805.

[14]. Son, Y. W.; Cohen, M. L.; Louie, S. G., Energy gaps in graphene nanoribbons. *Physics Review Letters* 2006, 97 (21), 216803.

[15]. Masubuchi, S.; Ono, M.; Yoshida, K.; Hirakawa, K.; Machida, T., Fabrication of graphene nanoribbon by local anodic oxidation lithography using atomic

force microscope. *Applied Physics Letters* 2009, 94 (8), 082107.

[16]. Tapasztó, L.; Dobrik, G.; Lambin, P.; Biró, L. P., Tailoring the atomic structure of graphene nanoribbons by scanning tunnelling microscope lithography. *Nature Nanotechnology* 2008, 3 (7), 397–401.

[17]. Xie, L.; Jiao, L.; Dai, H., Selective etching of graphene edges by hydrogen plasma. *Journal of the American Chemical Society* 2010, 132 (42), 14751–14753.

[18]. Campos, L. C.; Manfrinato, V. R.; Sanchez-Yamagishi, J. D.; Kong, J.; Jarillo-Herrero, P., Anisotropic etching and nanoribbon formation in single-layer graphene. *Nano Letters* 2009, 9 (7), 2600–2604.

[19]. Fultz, B.; Howe, J. M., Transmission electron microscopy and diffractometry of materials. *Springer Science & Business Media*: 2012.

[20]. Aoki, M.; Amawashi, H., Dependence of band structures on stacking and field in layered graphene. *Solid State Communications* 2007, 142 (3), 123–127.

[21]. Xia, F.; Farmer, D. B.; Lin, Y.-m.; Avouris, P., Graphene field-effect transistors with high on/off current ratio and large transport band gap at room temperature. *Nano Letters* 2010, 10 (2), 715–718.

[22]. Yang, L.; Park, C. H.; Son, Y. W.; Cohen, M. L.; Louie, S. G., Quasiparticle energies and band gaps in graphene nanoribbons. *Physics Review Letters* 2007,

99 (18), 186801.

[23]. Magda, G. Z.; Jin, X.; Hagymasi, I.; Vancso, P.; Osvath, Z.; Nemes-Incze, P., et al., Room-temperature magnetic order on zigzag edges of narrow graphene nanoribbons. *Nature* 2014, 514 (7524), 608–611.

[24]. Areshkin, D. A.; Nikolić, B. K., I−V curve signatures of nonequilibrium-driven band gap collapse in magnetically ordered zigzag graphene nanoribbon two-terminal devices. *Physical Review B* 2009, 79 (20), 205430.

[25]. M.E. Schmidt; M. Muruganathan; T. Kanzaki; T. Iwasaki; A.M.M. Hammam; S. Suzuki, et al., Dielectric-screening reduction-induced large transport gap in suspended sub-10 nm graphene nanoribbon functional devices, *Small* 2019, 15 (46), 1903025.

[26]. Lu, Y.; Merchant, C. A.; Drndic, M.; Johnson, A. T., In situ electronic characterization of graphene nanoconstrictions fabricated in a transmission electron microscope. *Nano Letters* 2011, 11 (12), 5184–5188.

[27]. Qi, Z. J.; Rodriguez-Manzo, J. A.; Botello-Mendez, A. R.; Hong, S. J.; Stach, E. A.; Park, Y. W. , et al., Correlating atomic structure and transport in suspended graphene nanoribbons. *Nano Letters* 2014, 14 (8), 4238–4244.

[28]. Rodriguez-Manzo, J. A.; Qi, Z. J.; Crook, A.; Ahn, J. H.; Johnson, A. T.; Drndic, M., In situ transmission electron microscopy modulation of transport in

graphene nanoribbons. *ACS Nano* 2016, 10 (4), 4004–4010.

[29]. Wang, Q.; Kitaura, R.; Suzuki, S.; Miyauchi, Y.; Matsuda, K.; Yamamoto, Y., et al., Fabrication and in situ transmission electron microscope characterization of free-standing graphene nanoribbon devices. *ACS Nano* 2016, 10 (1), 1475–1480.

[30]. Jia, X.; Hofmann, M.; Meunier, V.; Sumpter, B. G.; Campos-Delgado, J.; Romo-Herrera, J. M., et al., Controlled formation of sharp zigzag and armchair edges in graphitic nanoribbons. *Science* 2009, 323 (5922), 1701–1705.

[31]. Rodriguez-Manzo, J. A.; John Qi, Z.; Puster, M.; Balan, A.; Charlie Johnson, A. T.; Drndic, M., Fabrication and simultaneous electrical measurement of graphene nanoribbon devices inside a S/TEM. *Microscopy and Microanalysis* 2015, 21 (S3), 1155–1156.

Chapter 2 Experimental setup and sample preparation

Introduction

This chapter contains experimental setup, all the fabrication recipes and the experimental details which were used in the later part of this thesis. It mostly contains information on experimental setup, the design of home-built holder, the fabrication and characterization of suspended GNR devices. The fabrication process of GNR devices, including the evaporation of metal electrodes, cutting a spatial gap, transfer and pattering of a ribbon.

2.1 Experimental setup

In order to perform in-situ TEM observation and nano-sculpting, in combination with electrical measurements, we have built a custom designed setup, which is illustrated in Figure 2.1. Starting from the left to right, we see a spherical aberration correction software, the TEM microscope (a 50 pm resolved aberration-corrected TEM (JEOL R005) operated at 80 kV and under a pressure of 10^{-6} Pa) with a TEM holder inserted from the side entry, and the electrical measurement system. The home built TEM holder connect with a source meter (Keithley 2635A) for electrical measurements. The bias voltage was swept in order from 0.0 to 1.0 V, 1.0 to -1.0 V, and -1.0 to 0.0 V, which corresponded to one cycle, and the current was measured at each 50 mV step. For obtaining current value accurately and reducing the influence of noise, the output current was programmed to average 10 cycles of the I-V measurement results. The measurement time was dependent on the current value; therefore, the measurement time was not constant. The program was developed by Labview to set the bias voltage and record the measured values.

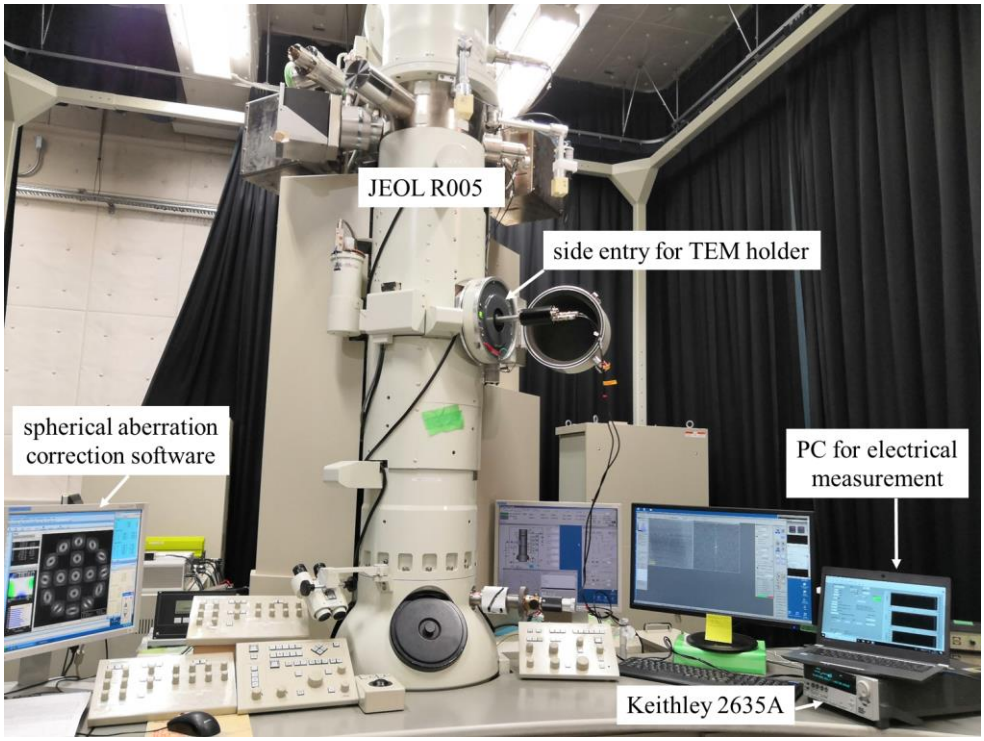

Figure 2.1 Experimental setup: aberration-corrected TEM JEOL R005 with home built holder inside, and the electrical measurement system including Keithley 2635A and the PC with software.

2.2 The design of in-situ TEM holder

Figure 2.2 (a) shows the custom-designed TEM holder, equipped with electrical connections at the bottom. Inside the holder, there are three wires connect the tip, where the specimen is located. Concerning the practical realization of this holder, its design and manufacturing is entirely done in-house, using the facilities provided by the KITANO SEIKI Incorporated.

An enlargement of the TEM holder tip is shown in Figure 2.2 (b): from left to right,

it mainly consists of one sample stage, three tungsten probes fixed on one spring-loaded poly-ether-ether-ketone (PEEK) board and three coaxial cables. The sample stage enables us to load a silicon (Si) chip with three different GNR devices. The electrical contact can be established without breaking the Si chip by controllably connecting three tungsten probes with the three electrodes of the GNR devices. Figure 2.2 (c) shows the schematic illustration of the area around the head of the TEM holder with electrical connections. By this design, we realize the measurement of electrical conductance properties with observing the sample in TEM simultaneously.

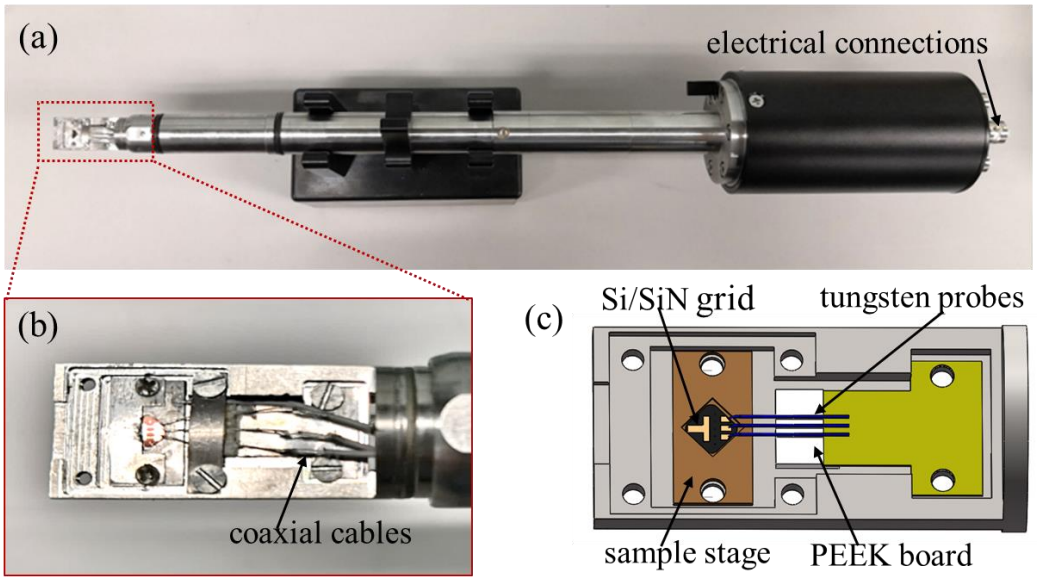

Figure 2.2 (a) Optical images of home built holder. The black arrow indicate the electrical connections with Keithley 2635A. (b) Enlarged images of the head of holder with sample loaded. (c) Schematic illustration of the area around the head of the TEM holder with electrical connections.

2.3 The design of custom TEM chip

The custom TEM chip is a silicon substrate/silicon nitride film (Si/SiN) chip with dimensions of approximately 2.6 × 2.6 mm obtained from SiMPore Incorporated, as shown in the inset of Figure 2.3. It is consisted of a 200-μm-thick silicon wafer covered with a 50-nm-thick SiN film on both sides.

As shown in the Figure 2.3 (a), there are five square windows and three rectangular windows in each chip, which are transparent to electron beam. Those windows are only covered by SiN membrane, which can be used in TEM observation.[1,2] From the enlarged SEM images in Figure 2.3(b), the area of each square window and rectangular window is 60 × 60 μm and 500 × 60 μm, respectively. In this experiment, we only designed three tungsten probes for measuring the electrical conductance properties, so only the three central square windows was used for fabrication.

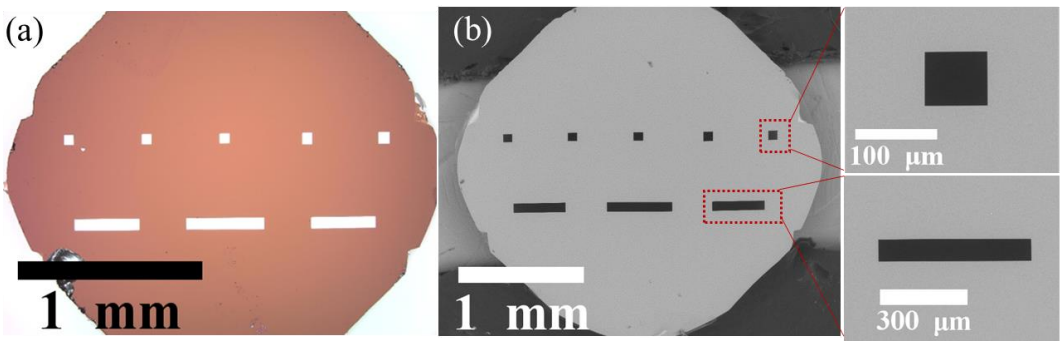

Figure 2.3 (a) Photograph of Si/SiN chip with optical microscopy. (b) SEM image of

the initial chip before fabrication process. The enlarged images shows a square window and rectangular window, respectively.

2.4 The fabrication of GNR device

2.4.1 List of equipment used for fabrication

Firstly, we list the main equipment which used for the fabrication of GNR device, and briefly introduce their functions in this experiment.

1. Electron Beam Lithography

Figure 2.4 Photograph of Electron Beam Lithography machine.

Electron Beam Lithography (EBL, ELS-7500) fabricated by ELIONIX Company.

In this experiment, it was used to pattern the designed shape on sample.[3] First time, it was used to exposure the electrodes on the Si chip, as describe in Chapter 2.4.3; second time, it was used for patterning the ribbon shapes of graphene, as introduce in Chapter 2.4.5.

2. Reactive Ion Etching system

Figure 2.5 Photograph of Reactive Ion Etching system.

Reactive Ion Etching system (RIE-10NR) fabricated by SAMCO Company. In this experiment, it was used to clean the surface of sample by strong oxygen plasma before

electrode fabrication[4] in Chapter 2.4.3. In addition, it was also used for etching back layer graphene and exposed graphene in Chapter 2.4.5.

3. Electron Beam Evaporation system (MUE-ECO-EB)

Figure 2.6 Photograph of Electron Beam Evaporation system.

Electron Beam Evaporation system (MUE-ECO-EB) fabricated by ULVAC Company. It was used to deposit the different metals by electron beam evaporation to fabricate the electrodes for devices. In Chapter 2.4.3, chromium/gold (Cr/Au) were deposited by electron beam evaporation on the sample.

4. Focused Ion Beam

Figure 2.7 Photograph of Focused Ion Beam machine.

Focused Ion Beam (FIB, SMI-3050) fabricated by HITACHI Company. In Chapter 2.4.4, by using Gallium (Ga) ion beam, we can cut a nano-gap at the center of electrode in our experiment.[5,6] The desired dimensions of gap can be controlled by different setting parameters, such as: width, depth and height.

5. Transmission Electron Microscope

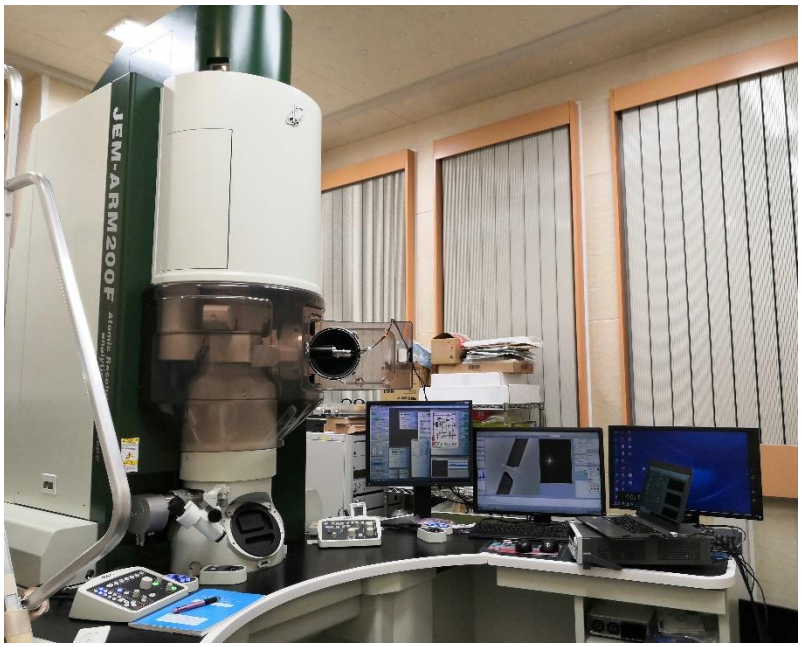

Figure 2.8 Photograph of Transmission Electron Microscope machine.

Transmission Electron Microscope (TEM, JEM-ARM200F) fabricated by JEOL Company.[7] In this experiment, it was used to check the size of gap after using FIB (Chapter 2.4.4) and the fabricated suspended GNRs (Chapter 2.4.5). The acceleration voltage of this machine can be operated at 120 or 200 kV. Since this machine does not have spherical aberration-corrector for TEM mode, it is only used for checking the size of ribbon or taking some low-magnification images.

High resolution TEM images (HR-TEM) of graphene were taken by a 50 pm resolved aberration-corrected TEM (JEOL R005) operated at 80 kV in Tokyo Institute of Technology as shown in Figure 2.1.

2.4.2 The overall process of fabrication

The fabrication process of suspended GNR device is shown in Figure 2.9, which mainly consists of three steps. The first step is the fabrication of three source-drain electrodes for electrical conductance measurement (Figure 2.9 (a-e)). After the surface of the Si/SiN chip was cleaned with acetone solution, thin Methyl methacrylate (MMA) and poly (methyl methacrylate) (PMMA) resist layers were spin-coated onto the surface of chip and patterned by conventional electron beam lithography (EBL, ELS-7500). After developing in methylisobutylketone/isopropyl alcohol (MIBK/IPA) to dissolve the exposed PMMA, electron beam evaporated Cr/Au were deposited on the chip at thicknesses of 5 and 40 nm, respectively. Subsequently, N-methyl-2-pyrrolidone (NMP) was used to lift-off the MMA/PMMA layer while leaving the electrodes. The second step is cutting a spatial gap for suspending the GNR (Figure 2.9 (f)). A gap with a width of 100-300 nm and a length of 2.5 μm was cut at the center of the narrowest electrode by a Ga FIB (SMI-3050), where graphene will be placed. This is essential for TEM observation, the GNR can be directly observed and can be modified in shape and/or size by an intense electron beam. The final step is the transfer and pattering of suspended graphene (Figure 2.9 (g-i)). Large-area graphene grown by chemical vapor deposition (CVD) covered by PMMA layer was directly transferred onto the prepared chip and patterned by using EBL, then followed with O_2 plasma etching step (RIE-

10NR) to remove the exposed graphene. Finally, the sample was soaked in acetone overnight to completely remove PMMA.[8,9] The details of each step will show in the following content.

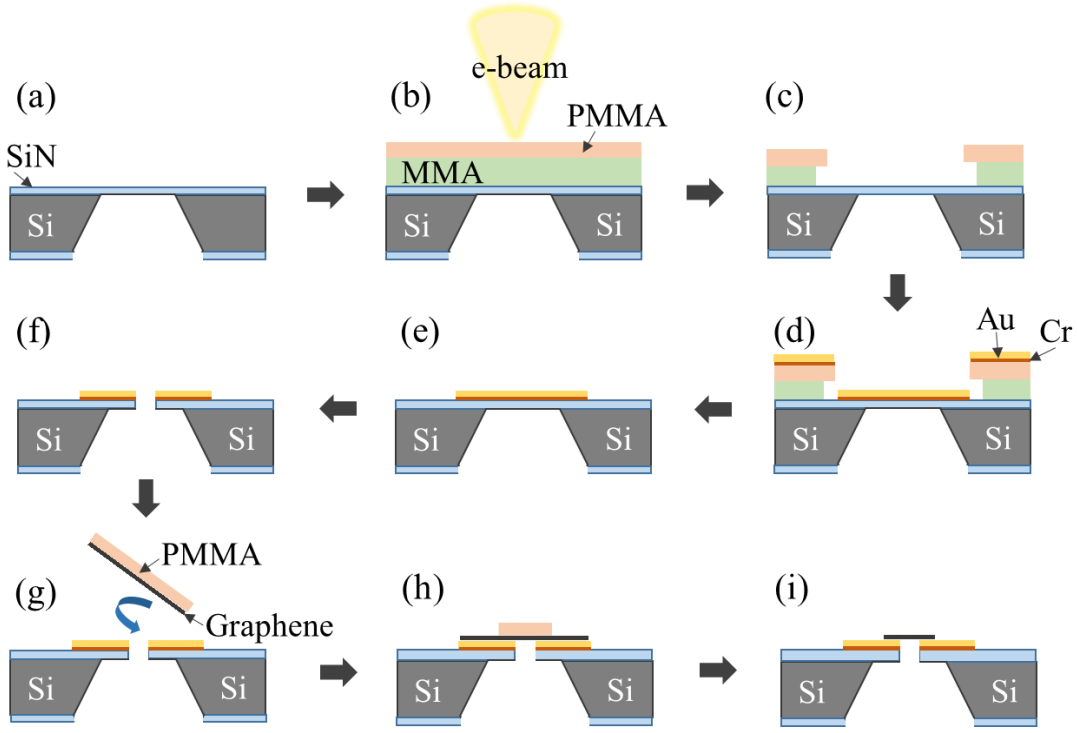

Figure 2.9 Fabrication steps for producing a suspended GNR device. (a) Initial Si/SiN chip. (b) MMA/PMMA resist layers are spin-coated on the surface of the chip and exposed to an electron beam. (c) The desired electrode pattern is formed by lithography. (d) Cr/Au films are obtained by electron beam deposition. (e) Lift-off process. (f) A gap is created by an FIB at the center of the electrodes. (g) CVD-grown graphene covered with PMMA is directly transferred onto the Si chip. (h) Graphene is patterned into a

nanometer-wide ribbon. (i) A suspended GNR is obtained between two electrodes after O_2 plasma etching and acetone cleaning.

2.4.3 Electrodes fabrication

In previous section, we explained the overall process of fabrication GNR devices. Here we describe in more detail about the fabrication of the Cr/Au electrodes to measure the electrical conductance properties of graphene.

As we mentioned in the last section (Chapter 2.3), the size of TEM grid is very small, which make it difficult to load on a sample stage for spin coating or electron beam exposure process. For fabricating the electrodes on TEM grid, we need to find one method to catch it easily by tweezer and fix it during the fabrication process. For solving this problem, we designed an aluminum (Al) plate for fixing the TEM grid as shown in Figure 2.10. The size of this plate is 20.0 × 15.0 mm, with a thickness of 1.0 mm. At the right side of this plate, there is a hollow of a diamond which corners are rounded. The size of diamond shape is slightly larger than TEM grid for fixing it. The depth is 0.2 mm, which is same with TEM grid. This design will make sure the surface is flat after fixing the grid into Al plate. The round hole below the diamond hollow is used to avoid the damage of SiN membrane during evacuation.

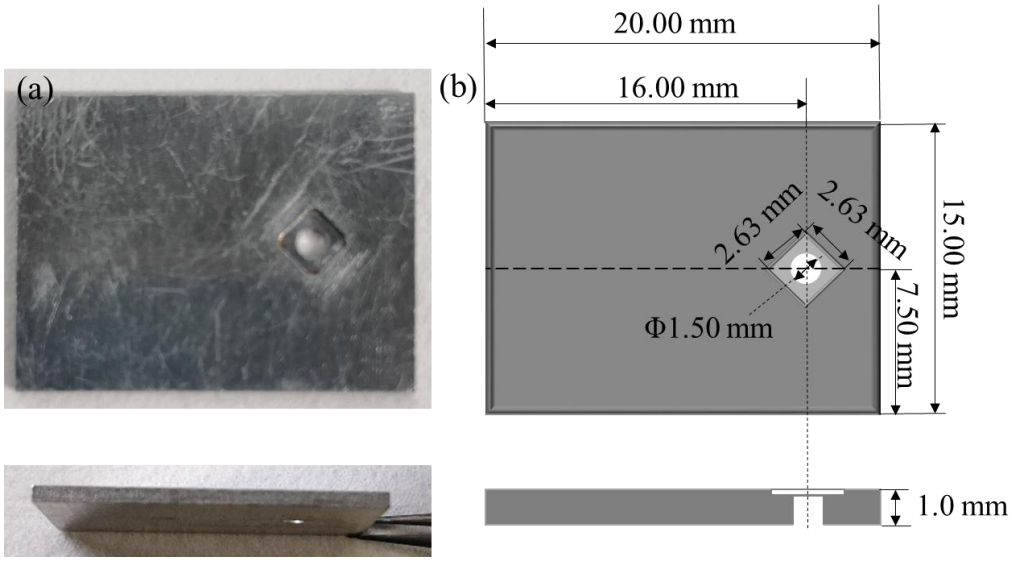

Figure 2.10 (a) Photograph of an aluminum plate for fixing the TEM grid. (b) Schematic illustration of the detail design of this plate.

The photograph during the fabrication process are shown in Figure 2.11 (a-f). Firstly, the TEM grid was cleaned with acetone solution and fixed onto Al plate (Figure 2.11 (a,b)). The SiN membrane of TEM grid was so flat that it's hard to coat with resist layer. In this case, we tried to make a little roughness of the SiN surface by O_2 plasma. After O_2 plasma treatment, double layer positive electron-beam resist MMA/PMMA were spin coated on the chip, as shown in Figure 2.11 (c).

EBL was used to pattern the designed electrode shapes. The MMA/PMMA resist was exposed with an electron beam by ELS-7500. After the development in MIBK:IPA solution, the pattern of electrodes could be seen clearly as shown in Figure 2.11 (d). From the enlarged image in the window, we can confirm the thinnest part of electrode

also had been formed. Electron beam evaporator was used to deposit electrodes. After the deposition of Cr/Au metal, an optical photograph of chip of Figure 2.11 (e) shows that all the surface were deposited with metal. Finally, this sample was lift-off with NMP solution for at least 3 hours. During this step, we must take care of the SiN membrane in the window, because it is very fragile. Under this condition, we cannot use ultrasound sonication in this step. The fabricated electrodes on the grid of Figure 2.11 (f) shows three separated source electrodes, a large pad as common drain electrode and some small marks for second time lithography. By this design, we can obtain three individual GNRs on one chip. From an enlarged photograph of the electrode in a small window, the size of thinnest part of electrode is 1.5 μm wide and 20 μm long. All details and setting parameters during this fabrication process has been list in following table 2.1.

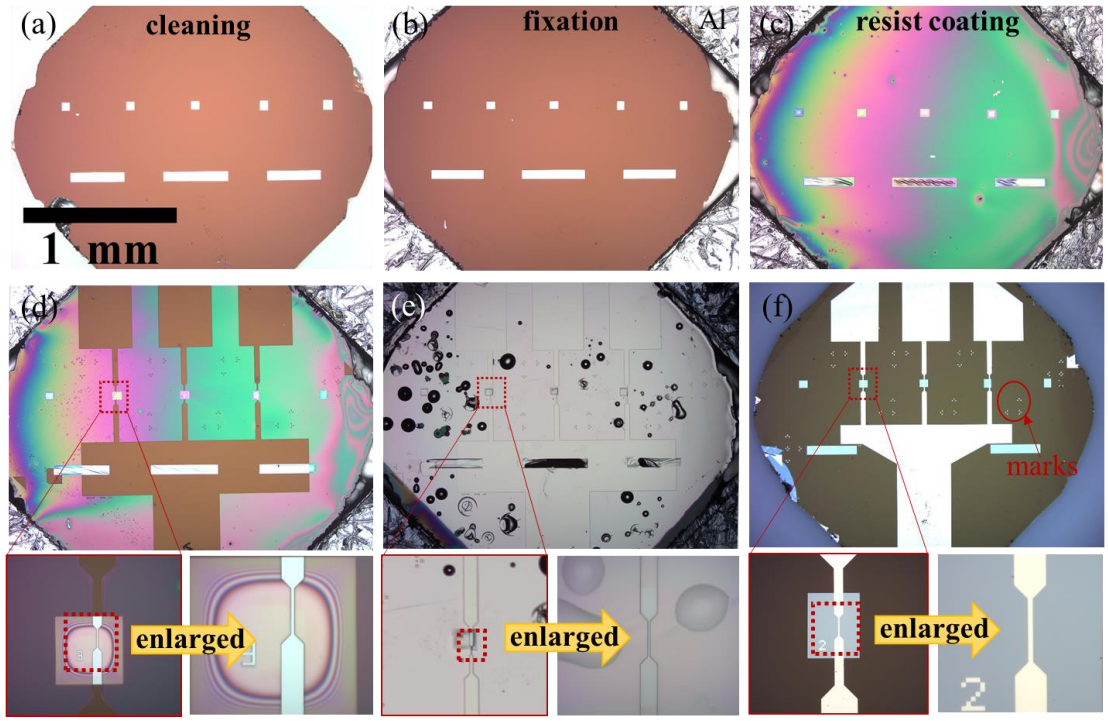

Figure 2.11 Electrodes fabrication in cleanroom. Photograph of TEM grid after (a) cleaning with acetone solution, (b) fixing on a Al plate, (c) resist coating with MMA/PMMA, (d) electron beam lithography and development, (e) E-beam deposition with Cr/Au, (f) lift off with NMP solution.

Table 2.1 List of 1st steps for electrodes fabrication on TEM grid.

1st Step – Electrode fabrication on TEM grid		
Step#	**Step description and detail parameter**	**photograph**
1	**Cleaning of TEM grid** Clean the grid in those solutions with the turn: Acetone-IPA-DIW, 3 min for each solution.	Figure 2.11 (a)
2	**Fixation of TEM grid on Al plate** Stick grid with PMMA onto the plate, then heating on hot plate at 180 ℃ for 5 min.	Figure 2.11 (b)
3	**Making the roughness surface of SiN membrane** Using O_2 plasma by RIE (10 sccm, 4 min, 100 W, 4 Pa)	-
4	**Resist coating with MMA/PMMA double layer** 1st layer: MMA copolymer, spincoat 2000 rpm, bake 5 min on hotplate @180°C. 2nd layer: PMMA 495K A4, spincoat 4000 rpm, bake 5 min on hotplate @180°C.	Figure 2.11 (c)
5	**Electron beam lithography and development** Exposure dose: 300 μC/cm^2 with 1nA current. Develop in MIBK:IPA=1:3, for 2 min, MIBK:IPA=1:1, for 20 sec, rinse 45 sec in IPA.	Figure 2.11 (d)
6	**E-beam deposition with Cr/Au** First deposit adhesion layer of Cr, 5 nm with 1.0 A/sec deposition rate, then Au layer, 40 nm at 2.0 A/sec.	Figure 2.11 (e)
7	**Lift off with NMP** The sample soaked in NMP for at least 3 hours and lift-off, then clean by IPA solution for 3 min	Figure 2.11 (f)

2.4.4 Fabrication of nano-gaps on the electrode

For TEM observation, graphene must be completely free-standing, which is essential for imaging and sculpting. A gap should be cut on the electrode for separating it to source and drain. Here, we fabricated several gaps with different width and length

by using focused ion beam with Ga ion source (SMI-3050).

The TEM images of fabricated gaps are shown in Figure 2.12, the minimum width is 40 nm, and the maximum is 330 nm. After cutting the gap, the electrode was separated from the center. The size of gaps were controlled by the setting parameter during FIB process, which is list in Table 2.2. Although we can fabricate different widths of gap, a narrow size of gap was not suitable for our experiment. There are two reasons: (1). When the width of gap is very narrow, after transfer CVD-grown graphene, the contact condition between electrodes and graphene is poor, so that the initial contact resistance value is very large. (2). When we clean the surface of GNR by current annealing, the width of gap will change due to high temperature. Under this condition, for narrow gap, the change of width is so large, which makes the ribbon easily rupture due to the stretch force. In conclusion, in the following experiments, we usually fabricate the gaps with the width of 100-300 nm.

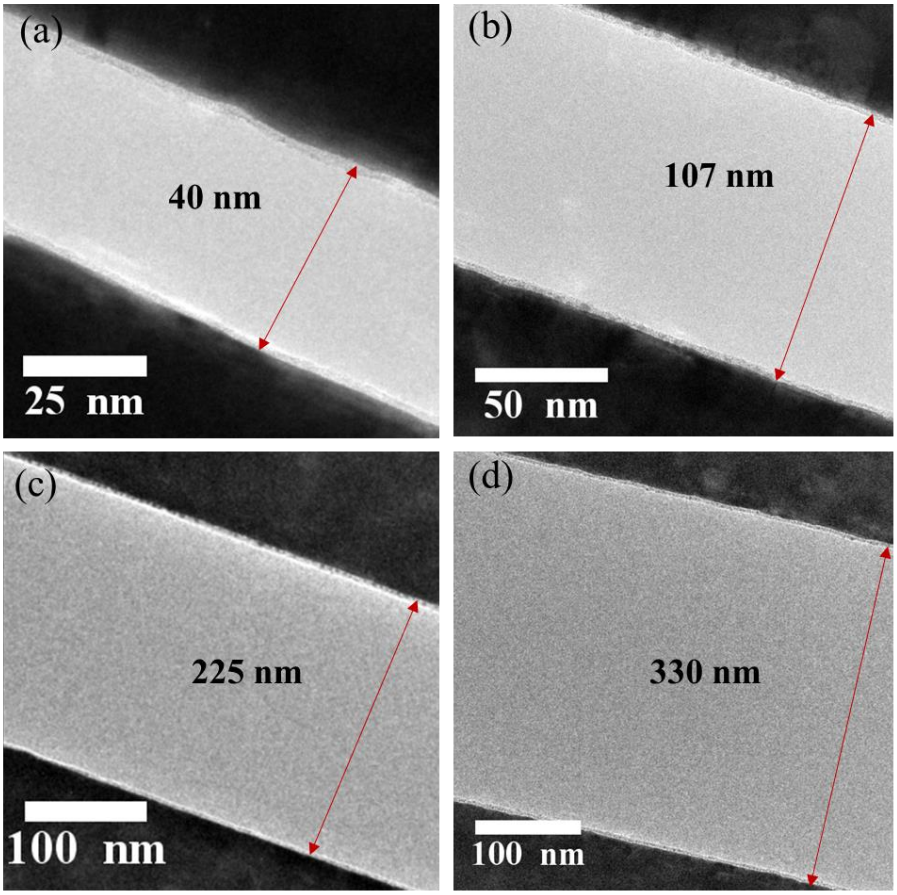

Figure 2.12 Several fabricated nano-gaps by FIB with the different width of (a) 40 nm, (b) 107 nm, (c) 225 nm, (d) 330 nm, respectively. The black part indicate the Cr/Au electrodes, and the red arrow indicate the measured width of gap.

Table 2.2 List of 2nd steps for cutting nano-gap on electrode.

2nd Step – Nano-gap fabrication on electrode						
Sample	**Beam condition**	**Length (μm)**	**Height (μm)**	**Depth (μm)**	**Width of gaps** (nm)	**TEM images**
1	Ufine	2.5	0.04	0.25	40	Figure 2.12 (a)
2	Ufine	2.5	0.10	0.20	107	Figure 2.12 (b)
3	Ufine	2.5	0.20	0.20	225	Figure 2.12 (c)
4	Ufine	2.5	0.30	0.20	330	Figure 2.12 (d)

2.4.5 Transfer and pattering of graphene

In this part, we focus on the 3rd step: the transfer and pattering of CVD-grown graphene. The CVD graphene grown on copper foil was bought form Graphene Platform Corporation.

As shown in Figure 2.13 (a), a monolayer graphene was grown on 100 mm thick copper foil by CVD method. Figure 2.13 (b) shows the schematic viewing from the cross section. It consists of five layers. From top to bottom, a protect layer, graphene on the top layer, copper foil, graphene on the back layer and heat release sheet.

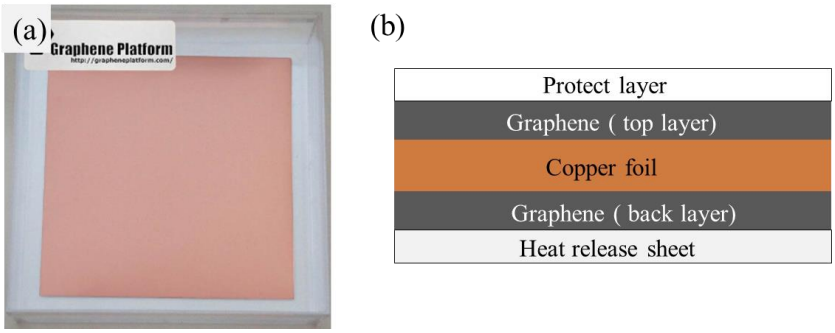

Figure 2.13 (a) CVD-grown monolayer graphene on 100 mm thick copper foil bought from Graphene Platform Corporation. (b) Schematic of CVD graphene from the cross section.

The transfer method is shown in Figure 2.14. Firstly, the large-area CVD grown graphene on a copper foil was cut to an area of 1 × 1 cm, and peel off the protect layer.

Then, a thin PMMA resist layer was spin-coated onto the surface at 4000 rmp, and baked on the hot plate at 180 ℃ for 5 min with peeling off the heat release sheet. The back layer graphene was etched using O_2 plasma by RIE (15 sccm, 25 sec, 30 W, 4 Pa). Subsequently, the PMMA-coated graphene with the copper foil was floated facing down on 5% Ammonium Persulfate solution (APS) to remove the copper foil. For avoiding the copper oxide (CuO) formed during this process, we also make it floated on 50% hydrochloric acid (HCl) solution. Finally, the remaining PMMA-coated graphene was cleaned by deionized water (DIW). The detail time and sequence are list in Table 2.3.

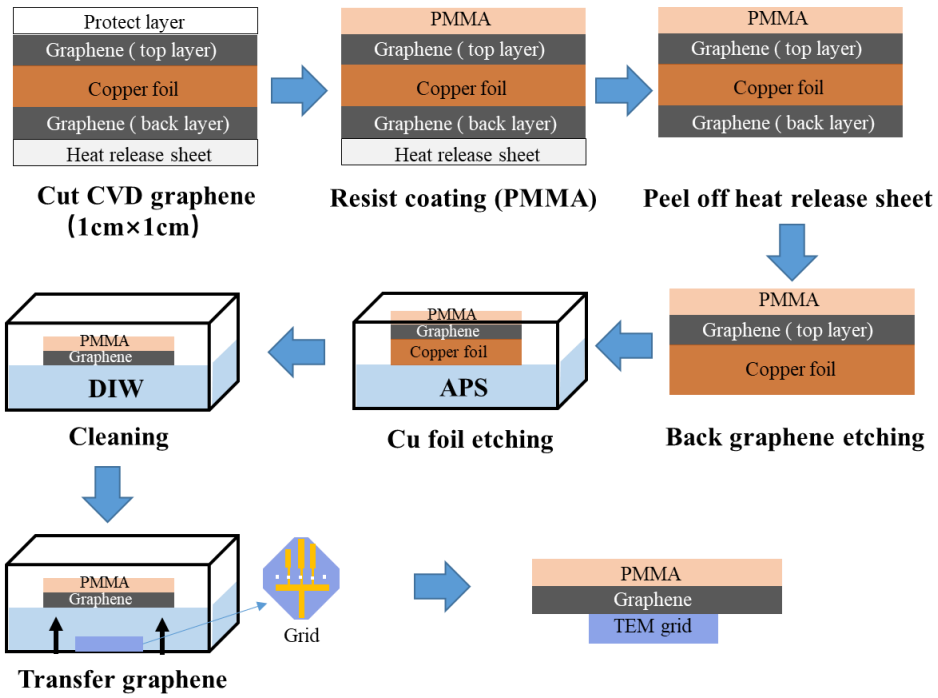

Figure 2.14 Schematic of whole transfer process of graphene onto prepared TEM grid.

Table 2.3 List of 3rd steps for preparing transferred graphene.

3rd Step – Preparing the transferred graphene.			
Step#	**Step description**	**Solution**	**Time (min)**
1	Cu foil etching	APS	45
2		APS	45
3		APS	45
4		APS	360~
5	CuO etching	HCl	10
6	Cleaning	DIW	10
7	Cu foil etching	APS	10
8	Cleaning	DIW	10
9	CuO etching	HCl	10
10	Cleaning	DIW	10
11	Cleaning	DIW	10
12	Cleaning	DIW	50~

After etching the Cu foil layer under graphene, it was directly transferred onto the prepared TEM grid and drying for more than 24 h as shown in Figure 2.15 (a). Then the transferred graphene was patterned into nanoribbons by EBL again. The small marks which mentioned in Figure 2.11 (f) were used to adjust the position of ribbon. They were used for making sure that the patterned GNR just could be fabricated on the cutting gap. After development in MIBK/IPA solution, the optical image of patterned GNRs on the chip is shown in Figure 2.15 (b). Bare SiN film is shown by brown regions on the Si chip; thus, monolayer graphene remained on the chip, except in brown regions.

The color results confirmed that the graphene was separated among the three electrodes. Then exposed graphene was removed by O_2 plasma in RIE, as shown in Figure 2.15 (c). From the enlarged image, a narrow ribbon are suspended over the cutting-gap between source and drain electrodes. The size of this suspended GNR was measured at approximately 300 nm wide and 3μm long. Finally, the PMMA layer on graphene was removed by acetone solution. As shown in Figure 2.15 (d), after removing PMMA layer, it's hard to see the fabricated GNR by optical microscopy even under high-magnification. All the details and parameters during this process are list in Table 2.4.

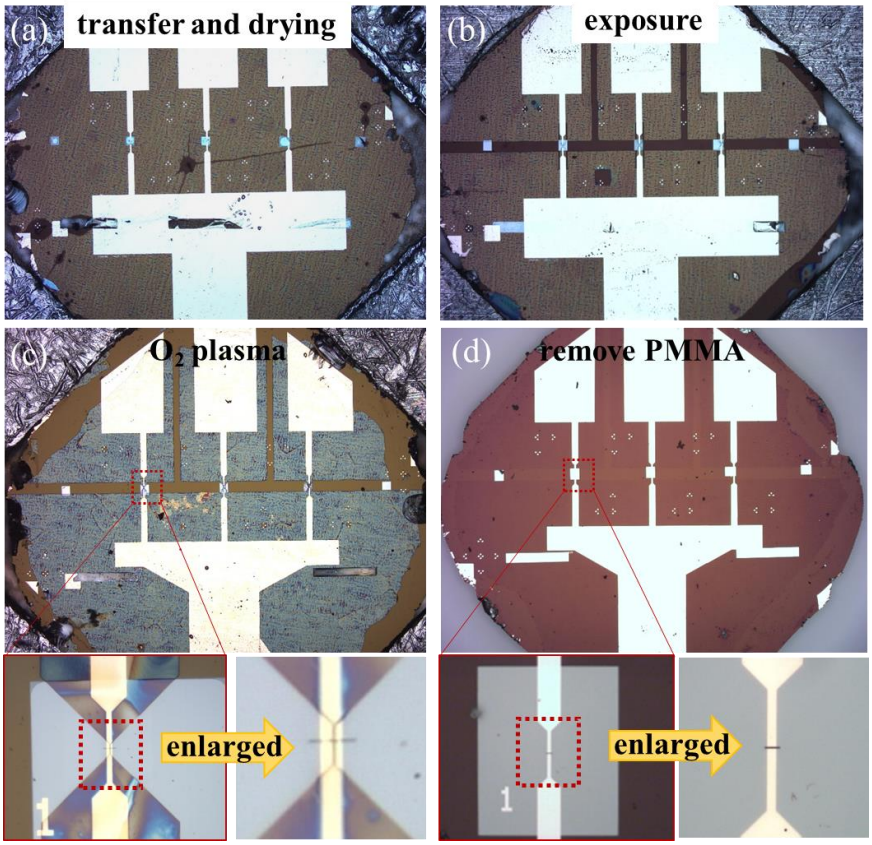

Figure 2.15 GNR fabrication in cleanroom. Photograph of TEM grid after (a) transfer

and drying of graphene, (b) exposure by EBL and development, (c) etching exposed graphene, (d) removing PMMA layer by acetone.

Table 2.4 List of 3rd steps for patterning transferred graphene.

3rd Step –Patterning of graphene		
Step#	**Step description and detail parameter**	**Optical images**
1	**Drying of the sample** Keep the sample in cleanroom for over 24 h	Figure 2.15 (a)
2	**Electron beam lithography and development** Exposure dose: 450 μC/cm^2 with 250pA current. Dose time: 1.8 μs/dot Develop in MIBK:IPA=1:3 for 3 min, MIBK:IPA=1:1 for 5 sec, rinse 30 sec in IPA.	Figure 2.15 (b)
3	**Etching exposed graphene** Using O_2 plasma by RIE (10 sccm, 25 sec, 30 W, 4 Pa)	Figure 2.15 (c)
4	**Cleaning of PMMA layer** The sample soaked in acetone solution (10 min, 10 min, 6 h~), then clean by IPA solution for 10 min	Figure 2.15 (d)

2.5 Characterization of fabricated GNRs

TEM images were used to check the size and layer number of fabricated GNRs. The low and high magnification images were acquired by JEM-ARM200F under 200 kV. As shown in Figure 2.16 (a-c), there are three suspended GNRs with different widths between the electrodes. The widths of these ribbons were measured to be 102, 395 and 798 nm, respectively, while the designed widths were 100, 400, and 800 nm, respectively. Thus, the width of the suspended ribbons was well controlled by the

exposure conditions. Then, we identified the layer number and checked the quality of GNR by high magnification TEM image. For example, as shown in Figure 2.16 (d), there are many contaminations on the surface of GNR, so it's hard to obtain the atomic image with the hexagonal structure of graphene underneath them. However, the layer number could be identified from the corresponding FFT pattern as shown in Figure 2.16 (e). The spots in the FFT pattern correspond to the (100) lattice plane of graphene (0.21 nm), which confirmed that the GNR was a monolayer.

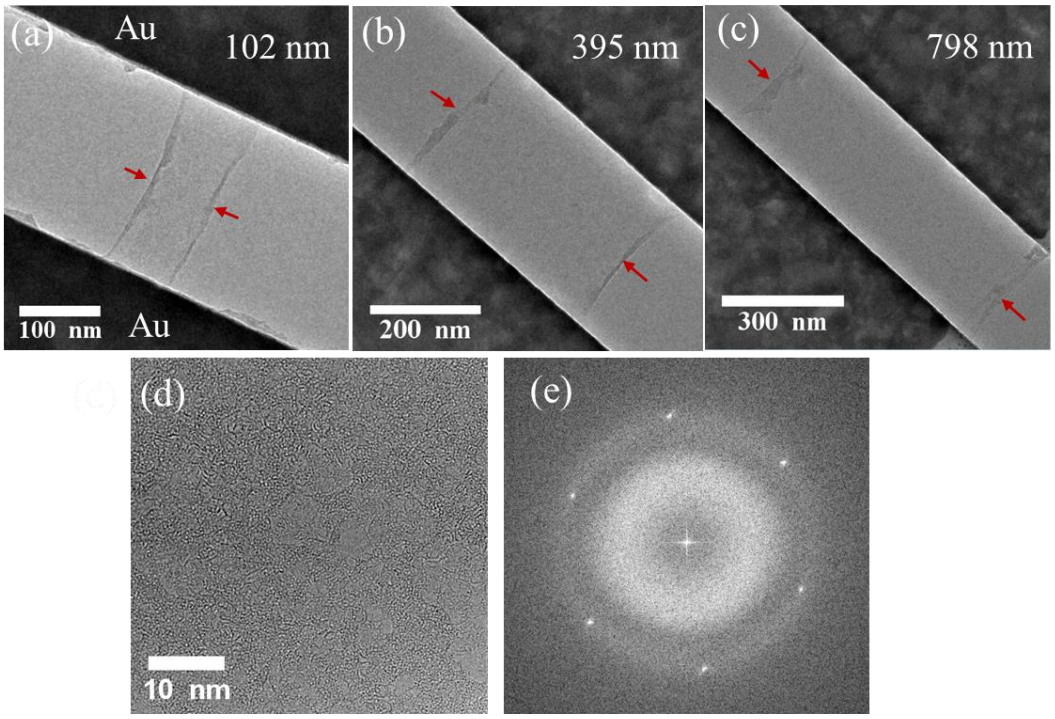

Figure 2.16 TEM images of fabricated suspended GNRs and corresponding electron diffraction pattern. (a-c) TEM images of suspended GNRs with the width of 102, 395, 798 nm, respectively. The black part indicate Au electrodes and red arrows indicate the

edge positions of ribbons. (d) High magnification TEM image of a monolayer GNR. (e) The corresponding FFT pattern to (d).

2.6 Conclusion

In this chapter, we have demonstrate the experimental setup and sample preparation. Firstly, we introduce the equipment and measurement methods used in this experiment. Then, the design of in-situ TEM holder and custom TEM chip have been explained. Finally, we showed the fabrication details of the GNR devices, which include the electrodes fabrication, cutting nano-gaps, graphene transfer and patterning. By checking the TEM images, we confirm the suspended monolayer GNRs with the width from ca.100 to 800 nm have successfully fabricated. However, there are some contaminations cover the surface of GNR after fabrication, which influence the observation of atomic structure.

References

[1]. Lu, Y.; Merchant, C. A.; Drndic, M.; Johnson, A. T., In situ electronic characterization of graphene nanoconstrictions fabricated in a transmission electron microscope. *Nano Letters* 2011, 11 (12), 5184–5188.

[2]. Qi, Z. J.; Rodriguez-Manzo, J. A.; Botello-Mendez, A. R.; Hong, S. J.; Stach, E. A.; Park, Y. W., et al., Correlating atomic structure and transport in suspended graphene nanoribbons. *Nano Letters* 2014, 14 (8), 4238–4244.

[3]. Vieu, C.; Carcenac, F.; Pepin, A.; Chen, Y.; Mejias, M.; Lebib, A., et al., Electron beam lithography: resolution limits and applications. *Applied Surface Science* 2000, 164 (1-4), 111–117.

[4]. Tatsumi, T.; Hikosaka, Y.; Morishita, S.; Matsui, M.; Sekine, M., Etch rate control in a 27 MHz reactive ion etching system for ultralarge scale integrated circuit processing. *Journal of Vacuum Science & Technology A: Vacuum, Surfaces, and Films* 1999, 17 (4), 1562–1569.

[5]. Nagase, T.; Gamo, K.; Kubota, T.; Mashiko, S., Direct fabrication of nano-gap electrodes by focused ion beam etching. *Thin Solid Films* 2006, 499 (1-2), 279–284.

[6]. Nagase, T.; Kubota, T.; Mashiko, S., Fabrication of nano-gap electrodes for measuring electrical properties of organic molecules using a focused ion beam.

Thin Solid Films 2003, 438, 374–377.

[7]. corrected Microscope, C., JEM-ARM200F. [Online].Available:https://pdfs.semanticscholar.org/9c21/86bfaa62f1dc8198b04db05d0ffa680e6735.pdf

[8]. Rodriguez-Manzo, J. A.; Qi, Z. J.; Crook, A.; Ahn, J. H.; Johnson, A. T.; Drndic, M., In situ transmission electron microscopy modulation of transport in graphene nanoribbons. *ACS Nano* 2016, 10 (4), 4004–4010.

[9]. Wang, Q.; Kitaura, R.; Suzuki, S.; Miyauchi, Y.; Matsuda, K.; Yamamoto, Y., et al., Fabrication and in situ transmission electron microscope characterization of free-standing graphene nanoribbon devices. *ACS Nano* 2016, 10 (1), 1475–1480.

Chapter 3 Graphene cleaning methods

Introduction

This chapter introduced several different methods for cleaning the surface of graphene nanoribbon. Including: dry-cleaning with adsorbents (heating with active carbon), heating in vacuum by using a heating holder, heating in gas environment (Ar/H_2), and in-situ current annealing (Joule heating). By checking the cleanliness of GNR from high-resolution TEM images, we compared the above cleaning methods and found the most suitable and effective method.

3.1 Consideration on cleaning of graphene

The properties of graphene have proved to be very sensitive to the surface contamination, which degrade the excellent optical and electrical conductance properties of graphene.[1, 2] Residues on the surface of graphene also result in an unintended doping effect and unstable electrical performance due to nonuniform charge accumulation at the interface between the electrode material and graphene.[3] So achieving ultraclean graphene samples is a key issue for investigating the intrinsic electrical conductance properties of graphene. Unfortunately, polymeric residues, impurity particles and other contaminants are easily involved during the lithography process, which is essential for the fabrication of GNR devices. The surface contaminants are typically composed of hydrocarbons with wide variation in their stoichiometry (C = O, C-OH, or H-C) and chain lengths.[4] Such contamination can be cross-linked and/or graphitized under the electron beam of a TEM[5] or at high temperatures.[6, 7] It is therefore considerably difficult to obtain an ultraclean graphene sample. In order to reduce the contamination on the graphene, cleaning is usually recommended after the fabrication[1, 8-10].

Until now, various treatments have been used for cleaning the surface of graphene, such as: heating treatment in a vacuum or gas environment, dry-cleaning with adsorbents, plasma etching, in-situ current annealing and so on. Heating treatment is

one of the most common methods for removing hydrocarbon contamination from surfaces. Although annealing of graphene in vacuum or inert atmosphere reduces the amount of contamination,[11, 12] it has been shown that residuals are still present after such treatment.[13] If the heating is insufficient, many contaminants will remain; if the sample is over-heated, obvious defects may occur, especially for the suspended graphene. This will hinder the investigation of the intrinsic properties of graphene.

Recently, a different approach for cleaning graphene was developed: the use of a metal-catalyst (Pt or Pd) to aid in the removal of surface contamination[14] on graphene. Although this method can remove efficiently contamination from graphene at moderate temperatures (300°C) and under atmospheric conditions. However, depositing metals on the sample surface is not desirable, especially for our fabricated GNR devices which are used for electronic applications.

Since it is difficult to find a uniform and proper cleaning condition for specific graphene devices, especially for suspended GNRs, we will try several different cleaning methods and find the most suitable one for our devices in this chapter.

3.2 Dry-cleaning with adsorbents

Here, we present a special cleaning method, dry-cleaning with adsorbents which has been reported in 2014.[15] They observed surface cleanness of 95% in single layer

graphene, when embedding free-standing single-layer graphene supported on Quantifoil TEM grids in commonly used adsorbents-activated carbon (Merck, "charcoal activated for analysis"). It seems that this method is very simple and effective.

Following their method, we tried to clean the surface of GNR which fabricated on TEM grid. For comparison, we tried to clean two different types of sample. One sample is transferred graphene on typical copper TEM-grid, another one is custom Si/SiN grid with fabricated GNRs. Both of them were embedded in a powder of activated carbon inside a glass vial. Then, this vial was placed on a hot plate, which was heated from room temperature to ~210℃ at a rate of 5 ℃/min. The sample was held at this temperature for 30 min. Afterwards, these sample were cooled to room temperature and blown gently with air before inserting them in the TEM to remove remaining active carbon from the surface of the samples.

As shown in Figure 3.1, it shows the TEM images of these two samples before and after cleaning process, which were took by ARM-200F at 200 kV. Figure 3.1 (a-c) shows the TEM images of transferred graphene on copper foil before and after heating with active carbon. The sample surface covered with contamination with only small patches of clean graphene as shown in Figure 3.1 (a), which is a typical non-cleaned graphene sample. After dry-cleaning with active carbon, the cleanness is improved, as shown in Figure 3.1 (b). From an enlarged TEM images Figure 3.1 (c), the clean area

of graphene could reach to the size of some tens of nanometer. However, when using the same method with fabricated GNR devices, it seems not effective. As shown in Figure 3.1 (d), the initial GNR is non-clean surface, with the width of 184 nm. After heating with active carbon, we didn't see obvious cleaning effect of the surface in Figure 3.1(e). At the same time, we found that the width reduced to 150 nm. From the enlarged TEM image of Figure 3.1(f), some residual contamination still existed on the ribbon and several large holes have been formed. One of the reason is that only the contamination area where activated carbon was adsorbed could be cleaned. Considering the size of active carbon particle with micrometer (50-150 μm), it's hard to contact with our fabricated GNR due to small size. Another reason is the properties of PMMA resist may be changed by lithograph and development, which makes the cleaning of the GNR harder.

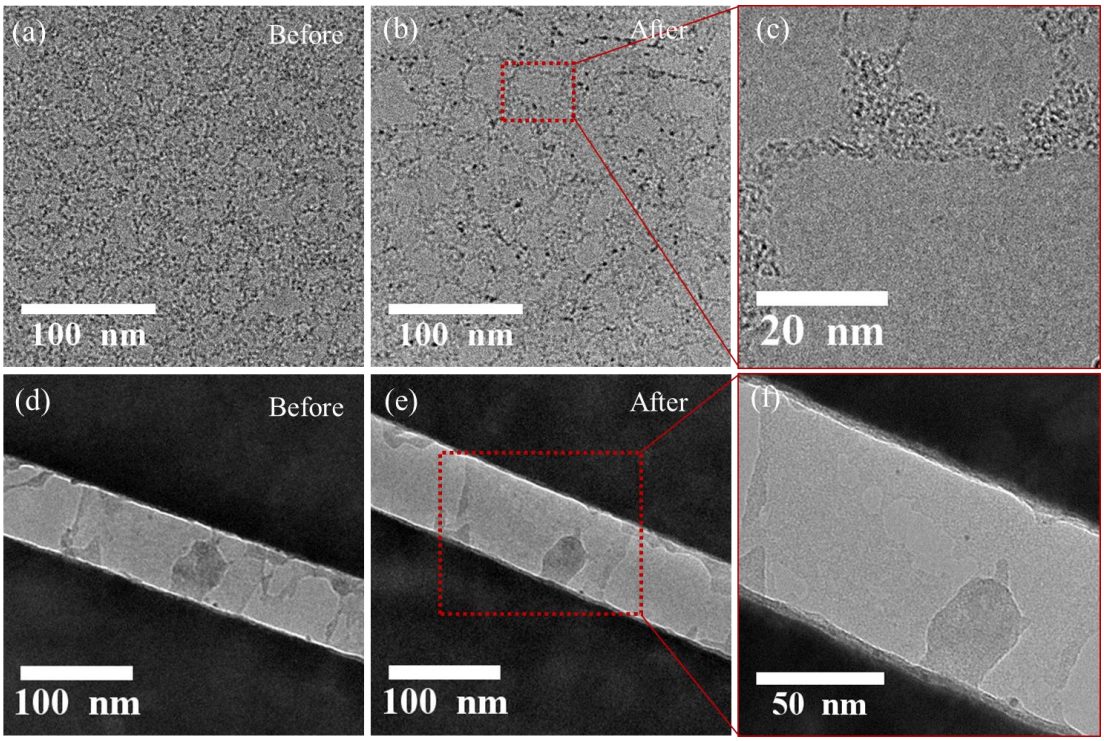

Figure 3.1 Dry-cleaning effect of graphene with active carbon. (a-c) TEM images of transferred graphene on copper TEM-grid before and after dry-cleaning. (d-f) TEM images of fabricated GNRs on custom Si/SiN grid before and after dry-cleaning.

In conclusion, the dry-cleaning method with activated carbon is effective for large-area transferred graphene on TEM grid without lithography step. However, it is not effective for suspended GNRs with size of nanometer. This method have the possibility to damage the suspended graphene during heating or blowing activated carbon, snice the adsorbed active carbon on the sample is very hard to remove totally by blowing gently with air.

3.3 Two-step annealing in gas environment

Two-step annealing is the most common method for cleaning GNRs fabricated on the Si/SiO_2 substrate. Two-step annealing means annealing the sample in air followed by another annealing in H_2/Ar mixture gas. This method can effective remove PMMA residue and provide the cleanest graphene surface.[8]

In our experiment, we first heated our sample on a hotplate at 200℃ in air for 30 min in cleanroom. If the annealing time is too long (>30 min), the presence of oxygen will induce the defect formation. Then, this sample moved to an infrared furnace (ULVAC VHC-P610CP) and annealing in mixed gas ambient of Ar +H_2 (9: 1) at 300℃ for 2 h or 450℃ for 3 h. The infrared lamp furnace is shown in Figure 3.2.

Figure 3.2 Photograph of infrared lamp furnace.

Figure 3.3 shows a monolayer GNR with width of 237 nm, which was cleaned by two-step annealing method. Comparing the high magnification of TEM images taken before (c) and after (d) annealing, the edge of ribbon became straight after heating, however, there are still many contaminations on the surface of graphene. Then we tried to anneal other sample with increasing heating temperature and keeping for longer time.

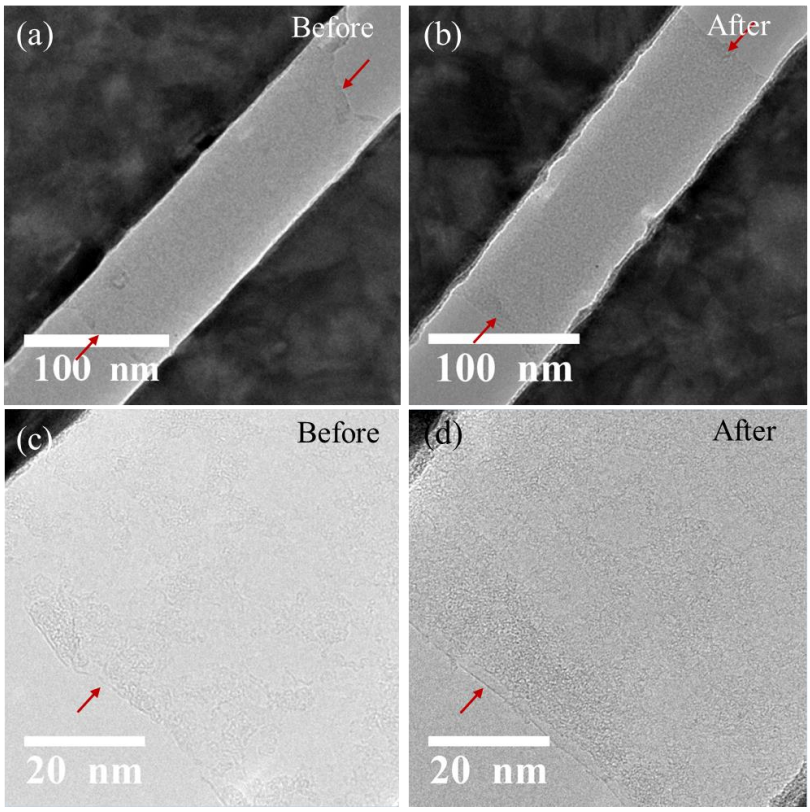

Figure 3.3 Low and high magnification of TEM images of graphene before (a, c) and after (b, d) air and Ar +H_2 two-step annealing at 300 °C for 2 h. The red arrows indicate the edge of ribbon.

We used the same method to clean other sample with the temperature at 450 °C for 3 h. As shown in low magnification TEM images of Figure 3.4 (a) and (b), we didn't find obvious change of the surface. The enlarged TEM images show that the contamination on the surface still existed. In addition, when the temperature is much higher than 300 °C, defects were sometimes formed on graphene or the ribbon was ruptured. In conclusion, this two-step annealing method is not effective for cleaning the

surface of suspended GNRs.

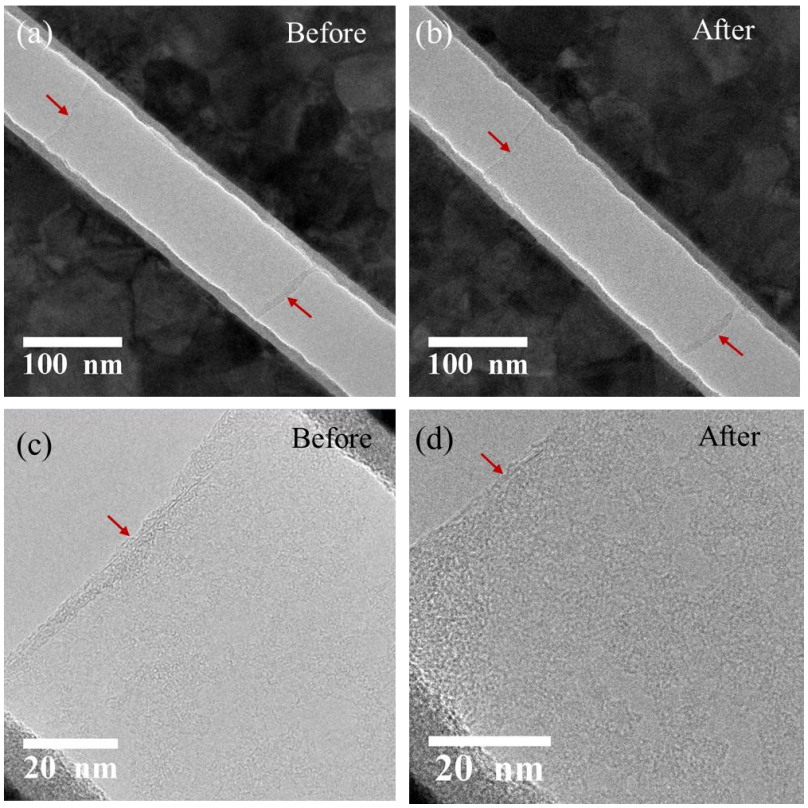

Figure 3.4 Low and high magnification of TEM images of graphene before (a, c) and after (b, d) air and Ar +H_2 two-step annealing at 450 °C for 3 h. The red arrows indicate the edge of ribbon.

3.4 Thermal annealing in vacuum

As we discussed above, there have been many methods to remove the PMMA residues, among which thermal annealing in vacuum is the most widely applied.

For cleaning the surface of graphene, the fabricated sample was loaded in an in-

situ heating holder and annealed in the TEM column under high vacuum (pressure 10^{-5}~10^{-6} Pa) to remove adlayers of polymeric residues on the surface. The heating holder: EM-31670SHTH is shown in Figure 3.5, which is fabricated by JEOL Company; the temperature is controlled by a heater control unit which linked with holder as shown at the lower left corner. For investigating the cleaning effect of this method, we set the temperature from 300~450 °C and keep the temperature for at least 6 h.

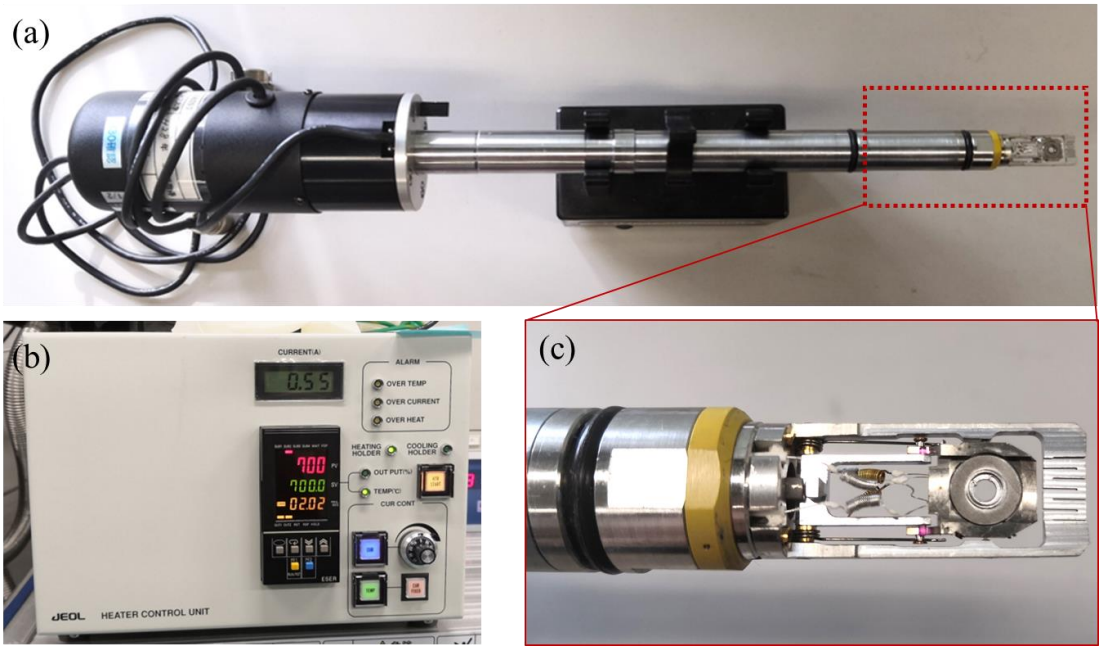

Figure 3.5 Photograph of a heating holder (a) and linked additional heater control unit (b) for controlling the temperature. (c) An enlarged image at the head of holder, where we loaded the sample

The high resolution TEM images of graphene before and after annealing in vacuum

are shown in Figure 3.6. As shown in Figure 3.6 (a), there are many PMMA residues on the surface of graphene after fabrication. PMMA residues were relatively thin in some places and such thin PMMA residues consist of one PMMA layer, which was directly adsorbed on the surface of graphene, and another PMMA layer, which was deposited on the former PMMA layer. The former one, which shows light contrast as indicated by a red square in Figure 3.6(a), is named PMMA-G, since it faces the graphene. On the other hand, the latter one, slightly darker contrast as indicated by a yellow square in Figure 3.6(a), is named PMMA-A, since it faces the air. Normally, after a typical electron beam lithography, 3-5 layers of PMMA-A left on the surface of graphene. PMMA-G only indicated the last layer of PMMA that seems to make contact with graphene. [8] After heating in the vacuum at 300 °C for 6 h, some part of PMMA-A disappeared, which means that the decomposition temperature of PMMA-A must be relatively lower. Then the temperature was increased to 380°C and kept for 6 h. As shown in Figure 3.6 (c), the image contrast of PMMA became brighter, indicating that the amount of PMMA-A was reduced due to heating. Until heating to 400°C, only PMMA-G was remained on the surface of graphene, since slightly dark of PMMA disappeared. However, the remained PMMA-G could not be remove when increasing the temperature to 450°C for 24 h. The PMMA-G layer seems only to be melt under the high temperature, however, it seems not to be evaporated from the surface.

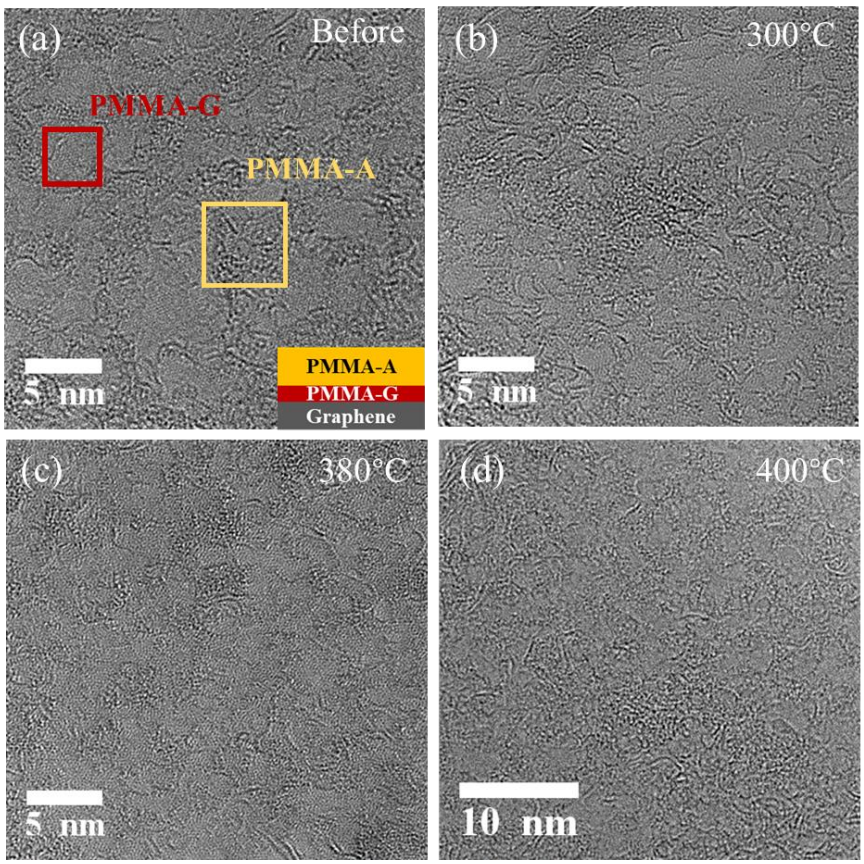

Figure 3.6 High magnification TEM images of graphene before (a) and after annealing in vacuum at 300 °C (b), 380 °C (c) and 400 °C (d) for 6 h, respectively. The colorful square in (a) indicate the different layer of PMMA.

In conclusion, thermal annealing in vacuum by using heating holder in TEM can make the surface of graphene clean partially. However, there are some obvious disadvantage in this method. Firstly, this method spend long time for cleaning, usually more than 6 h. Secondly, the cleaning effect depends on the sample. Sometimes it was not effective. Most of important, thin PMMA layer is remained on the surface of

graphene, which can't be removed totally.

3.5 In-situ current induced-annealing

In this part, in-situ current induced-annealing inside the TEM chamber is presented. This method is based on the application of a source-drain bias voltage of a few volts across the sample, which induce a large current flow through the graphene device and generate several tens of milliwatts dissipation over hundreds of nm^2 surface area.[16] Then, we could check the cleaning effect by TEM observation almost at the same time with cleaning. These cleaned graphene devices allow us to measure the intrinsic electrical conductance properties. For obtaining the atom-resolved TEM images of graphene, TEM observations were conducted using a 50 pm resolved aberration-corrected TEM (JEOL R005) in Tokyo Institute of Technology, which operated at 80 kV and under a pressure of 10^{-6} Pa.

3.5.1 The damage of GNR under electron beam before cleaning

As we discussed above, the GNR fabricated by EBL had many contaminants on the surface associated with lithographic processing (mainly resist residue), as shown in Figure 3.7 (a). When such a contaminated GNR was irradiated with an incident electron

beam, it was observed to be easily destroyed. Many holes were easily formed near the contaminants on the surface of the contaminated GNR during TEM observation (Figure 3.7 (b)). Finally, the GNR was ruptured by accumulation of holes, as shown in Figure 3.7 (c). As one of the reasons, we suppose that the strong sp2 covalent bond was weakened by bonding with contaminants. To achieve fabrication of narrower GNRs controllably, the contaminants seemed to be removed as much as possible.

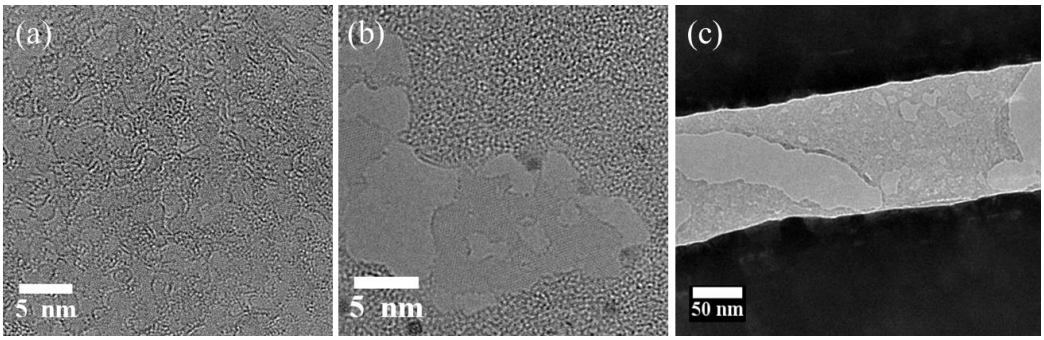

Figure 3.7 The damage evolution of GNR under electron beam irradiation (80 kV) before cleaning. (a) Initial graphene surface with contamination, (b) large holes have been formed after observation, (c) the final ruptured GNR.

3.5.2 Current annealing process of GNR

The contaminants on the surface of the GNR were removed by current annealing (Joule heating), as previously reported. [6, 16] In the current annealing process, special care has to be taken to preserve the integrity of the device upon applying large bias

voltage. It was done as follows: a bias voltage (V) was applied between two electrodes, and was gradually increased at a speed of 5 mV/s from 0 up to 2.5 V, as shown in Figure 3.8 (a). During this process, we hold the bias voltage constant to monitor the time dependence of the current. If current stays constant for a certain time, we keep on increasing voltage. Such voltage increment was repeated until the current started increasing continuously at a fixed bias. Annealing was performed inside the TEM at 10^{-6} Pa. This vacuum level is sufficiently high to prevent the oxidation of graphene by heating. The resistance evolution of the GNR during the annealing is plotted in Figure 3.8 (b). The resistance gradually decreased from ca. 74 to 8 kΩ, which was attributed to the removal of resist residue (or recovery of sp2 covalent bonds of graphene) and lowering of the contact resistance between graphene and the Au electrodes.

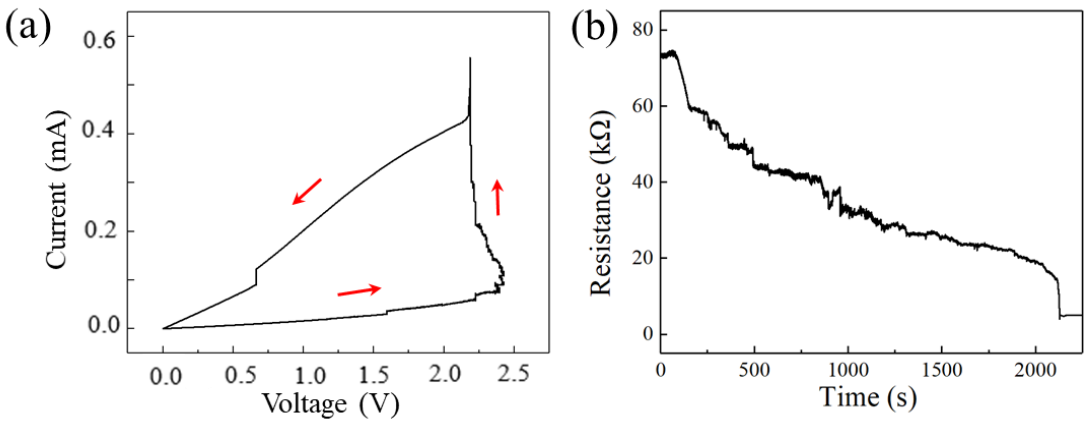

Figure 3.8 The electrical measurement of the suspended GNR during current annealing process. (a) Current versus bias voltage measurement during current annealing. (b) The

corresponding time evolution for the resistance of GNR.

As shown in Figure 3.9, the low-magnification and high-resolution TEM (HR-TEM) images taken before (a-c) and after (d-f) annealing clearly shows the removal of resist residue on the surface of graphene. The contaminations were removed just as evaporated from the surface by heating. An HR-TEM image taken after annealing shows that the monolayer GNR is clean in most areas as shown in Figure 3.9 (f). In addition, the lattice orientation of graphene was unchanged by annealing because the hexagonal spots appear at the same position in both FFT patterns (insets of Figures 3.9 (c) and (f)). After cleaning, the GNR was resistant to electron beam irradiation and was thus not readily destroyed. Vacancies in GNRs were sometimes formed by electron beam irradiation, but soon disappeared. Therefore, a strong electron beam was necessary to form a hole. We consider that this clean GNR is suitable for further controllable sculpting.

Therefore, current induced-annealing is the most suitable method for suspended GNR devices. This process is necessary not only to obtain the electrical conductance behavior of intrinsic GNRs, but also for the controllable sculpting of GNRs.

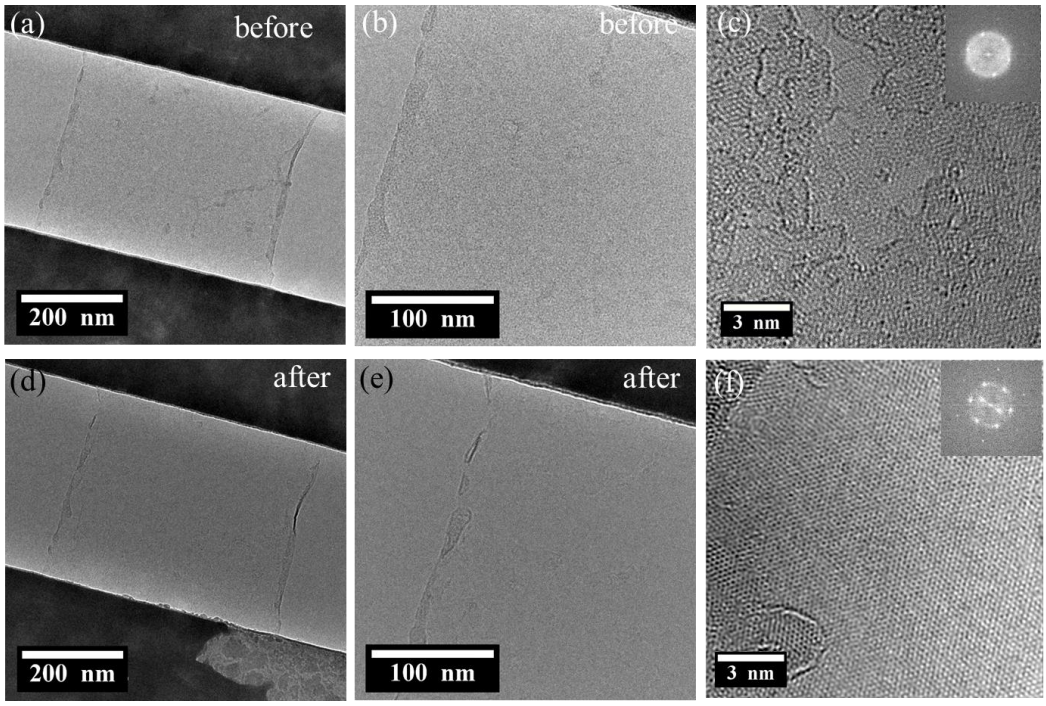

Figure 3.9 Current annealing process of GNR inside the TEM. (a-c) Low magnification and HR-TEM micrographs of a monolayer GNR before annealing. (d-f) The corresponding low magnification and HR-TEM micrographs after current annealing. Insets in (c) and (f) are the corresponding FFT patterns.

3.5.3 The mechanism of in-situ current annealing

For investigating the mechanism of current-induced annealing, the annealing process was observed by in-situ TEM observation under 80 kV electron beam. The TEM images were taken in each 5 min simultaneously with recording the current and voltage. The time evolution of current, voltage, resistance and power are shown in Figure 3.10 (a-d), respectively. All this cleaning process spent over 30 min with the bias

voltage up to 2.6 V. The red point from 1 to 7 indicate the sequence for capturing TEM images. From point 1 to 7, the current and power increased with the time, at the same time, the resistance reduced. The decrease of resistance is due to the removal of contamination and improve of electrical contact between graphene and Au electrode as we mentioned in Chapter 3.5.2. During annealing process, the voltage is fast increased from 1.0 to 2.6 V (point 1 to 3), then it was decreased gradually for monitoring the time dependence of the current. Note that if the current increases acceleratingly, the GNR will be rupture.

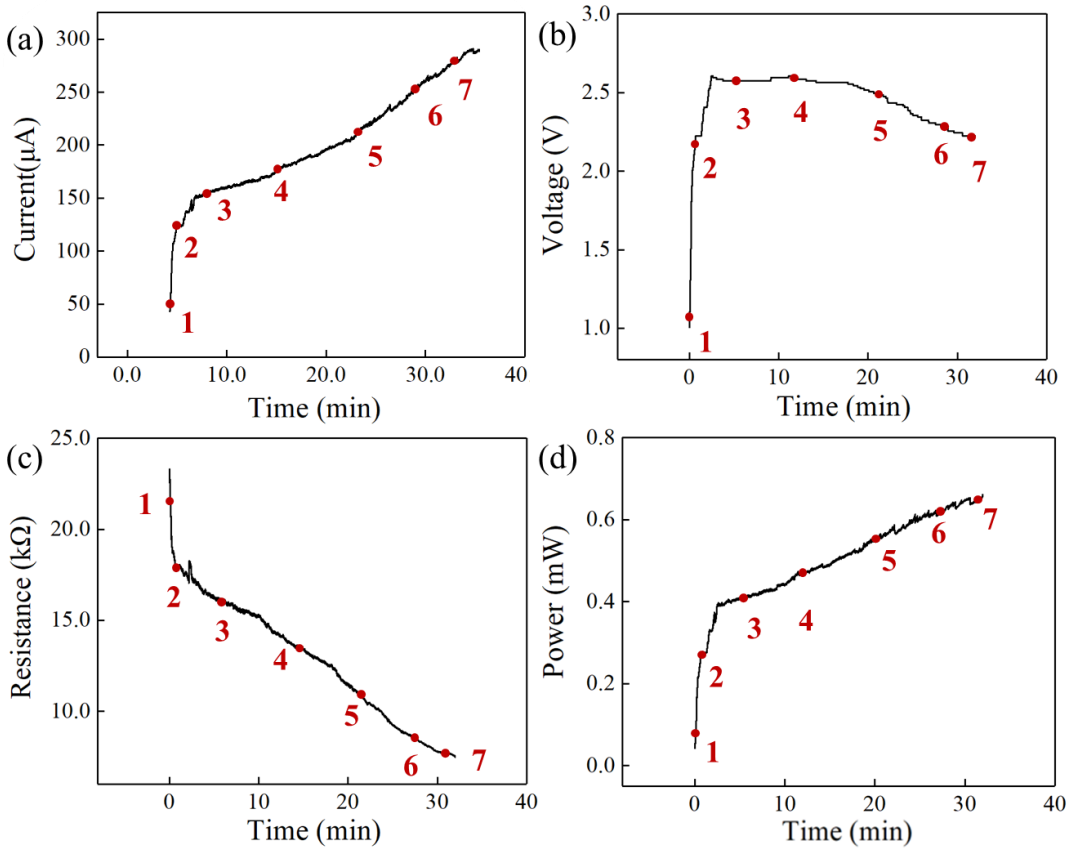

Figure 3.10 Time evolution of current (a), voltage (b), resistance (c) and power (d)

during current annealing process. Red point indicate the sequence for capturing TEM images.

The schematic of current annealing process is shown in Figure 3.11 (a). Since the bias voltage was applied to the right electrode and the ground was connected to the left electrode, electrons flowed as indicated by blue arrow. The corresponding TEM images of point 1-7 are shown in Figure 3.11 (a)-(g), which were captured during annealing process. For clearly visualizing the cleaning effect of current annealing, all TEM images were taken under over focus condition, since the contrast of monolayer graphene is too low. At the beginning, the surface of GNR was covered by many contaminants. An obvious large circle existed at the bottom of GNR, which seemed the adsorption of polymers. When the bias voltage was increased, the contaminants on the surface started to be removed by evaporation or sublimation, the contaminants started to disappear at the left side of ribbon where near the big circle. In Figure 3.11(b), the cleaning started at the position indicated by an orange arrow. Then the cleaning area expanded from left to right side of GNR, as the increase of current and power, shown by orange dashed line in Figure 3.11 (b-g). After 31 min of the high current-cleaning process, most contaminations were removed from the ribbon, although very little ones remained near the electrodes, as shown in Figure 3.11 (g). We contributed this cleaning process to the

high temperature during the application of high bias voltage. The contaminations can be evaporated or sublimated at high temperature.

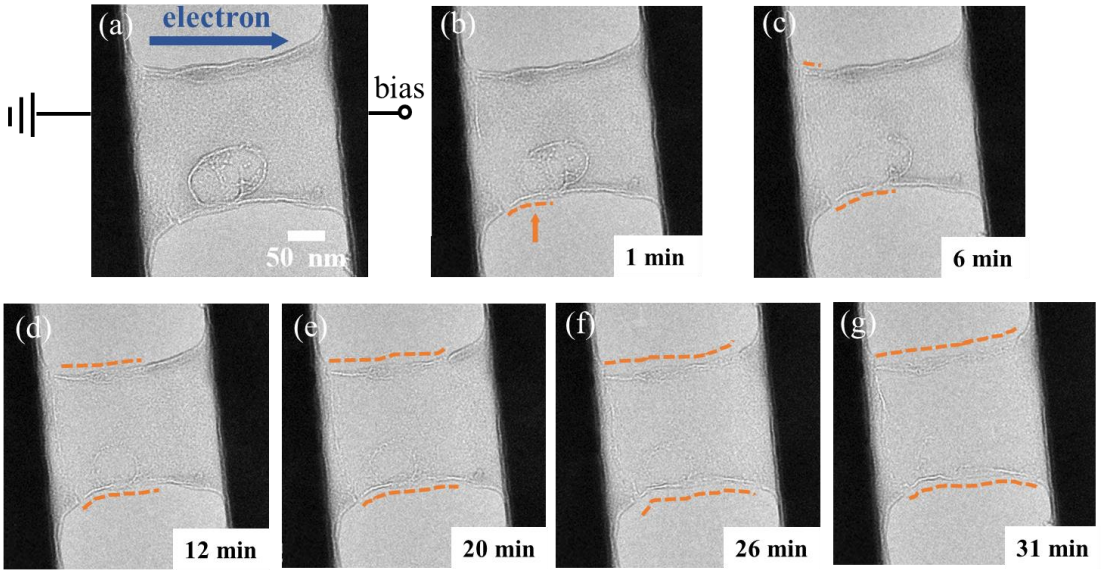

Figure 3.11 Simultaneous TEM images during current annealing process. (a) The schematic of annealing process, which shows the direction of flowing electrons by blue arrow. (a-g) TEM images corresponding to point 1-7 in Figure 3.10, respectively. The orange dashed line indicate the clean region.

For investigating the cleaning direction during current annealing, we checked the GNR devices before and after current annealing by using TEM. Figure 3.12 (a-c) are typical TEM images of the SiN windows where the GNRs were suspended: Figure 3.12 (a) was obtained before the current annealing process, and Figure 3.12 (b) and (c) were

obtained after it. Figure 3.12 (b) shows circle pattern, while, Figure 3.12 (c), half circle pattern. We found that the center of the circle was almost the middle of the GNR, while the center of the half circle was shifted towards the left electrode. Taking into account that such circle pattern appeared after making the GNR clean, we supposed that the formation of circle patterns may related with the evaporation or sublimation of contaminants by high temperature during current annealing. The temperature inside the circle patterns may be high enough for removing the contaminations.

For understanding these phenomena, we considered local Joule heating, which was generated at the left electrode, GNR and right electrode and thermal diffusion rate, because local temperature is basically determined by the balance between local Joule heating and thermal diffusion rate. Since Joule heating is proportional to the resistance at constant current, it is expected to be higher with increasing the resistance. Roughly, local thermal diffusion rate is thought to be inversely proportional to the local resistance. Therefore, the relationships among the contact resistance at left and right electrodes and the resistance of the GNR is critical.

Based on the consideration, the temperature is almost the same between both left and right electrodes when the contact resistance is almost the same between them. While, it is higher at the left electrode than at the right one, when the contact resistance is higher at the left one. These seem to be reasonable, because they explain that the

center of the circle is at the middle of GNR and one of the half-circle is shifted towards the left electrode, which contact resistance may be high. It suggests that such circle pattern may correspond to the temperature distribution during the current annealing.

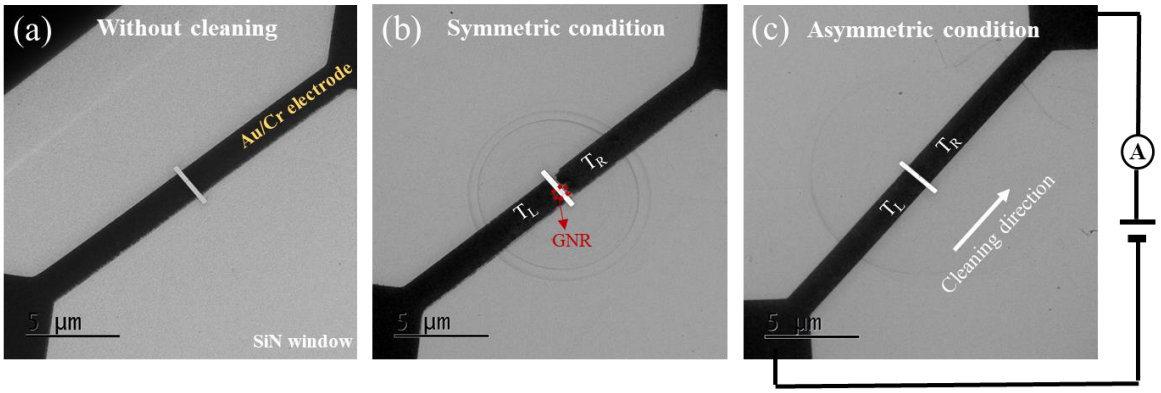

Figure 3.12 Low resolution TEM images near the suspended GNR and cutting gap inside SiN window. (a) GNR device without annealing process, (b,c) GNR devices after current annealing. In (b), some symmetrical circle shapes existed and centered on the GNR. In (c), only a half-circle existed near the left electrode.

3.5.4 Finite element method simulation of suspended GNR devices

For deeply understanding the temperature distribution on our GNR device during current annealing, a finite element thermal simulation was done by commercial software COMSOL Multiphysics^{TM}. Dr. Sankar in Mizuta lab contributed to this work.

The simulated region were limited to the SiN membrane window of 40 × 30 μm and the Cr/Au electrodes were placed on the membrane inside this region. The size and thickness of the SiN membrane, Cr/Au electrode and GNR were set according to the actual values. The temperature raise of surrounding Si chip is negligible, because it acts as large heat sink for the power generated on GNR by current annealing. The temperature at two boundary edges of simulated SiN membrane window was fixed at room temperature (300 K). During simulation, convective heat dissipation to the surrounding gas atmosphere is negligible, as the current annealing process is typically done inside TEM chamber with high-vacuum condition (10^{-6} Pa).

We report here the results obtained from two different contact conditions: symmetric and asymmetric condition. The symmetric condition means that the initial contact conditions with GNR are the same at both left and right electrodes. In contrast, the asymmetric condition means that the initial contact condition with GNR is obviously better or poor at the left electrode than at the right one. In simulation, such contact condition can be controlled by setting the electrical and thermal conductivity values at the contact of the electrode with the GNR. The setting parameters of electrical conductivity were calculated from our experimental data as shown in Appendix A. Figures 3.13 (a) and (b) show the temperature distribution with symmetric condition under the applied bias voltage of 2.2 and 2.6 V, respectively. The bias voltages of 2.2

and 2.6 V correspond to the starting voltage of making the GNR clean (Point 2) and the highest voltage (Point 3) during current annealing as shown in Chapter 3.5.3. The highest temperature portion is always confined to the most central region of the device, regardless of the change in the applied bias voltage. In Figure 3.13 (c) and (d), we show the temperature profiles across the central part of our device. Those two temperature profiles are symmetrical and centered in the middle of ribbon. From the enlarged view, we confirm the highest temperature portion exist at the center of suspended GNR.

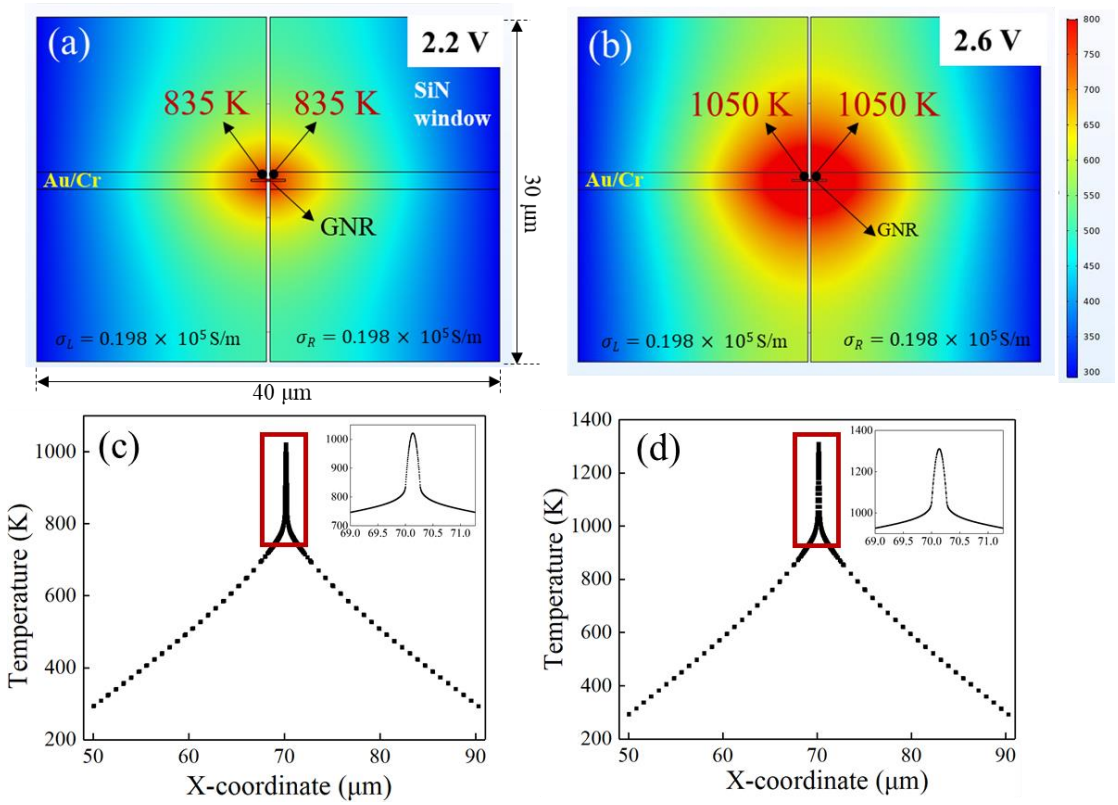

Figure 3.13. Temperature distribution of suspended GNR device under symmetric condition with different applied bias voltage. (a, b) The top view of device with Cr/Au

electrode and SiN membrane, with a color-map of the temperature distribution under an applied bias voltage of 2.2 and 2.6 V, respectively. (c, d) The temperature profile across the center of GNR device shown in (a) and (b). The enlarged view inside the red square where near the suspended ribbon and cutting gap is shown in inset.

For asymmetric condition, we assumed that the electrical and thermal conductivity values of the left electrode was one-tenth of the right one, as shown in Appendix A. Figures 3.14 (a) and (d) show the simulated temperature distribution with this asymmetric condition under the applied bias voltage of 2.2 and 2.6 V, respectively. They obviously show asymmetric temperature distribution on GNR device such that the average temperature of left side much higher than right side. The temperature difference between the regions near the edges of the left and right electrodes is 243 K at the bias voltage of 2.2 V, which increased to 380 K at 2.6 V as shown in Figures 3.14 (a) and (d). In the enlarged temperature profile near the suspended GNR of Figures 3.14 (c) and (f), we found that the temperature is always highest near the edge of the left electrode. We suppose that the contaminates start to be removed from the left side of suspended GNR, since the contaminants are evaporated or sublimated more frequently at higher temperature. In in-situ TEM observation, the contaminant-free region in the suspended GNR was observed to extend to the right side. Considering that the local resistance is

reduced by removing the contaminant in the left-side region of the suspended GNR, we think that the temperature distribution gradually shifts to the right side, which has still the contaminant remained. Therefore, our assumption well explains the experiment result. From the simulated results, we can estimate that the temperature which is necessary to remove the contaminates is about 1370 K. Because the highest temperature on the suspended GNR between electrodes is 1373 K at the bias voltage of 2.2 V, which corresponded to the staring voltage of removing the contaminates.

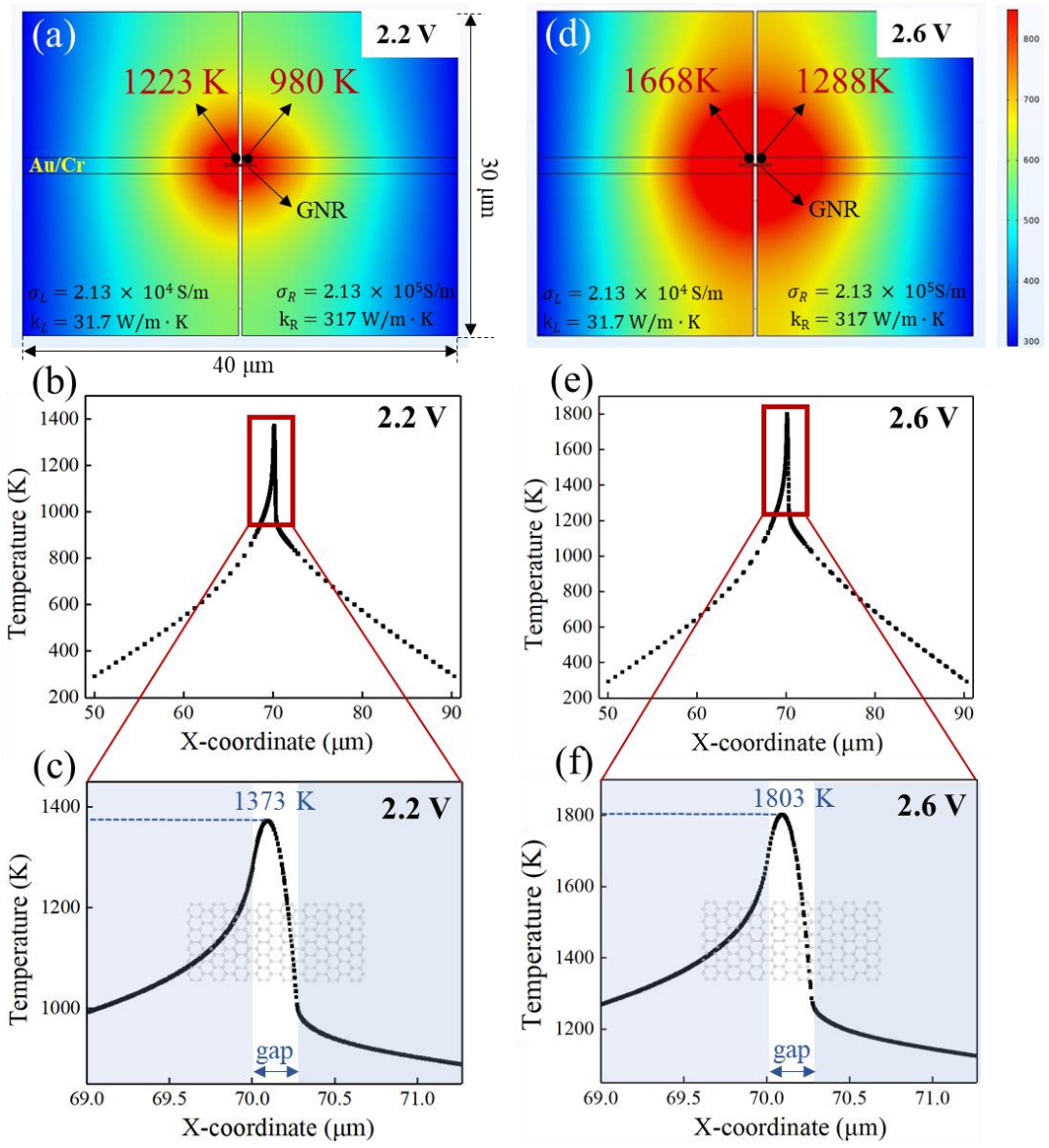

Figure 3.14 Temperature distribution of suspended GNR device under asymmetric condition with different applied bias voltage. The temperature distribution and temperature profile across the center of GNR device under an applied bias voltage of 2.2 V (a-c) and 2.6 V (d-f), respectively. The enlarged view of temperature profile inside the red square, where near the suspended ribbon and cutting gap is shown in (c) and (f) for (b) and (e), respectively.

3.6 Conclusion

In this chapter, we introduced several methods for cleaning the surface of GNR such as dry-cleaning with adsorbents (heating with active carbon), thermal annealing in vacuum by heating holder, two-step heating in gas environment (Ar/H_2), and in-situ current annealing (Joule heating). These methods were applied to make the suspended GNR clean, but it was very difficult to remove of PMMA residues perfectly on suspended GNRs after lithography and development process. Compared to the suspended GNRs, which was fabricated by lithography process, dry-cleaning with active carbon and two-step annealing methods were more effective and suitable for making transferred graphene clean. Thermal annealing in vacuum by using the heating holder could make the suspended GNR clean partially by long time heating, but it had the risk of damage the GNR devices.

In conclusion, current induced-annealing was the most suitable method for cleaning suspended GNR devices, which was helpful for the measurement of intrinsic electrical conductance properties and further nano-sculpting process. By the investigation of in-situ current annealing and the simulated temperature distribution on the GNR device, we found the relationship between the cleaning of the GNR and the local temperature.

References

[1]. Wang, H.; Zhang, X.; Takamatsu, H., Ultraclean suspended monolayer graphene achieved by in situ current annealing. *Nanotechnology* 2017, *28* (4), 045706.

[2]. Bolotin, K. I.; Sikes, K. J.; Jiang, Z.; Klima, M.; Fudenberg, G.; Hone, J., et al., Ultrahigh electron mobility in suspended graphene. *Solid State Communications* 2008, *146* (9-10), 351–355.

[3]. Dan, Y.; Lu, Y.; Kybert, N. J.; Luo, Z.; Johnson, A. T. C., Intrinsic response of graphene vapor sensors. *Nano Letters* 2009, *9* (4), 1472–1475.

[4]. Davidson, S., The use of X-ray photoelectron spectroscopy to estimate the stability of primary mass standards. *Measurement* 2007, 40 (7), 762–768.

[5]. Meyer, J. C.; Girit, C. O.; Crommie, M. F.; Zettl, A., Hydrocarbon lithography on graphene membranes. *Applied Physics Letters* 2008, *92* (12), 123110.

[6]. Westenfelder, B.; Meyer, J. C.; Biskupek, J.; Kurasch, S.; Scholz, F.; Krill, C. E., et al.,Transformations of carbon adsorbates on graphene substrates under extreme heat. *Nano Letters* 2011, *11* (12), 5123–5127.

[7]. Barreiro, A.; Borrnert, F.; Rummeli, M. H.; Buchner, B.; Vandersypen, L. M., Graphene at high bias: cracking, layer by layer sublimation, and fusing. *Nano Letters* 2012, *12* (4), 1873–1878.

[8]. Lin, Y. C.; Lu, C. C.; Yeh, C. H.; Jin, C.; Suenaga, K.; Chiu, P. W., Graphene

annealing: how clean can it be? *Nano Letters* 2012, *12* (1), 414–419.

[9]. Ahn, Y.; Kim, J.; Ganorkar, S.; Kim, Y.-H.; Kim, S.-I., Thermal annealing of graphene to remove polymer residues. *Materials Express* 2016, *6* (1), 69–76.

[10]. Xie, W.; Weng, L.-T.; Ng, K. M.; Chan, C. K.; Chan, C.-M., Clean graphene surface through high temperature annealing. *Carbon* 2015, *94*, 740–748.

[11]. Paredes, J. I.; Villar-Rodil, S.; Martínez-Alonso, A.; Tascón, J. M. D., Graphene oxide dispersions in organic solvents. *Langmuir* 2008, *24* (19), 10560–10564.

[12]. Mutus, J. Y.; Livadaru, L.; Robinson, J. T.; Urban, R.; Salomons, M. H.; Cloutier, M., et al., Low-energy electron point projection microscopy of suspended graphene, the ultimate 'microscope slide'. *New Journal of Physics* 2011, *13* (6), 063011.

[13]. Cheng, Z.; Zhou, Q.; Wang, C.; Li, Q.; Wang, C.; Fang, Y., Toward intrinsic graphene surfaces: a systematic study on thermal annealing and wet-chemical treatment of SiO_2-supported graphene devices. *Nano Letters* 2011, *11* (2), 767–771.

[14]. Longchamp, J.-N.; Escher, C.; Fink, H.-W., Ultraclean freestanding graphene by platinum-metal catalysis. *Journal of Vacuum Science & Technology B, Nanotechnology and Microelectronics: Materials, Processing, Measurement, and Phenomena* 2013, *31* (2), 020605.

[15]. Algara-Siller, G.; Lehtinen, O.; Turchanin, A.; Kaiser, U., Dry-cleaning of graphene. *Applied Physics Letters* 2014, *104* (15),153115.

[16]. Moser, J.; Barreiro, A.; Bachtold, A., Current-induced cleaning of graphene. *Applied Physics Letters* 2007, *91* (16), 163513.

Chapter 4 Nano-sculpting and in-situ electrical measurement of graphene nanoribbons

Introduction

This chapter contains the rough and precise sculpting of graphene nanoribbons, combined with in-situ electrical measurement, a part of which has been published recently [1]. The rough sculpt (>20 nm) is realized by using a convergent electron beam of a TEM microscope, and precise thinning process of sub-10 nm wide GNR by applying a high bias voltage.

In Chapter 4.1, we explain the rough sculpting procedure of graphene with TEM electron beam. In Chapter 4.2, we show the precise thinning process and restructure of of narrow GNR by applying a high bias voltage, with in-situ current-voltage measurement. In Chapter 4.3, we discuss the relationship between the resistance of GNR and width. In Chapter 4.4, we analyze the electrical conductance properties for ultra-narrow ribbons with armchair and zigzag edge structures.

4.1 Rough nano-sculpting of the GNR device

The basic mechanism of sculpting graphene by incident electron beam in TEM has been already reported in many previous paper.[1] In this study, we further optimized this technique for rough and precise sculpting of graphene.

As explained in Chapter 3.5, before sculpting, the current annealing process of GNR is necessary, which is helpful for the measurement of intrinsic electrical conductance properties and also nano-sculpting process. After that, the bias voltage was continuously maintained at 1.0 V to heat the sample, which was effective to avoid unnecessary damage and/or reattachment of contaminants onto the surface of the GNR.[2-4]

Then clean GNR was sculpted with a convergent electron beam under TEM mode with 80 kV. Because the electron energy is a little below the threshold for knock-off damage of carbon atoms from graphene (86 keV),[5] the damage of graphene lattice is less than higher acceleration voltage. During the nanosculpting process, the electron beam was converged to a spot to knock out carbon atoms. In particular, we searched for areas that were free of polymer residues and did not contain any grain-boundaries as much as possible, which can be easily ruptured by intense electron beam. By this method, the width of the GNR was narrow by irradiation with the convergent electron beam onto the edge of the GNR and moving it gradually inward, as shown in Figure

4.1. A narrow constriction of above 20 nm in width could be formed by sculpting the GNR from both sides.

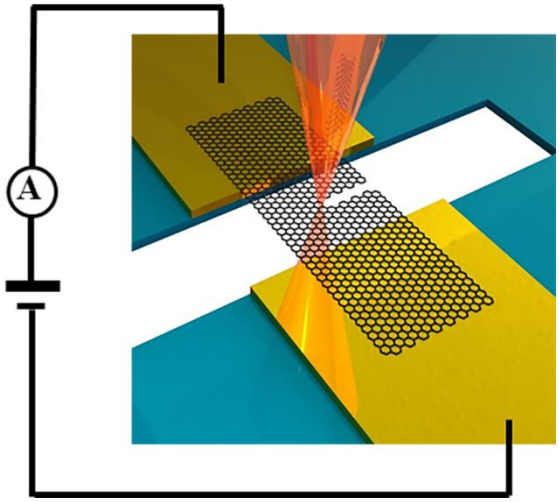

Figure 4.1 Schematic illustration of nanosculpting technique in the TEM with a convergent electron beam, with the bias voltage was continuously maintained at 1.0 V.

A series of the TEM images of the GNR which width was reduced by rough sculpting are shown in Figure 4.2 (a-e). At the beginning, we sculpted the ribbon from the upper side. After cutting the ribbon from 243 to 150 nm, we sculpted the ribbon from the bottom side. Finally, we got the GNR with width of ca. 32 nm.

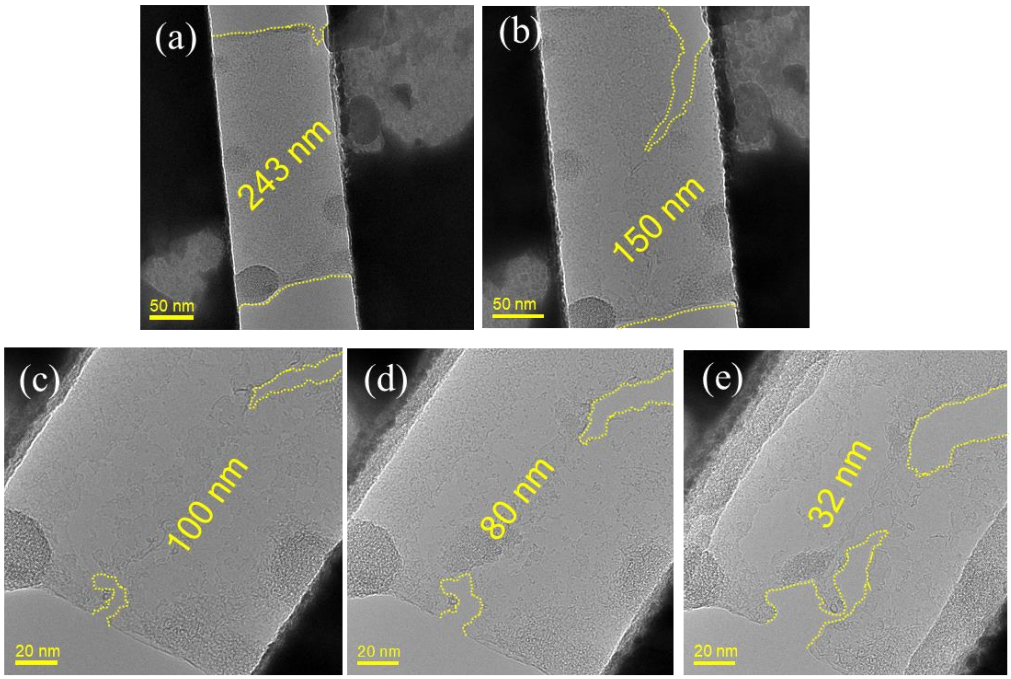

Figure 4.2 TEM images of GNR with different widths during rough nano-sculpting method. The width of ribbon reduced from 243 to 32 nm. The yellow dashed lines indicate the edge of ribbon.

After obtaining a ca. 20-30 nm wide constriction (narrow GNR), the rough nano-sculpting was stopped because it was difficult to control the width and orientation of the narrow GNR precisely due to fast etching speed.[6] After that, the further narrowing of ribbon can only realize by precise sculpting, which will discuss in later Chapter 4.2.

4.2 Precise thinning process and I-V measurement of narrow GNR

In this chapter, we introduced the precise thinning process of narrow GNR (ca. 20-30 nm). The width of ribbon was gradually thinned by the application of a high bias voltage under irradiation of a parallel electron beam.[7-8] The edges of ribbon will restructure and the width of ribbon will reduce at high temperature, which due to applying the high voltage. More details about the restructure of GNR under applying the bias voltage is explained in Chapter 5.

4.2.1 The thinning process of GNR by applying a high bias voltage

The GNR was gradually thinned by applying the high bias voltage up to 2.4 V. Such narrow GNR was observed to progressively reduce in width from ca. 20 to 0.4 nm. Figures 4.3 (a-h) show TEM images of narrow GNRs from 16.1 to 1.7 nm in width. In each TEM image, both edges were estimated to have the shapes indicated by yellow dashed lines, and the narrowest width was measured at the cross section between two yellow arrows. Although some “graphene islands” and folding structures had been formed at high temperatures,[6,9] they are not considered to have an influence on the electrical transport properties as discussed later.

In the process of Figures 4.3 (b-e), cracking was formed at the narrow GNR, which resulted in a sharp reduction in width. The orientation of the graphene near the narrow

GNR was tilted at the moment of cracking, which was identified by analysis of the FFT pattern inserted in the HR-TEM image. The edge structure of the GNR changed from a mixture of zigzag and armchair edges to only zigzag edge. The zigzag edge was maintained until breaking the GNR. We think that the electrical current is more concentrated near the narrow GNR, which may result in the introduction of cracking and tilting. The edge structure seems to change by following the orientation tilt near the narrow GNR, which occurred when the width of the GNRs was reduced from 1.9 to 1.7 nm. The GNRs in Figures 4.3 (a-g) were determined to have mixed edges (denoted MGNR), while the GNR in Figure 4.3 (h) had the zigzag edge (ZGNR).

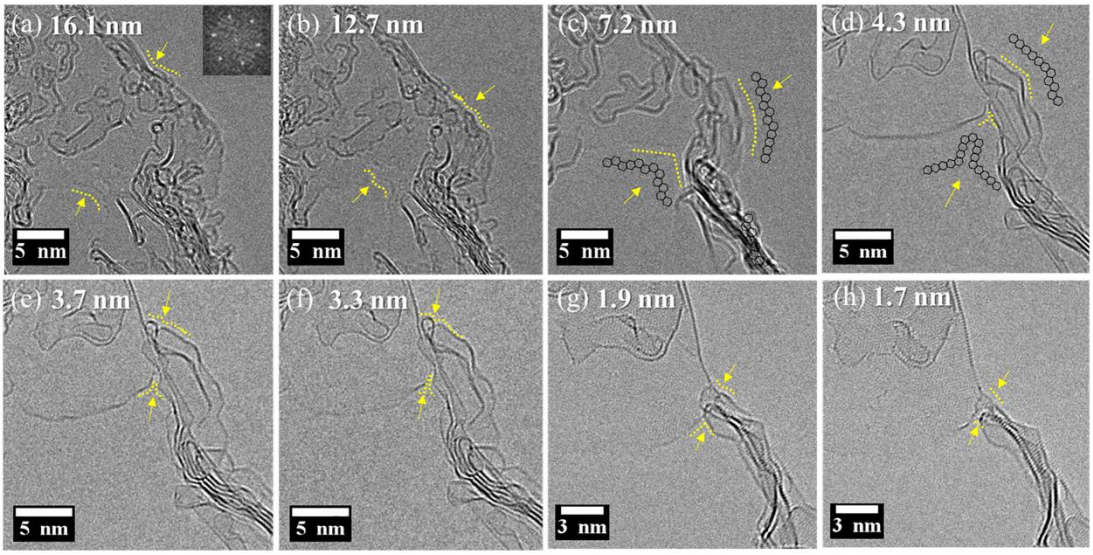

Figure 4.3 TEM images of GNRs less than 20 nm wide taken during the thinning process. (a-h) TEM images of the suspended GNR with widths from 16.1 to 1.7 nm. Yellow dashed lines indicate the shape of the edges. The cross section between two

yellow arrows are measured as the narrowest width. The orientation of edge structures are determined by comparing the edge direction and the corresponding FFT pattern, as described by the honeycomb patterns in (c) and (d). (c-g) GNRs with a mixture of both zigzag and armchair edges. (h) GNR with zigzag edges.

4.2.2 In-situ I-V measurements during thinning process

I-V curves were measured simultaneously with TEM observation of the narrow GNRs with different widths, as shown in Figure 4.4. The evolution of I-V curves of GNRs during the whole thinning process are shown in Figure 4.5. The I-V curve changed from linear to nonlinear with decreasing the width. The I-V characteristics were linear in the width range of 16.1 to 4.3 nm, as shown in Figure 4.4 (a-d). However, at widths below 3.7 nm, the I-V characteristics were nonlinear, suggesting opening of the energy gap, as shown in Figure 4.4 (e-h). In the transport gap regime, the energy gap can be estimated to be one half of the nonlinear region $\triangle V$ in the I-V curve.[10-13] The energy gaps of the MGNRs with widths of 3.7, 3.3, and 1.9 nm were estimated to be 0.1, 0.16, and 0.38 eV, respectively. These results indicate that the electrical conductance of the measured MGNR changed from metallic to semiconducting as the width decreased. In addition, the energy gap increased with the decrease of width, which is in good agreement with the previous prediction.[14-15] We found that differential

conductance-bias voltage (dI/dV-V) curves for the MGNRs showed parabolic patterns near the origin (0 V), as shown in Figure 4.4 (i-k). While, the ZGNR with a width of 1.7 nm was estimated to be an energy gap of 0.56 eV and showed sharp increase of the differential conductance at the threshold voltage in the dI/dV-V curve. The I-V and dI/dV-V curves between the MGNR and ZGNR showed obviously different patterns.

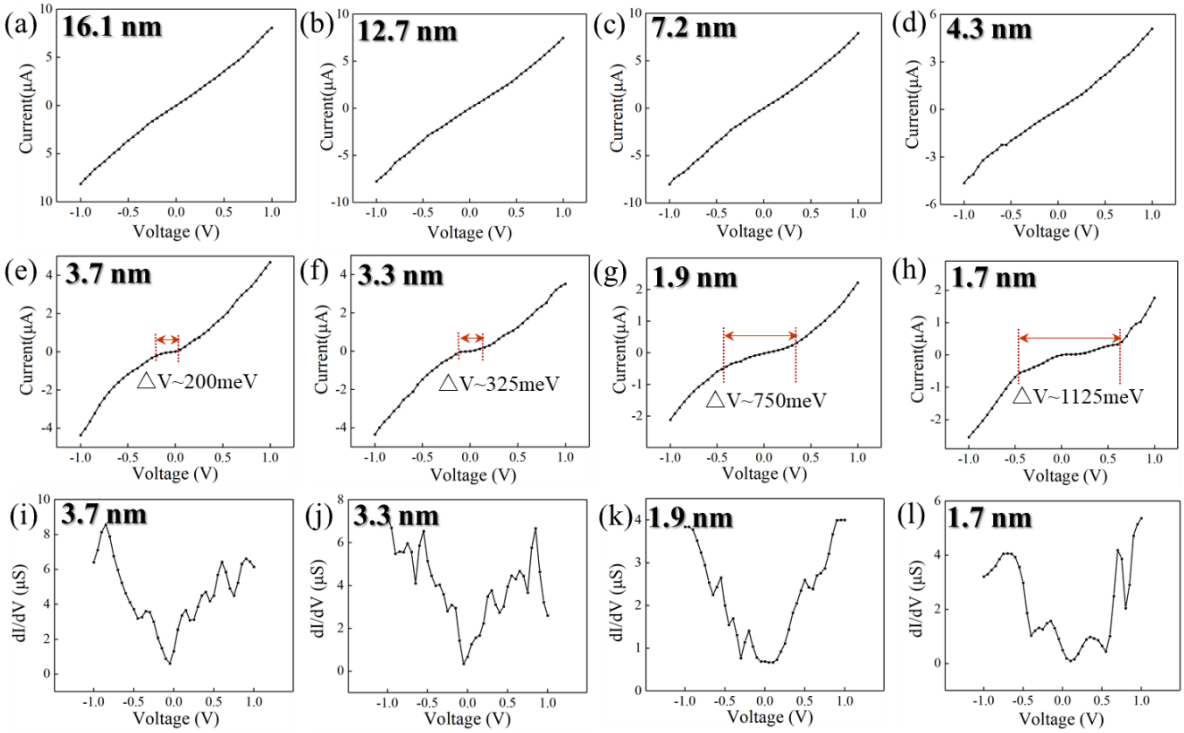

Figure 4.4 The corresponding current-voltage (I-V) and differential conductance-voltage (dI/dV-V) curves of GNRs in Figure 4.3, which measured during the thinning process. (a-h) I-V curves of the GNRs corresponding to Figure 4.3 (a-h). (i-l) Corresponding dI/dV-V curves for the GNRs in (e-h).

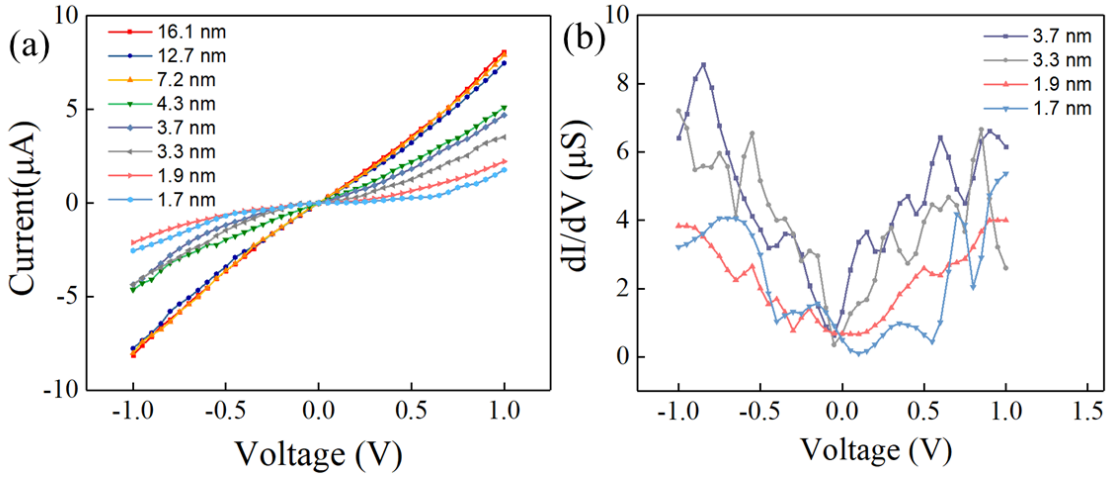

Figure 4.5 (a) I-V curves of the GNRs with widths from 16.1 to 1.7 nm. (b) Corresponding dI/dV-V curves for the GNRs with widths from 3.7 to 1.7 nm.

4.2.3 Formation of ultra-narrow zigzag edge-graphene nanoribbon

Ultra-narrow monolayer GNRs with perfect zigzag edge structure were finally obtained. Figure 4.6 shows a TEM image of a GNR with a width of 1.5 nm. The FFT patterns of the HR-TEM images confirmed that both straight edges of the 1.5 nm wide GNR were oriented along the zigzag direction, as shown in Figure 4.6 (b). Folding and wrinkled structures seem to be formed near the narrowest ribbon, as shown in Figure 4.6 (d); the simulated TEM image (Figure 4.6 (c)) based on the structural model (Figure 4.6 (d)) including folding and wrinkled structures reproduces the experimental TEM image (Figure 4.6 (b)). The simulation method of TEM images and analysis will be introduced in next Chapter 4.2.4. Folding and wrinkled structures seems to be formed

frequently at high temperatures, as reported previously.[9,16]

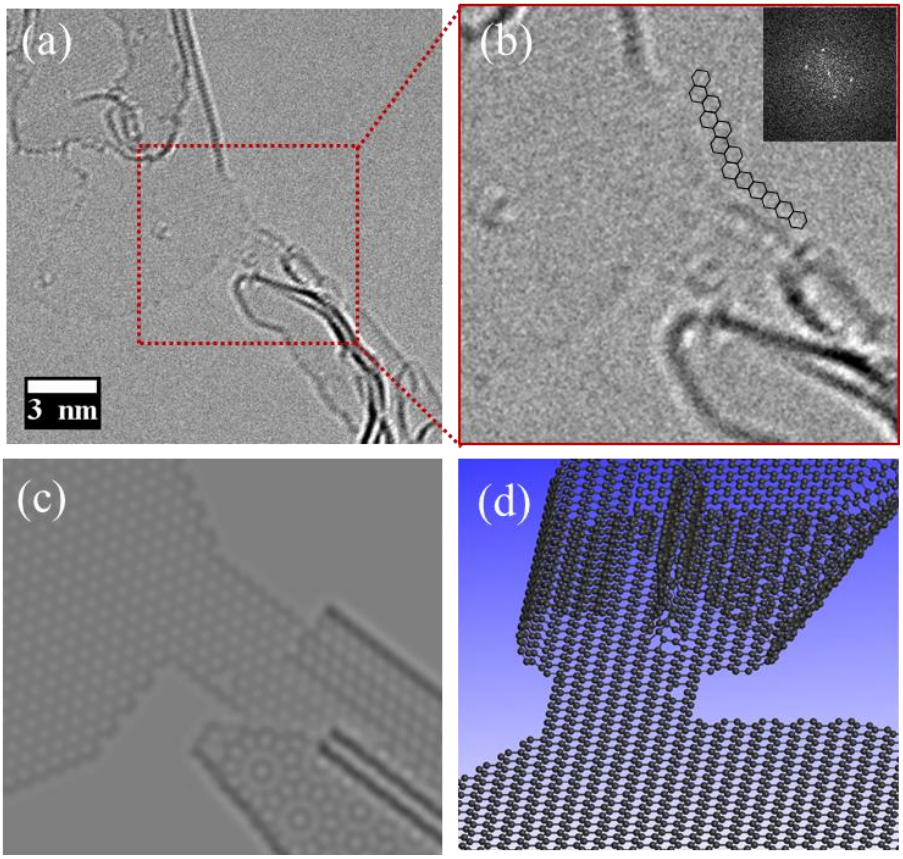

Figure 4.6 TEM image, I-V curve, and dI/dV-V curve for ultra-narrow GNR with zigzag edges (ZGNR). (a,b) TEM image of 1.5 nm wide ZGNR. The inset shows the corresponding FFT pattern. (c) Simulated TEM image of the model structure shown in (d), which well reproduces the experimental TEM image in (b). (d) Schematic illustration of 1.5 nm wide ZGNR and. Folding and wrinkled structures are formed near the ZGNR.

In addition, ZGNRs of 1.2, 0.7, and 0.4 nm in width could be obtained as shown

in Figure 4.7. Analysis of these FFT patterns for the ultra-narrow GNRs confirmed that the edge was the zigzag structure. These results indicate that ultra-narrow GNRs with well-defined edge structures can be fabricated by convergent electron beam nanosculpting followed by current annealing.

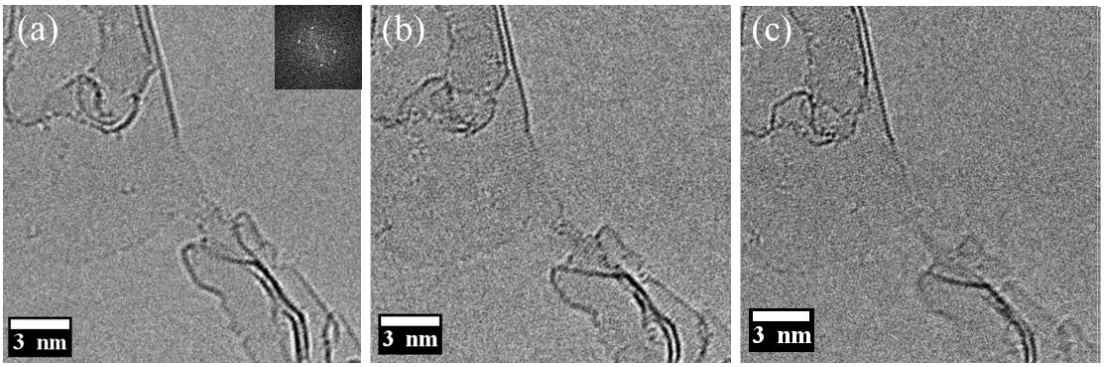

Figure 4.7 The TEM images of ultra-narrow ZGNRs. (a-c) The high-resolution TEM images of narrow ZGNRs with a width of 1.2, 0.7 and 0.4 nm, respectively. Inset: corresponding FFT pattern.

4.2.4 Different configurations in GNR and simulated TEM images

As mentioned above, we can obtain ultra-narrow GNRs with well define edge structures. However, when applying a high bias voltage to the GNR, the edges of the GNR were curled up and often welded together due to the high temperature. In this case, the folded edge structures will be formed in GNR, as shown in Figure 4.3, 4.6 and 4.7. The driving force of this behavior seems to reduce dangling bonds at the edges of the

GNR. Moreover, SiN membrane which supports the electrode was observed to be stretched due to Joule heating so that the gap distance between source and drain electrode slightly increased. In this case, the GNR must be also stretched, which may promote the formation of wrinkles parallel to the stretching direction. In Figure 4.6 (a) and (b), a single wrinkle was formed near the 1.5 nm wide ribbon, and the direction of wrinkle structure was parallel to the stretching direction.

For confirming the formation of those structures during thinning process, the simulated TEM images of GNRs were carried out by multi-slice calculations (HREM Research). The atomic positions were derived from the configurations of GNRs as obtained from the experimental TEM images. The conditions of the TEM observation were an accelerating voltage of 80 kV, a spherical aberration coefficient of 0.001 mm and a fifth order spherical aberration of 0.001 mm. The simulated TEM images of Figure 4.8 were obtained with different focus values of ±5, ±2 and 0 nm, which reproduced the experimental TEM images. For example, in Figure 4.8, the simulated TEM images based on the wrinkle model (under focus -2 nm) reproduce the experimental TEM image (Figure 4.7(a)). These folding and wrinkle structures were also observed after joule annealing in previous reported papers.[16,17]

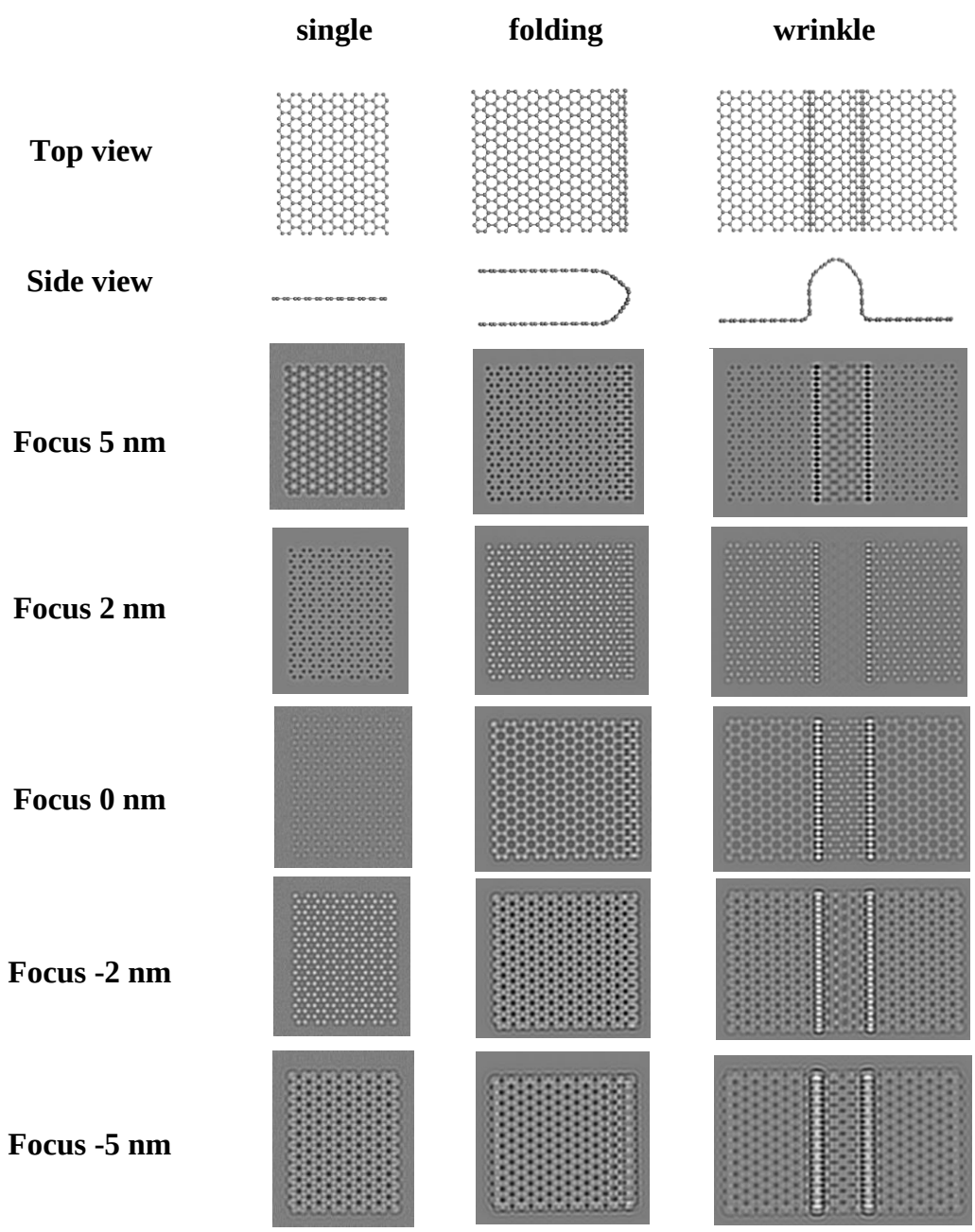

Figure 4.8 Schematic structures and simulated TEM images of single, folding and wrinkle structure under different focus values.

4.3 Resistance measurement of GNR with different widths

By combining the above rough and precise sculpting method, the GNRs could be sculpted from several hundred nanometer to below 10 nm in width. The resistance of GNRs with different widths have been measured during the whole sculpting process. All the resistance values were measured under a fixed bias voltage 1.0 V. Here we show the resistance data for two sample: Sample 1# and Sample 2#. By above sculpting methods, the width of Sample 1# change from 243 to ca. 2 nm, and the width of Sample 2# change from 358 to ca. 3 nm.

In Figure 4.9, we notice that the resistances of these two devices increased with decreasing the GNR widths. The total resistance R_{TOT} of the device depends on the width and can be described by the fitting function of $R_{TOT} = R_C + \rho_G \cdot \frac{L}{w \cdot d}$. Here, R_C is the contact resistance between GNR and Cr/Au electrodes, ρ_G is the resistivity of clean graphene, L and w is the length and width of suspended GNR between electrodes, respectively, d is the thickness of GNR which depend on the layer numbers (0.335 nm single layer thickness[18]). By fitting the experimental resistances as a function of width, we obtained the contact resistance, R_C = 2.8 ±1.4 kΩ and 6.2 ± 0.3 kΩ for Sample 1# and Sample 2#, respectively. The contact resistance seem to be determined dominantly by the resistance of Au electrode and GNR interface, since the resistance of long and narrow Au electrode must be relatively low. By removing the contact resistance from

the total resistance, the calculated resistivity of clean monolayer graphene for Sample 1# and Sample 2# was 1588 and 1572 Ω·nm, respectively. This value match well with previous papers, which shows the range of resistivity values are from 1350 to 1813 Ω·nm.[6,19,20]

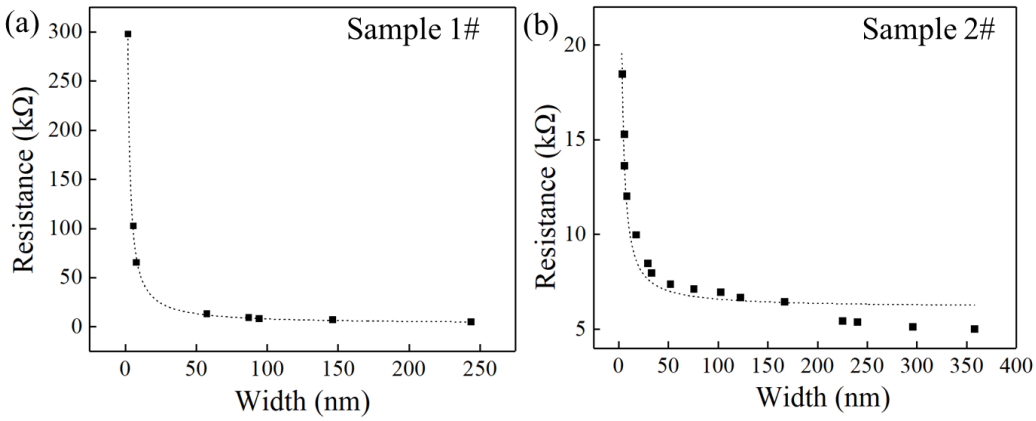

Figure 4.9 Resistance of the suspended graphene as a function of its width. All data were measured under bias voltage equal to 1.0 V. (a) Sample 1# with the width from 243 to 2 nm. The fitting contact resistance R_c= 2.8±1.4 kΩ. (b) Sample 2# with the width from 358 to 3 nm. The fitting contact resistance R_c= 6.2± 0.3 kΩ.

4.4 Structure-dependent electronic properties of ultra-narrow AGNR and ZGNR

4.4.1 The electrical conductance properties of AGNRs

As shown in Figure 4.10 (a) and (b), ultra-narrow GNRs with width of 1.5 nm

fabricated by convergent electron beam nano-sculpting followed by annealing with a high bias voltage. The edge structure of armchair (AGNR) was formed as indicated by black hexagonal patterns in Figure 4.10 (b). It is identified by the relationship between the orientation of the edge and the position of six spots in the corresponding FFT pattern.

During the thinning process, the I-V measurements were performed at some points by sweeping the bias voltage in the range of -1.0 to 0.0 V at 50 mV/step. The measured I-V curves before and after sculpting were shown in Figure 4.10 (c) and (d), respectively. Interestingly, we found that the electrical property of the GNR changed from almost metallic property to semiconductive one, when the width changed from 243 to 1.5 nm. As mentioned in Chapter 4.2.2, the transport gap can be estimated by one half of the observed nonlinear region. The AGNR of Figure 4.10 (d) has strong nonlinear I-V characteristic at finite bias voltage (-0.3 ~ 0.3 V), showing the nonlinear region of ~600 meV. Therefore, the AGNR of 1.5 nm width is found to have an estimated transport gap of ~300 meV.

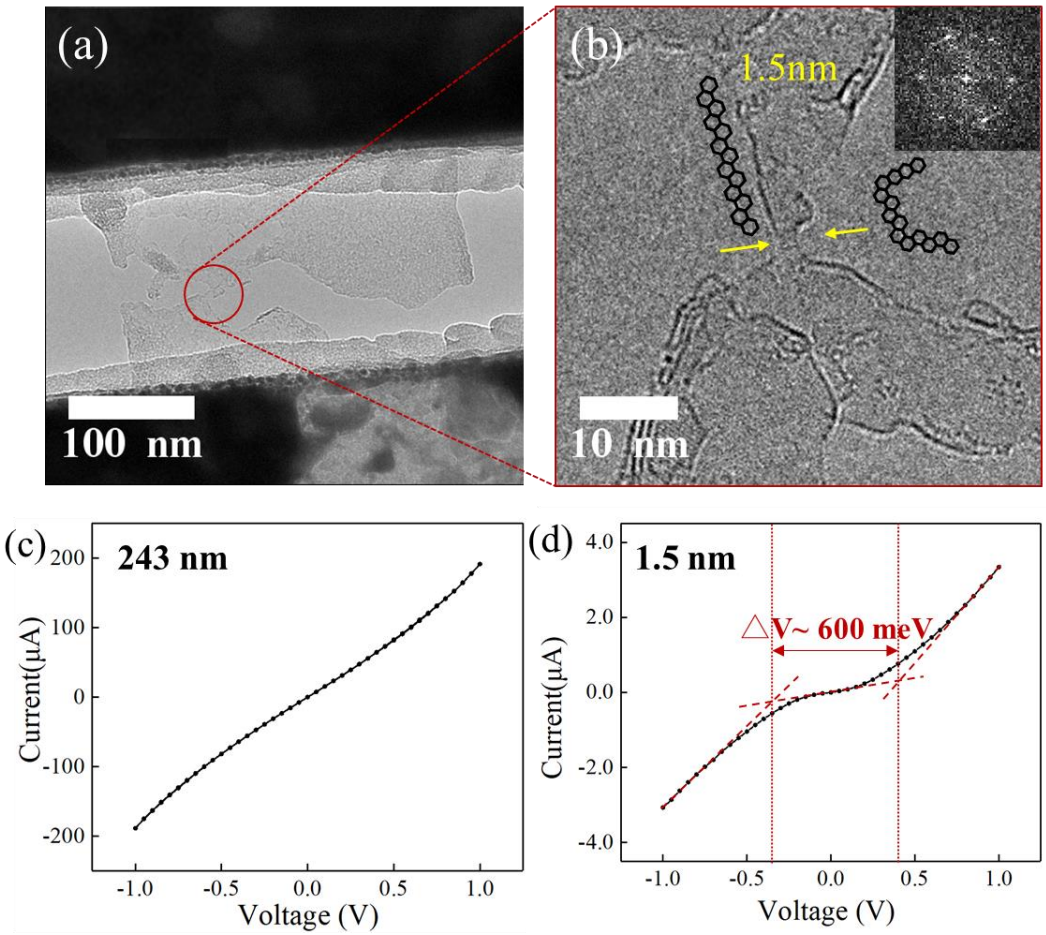

Figure 4.10 The TEM images of ultra-narrow 1.5 nm wide AGNR and I-V curves. (a) The low magnification of GNR after sculpting. From the enlarged TEM image (b), the width of ribbon is ca. 1.5 nm. The red arrow indicate the edge of ribbon. (c) The corresponding I-V curve of initial 243 nm wide GNR in Figure 4.3 (a). (d) The corresponding I-V curve of 1.5 nm wide GNR in (b).

4.4.2 I-V curves for ultra-narrow ZGNRs

As mentioned in Chapter 4.2.3, ZGNR with a width of 1.5 nm has been formed (Figure 4.6 (a,b)). The I-V curve was measured simultaneously with TEM observation.

Figures 4.11 (a) and (b) show the I-V and dI/dV-V curves for this ZGNR. The folding and wrinkled structures are not considered to have an influence on the electrical transport properties. We found that the differential conductance, dI/dV, sharply increased at the threshold voltage, which corresponded to -0.75 and 0.65 V. The transport gap can be estimated to be 0.7 V. However, to the best of our knowledge, such a large energy gap and also sharp increase in the dI/dV-V curve has not been reported previously. Sharp increases in the dI/dV-V curve were also observed for ZGNRs with widths of 1.7 and 1.2 nm, as shown in Figure 4.4 (l) and Figure 4.11 (d). And, the nonlinear regions (△V) for ZGNRs of 1.7 and 1.2 nm widths were measured to be 1.1 and 1.9 V, respectively. The transport gap for ZGNRs of 1.7 and 1.2 nm widths can be estimated to be 0.56 and 0.93 V, respectively. Therefore, the transport gap has a tendency to increase with decreasing the width of ZGNR as shown in Figure 4.12.

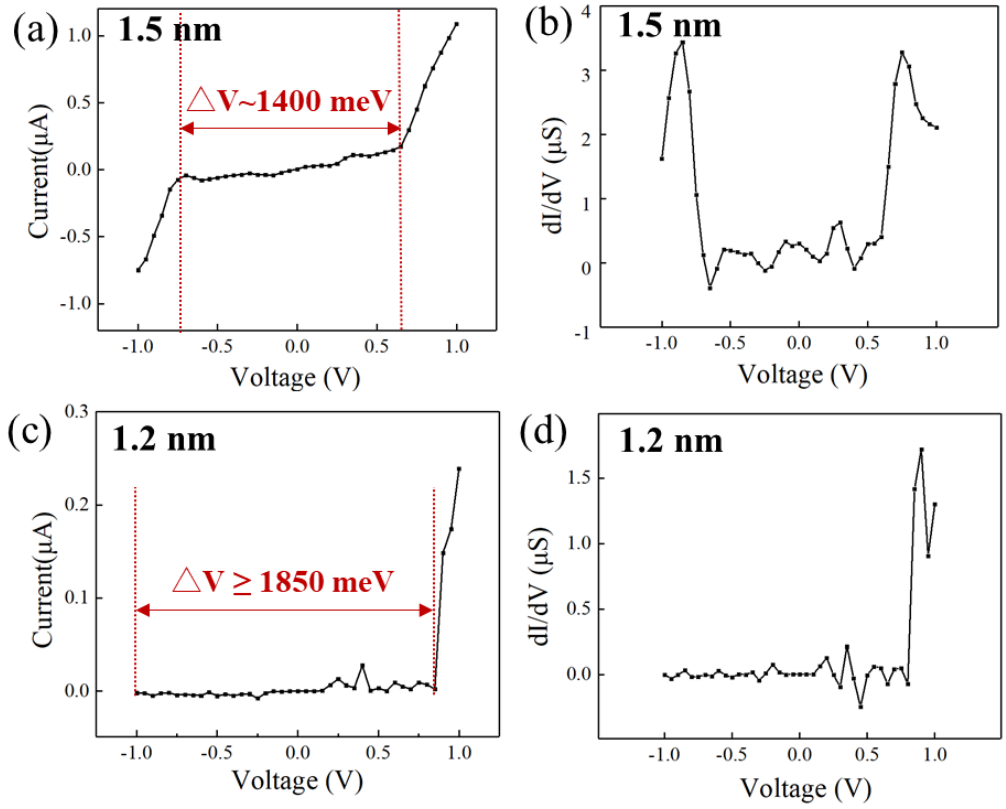

Figure 4.11 I-V and dI/dV-V curves for ultra-narrow ZGNRs. (a,b) The corresponding I-V and dI/dV-V curves for a 1.5 nm wide ZGNR, as shown in Figure 4.6 (b). (c,d) The corresponding I-V and dI/dV-V curves for a 1.2 nm wide ZGNR, as shown in Figure 4.7 (a). The abrupt increase of current is observed at 0.85 V, although it is not observed at the negative bias voltage in the range of -1 V to1 V. This reason may be out of range. Because the calculated band gap of 1.2 nm wide ZGNR should be around 1.4 V from GW calculation,[17] which means that ΔV in I-V curve should be about 2.8 V, which is much larger than the measured I-V range.

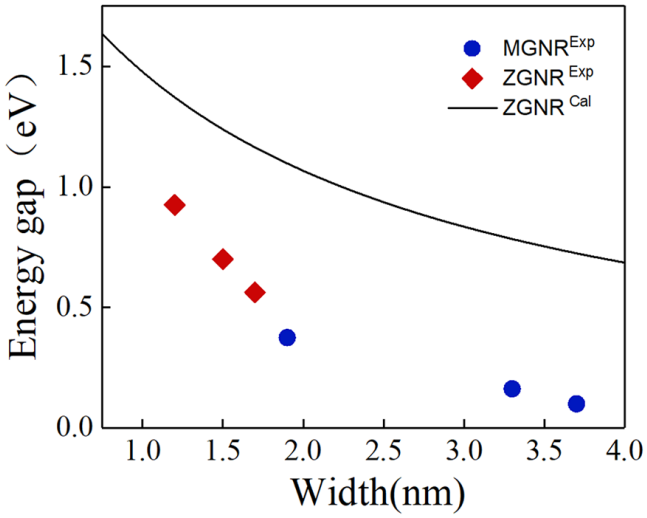

Figure 4.12 Measured and calculated energy gaps for GNRs with different widths during the thinning process. The blue circle and red diamond indicate the experimentally measured energy gaps of MGNRs and ZGNRs, respectively. The solid black line indicates the energy gaps calculated using the GW approximation.[21]

4.4.3 Interpretation of I-V curves for ZGNRs

The dimensions of narrow GNRs measured from TEM images and the energy gap determined from the I-V curves are summarized in Table 4.1. We find that the energy gap has a correlation with the width rather than the length. Also, the dI/dV-V curves show different features between MGNRs and ZGNRs; the ZGNRs show not only larger energy gaps than the MGNRs, but also a sharp increase at the threshold voltage in the dI/dV-V curve.

Table 4.1 Comparison of the electrical conductance properties with different ribbon structures

Edge structure	W (nm)	L (nm)	R (nm)	V_t^{exp} (V)	E_{gap}^{exp} (eV)	E_{gap}^{GW} (eV)
MGNR	3.7	0.7	1.1	-	0.10	-
MGNR	3.3	0.9	1.5	-	0.16	-
MGNR		0.5	0.7	-	0.38	-
ZGNR	1.7	0.3	1.1	0.60	0.56*	1.16
ZGNR	1.5	1.4	1.6	0.65	0.70*	1.24
ZGNR	1.2		2.0	0.85	≥ 0.93*	1.37

The width (W), left (L) and right (R) side lengths of a suspended GNR. The threshold voltage (V_t^{exp}) is the point where the current abruptly increases in the I-V curve. The energy gap (E_{gap}^{exp}) is estimated to be one half of the nonlinear region △V in the I-V curve. Note that the gap with the asterisk * indicates an apparent value. The band gap (E_{gap}^{GW}) was calculated based on GW approximation.[21]

The electronic structure of GNRs has been investigated using several theoretical calculations, including tight-binding (TB) approximations,[21-23] GW approximation,[17,24,25] density functional theory (DFT),[26,27] and nonequilibrium calculations.[26,28] Yang et al.[17] adopted the GW approximation, which includes electron-electron interaction effects due to the confinement, to show that the energy gap becomes 0.5 to 3.0 eV for both AGNRs and ZGNRs with widths of 2.4-0.4 nm. These energy gaps which calculated by this method could better predicted the experimental

results.[23,29] In calculation, the energy gap for ZGNR with width less than 2 nm was predicted to be greater than 1 eV. However, in our experiment, the energy gaps for ZGNRs with widths of 1.7, 1.5, and 1.2 nm were estimated to be 0.56, 0.7, and 0.93 eV, respectively. Obviously, the measured energy gap is smaller than the calculated one.

I-V curves of GNRs have rarely been investigated theoretically due to the difficulty of the nonequilibrium calculation. The I-V curve of GNRs was investigated based on nonequilibrium calculations by Areshkin and Nikolić.[28] They expected that the tunneling current would pass through the ZGNR when a bias voltage was applied, and that it would collapse the spin polarization and cause the ZGNR to change to the metallic state when such a current exceeded the threshold. They also predicted an abrupt jump in the I-V curve for two-terminal devices with short ZGNR due to a current-driven magnetic-insulator and nonmagnetic-metal nonequilibrium phase transition. The experimental results, which were obtained for narrow and short ZGNRs, seem to fit well with this prediction.

Firstly, a sharp increase in the dI/dV-V curve was observed only for ZGNRs as shown in Figure 4.4 (l), Figure 4.11 (b) and (d). Such a sharp increase in the dI/dV-V curve was not observed for the MGNRs (Figure 4.4) or AGNRs (Figure 4.10). Taking into account that the I-V curves of the GNRs were measured under high temperature conditions, the electronic states around the Fermi level must be blurred to some extent,

which would at least slow down the change in the I-V curve. Despite the high temperature conditions, a sharp increase in the dI/dV-V curve occurred, which cannot be explained by a band structure that assumes an equilibrium condition.

Secondly, the measured energy gap for the ZGNR was smaller than the calculated one based on the GW approximation.[21] The measured gaps for ZGNRs with widths of 1.7, 1.5, and 1.2 nm were 0.56, 0.7, and 0.93 eV, respectively, as shown in Figure 4.13. The band gaps for the ZGNRs with widths of 1.7, 1.5, and 1.2 nm were calculated to be 1.16, 1.24, and 1.37 eV, respectively.[17] When the applied bias voltage reaches the threshold value, the tunneling current passing through the ZGNR may be sufficient to collapse the spin polarization, resulting in a sharp increase in the dI/dV-V curve. If the threshold voltage is larger than the band gap, then the dI/dV-V curve shows a gradual increase, as illustrated in Figure 4.4 (i-k). Therefore, the threshold voltage should be smaller than the band gap of the ZGNRs because of a sharp increase in the dI/dV-V curve. Table 4.1 shows that the measured threshold voltage for the narrow ZGNRs was smaller than the calculated band gap.

Thirdly, the threshold voltage for the abrupt jump in the I-V curve increased with the ZGNR length. The tunneling current passing through the ZGNR can be predicted to increase with a decrease in the length; i.e., the threshold voltage should decrease with the length. The threshold voltages for average lengths of 0.7, 1.5, and 1.95 nm were

measured to be 0.6, 0.65, and 0.85 V, respectively (Table 4.1). Therefore, the present results support magnetic-insulator and nonmagnetic-metal transitions in ZGNRs.

I-V curves of narrow and short GNRs were measured during in situ TEM observations, whereby the I-V curves of the ZGNRs were deemed to be different from those of the MGNRs. The I-V curves measured for the ZGNRs support the occurrence of magnetic-insulator and nonmagnetic-metal nonequilibrium transitions, which was previously reported.[28] Therefore, it is possible to collapse the spin polarization in narrow and short ZGNRs by application of a certain bias voltage. Narrow and short ZGNRs are thus good candidates for the fabrication of single nanosized switching devices.

4.5 Conclusion

In this chapter, we introduced the nano-sculpting method for GNR, such as rough nano-sculpting and precise thinning process. Rough nano-sculpting is usually used for narrowing the width from several hundred nanometer to ca.20-30 nm by converged electron beam. Following the rough nano-sculpting, the precise narrowing method can obtain sub-10 nm GNR with the application of high bias voltage. It means the fabrication of narrow GNRs could be controlled by convergent electron beam nanosculpting followed by high bias voltage annealing.

By the combination of these two methods, we investigated structure-dependent electronic properties of suspended GNRs by in situ TEM observation to obtain structural information and simultaneous current-voltage curve measurements. During the GNR thinning process, we found that the electrical conductance of the GNR changed from metallic to semiconducting behavior with decreasing the width. When the width of GNR became very narrow (usually < 4 nm), the transport gap started to be opened. A transport gap of 300 and 700 meV is estimated for 1.5 nm wide AGNR and ZGNR, respectively.

The I-V curves for the ZGNRs were obviously different from those for the MGNRs and AGNRs as follows. (1) A sharp increase in the differential conductance-voltage (dI/dV-V) curve was observed only for ZGNRs. (2) The gaps measured for ZGNRs were smaller than the band gaps calculated by the GW approximation. (3) The threshold voltage of the abrupt jump in the I-V curve decreased with the ZGNR length. These features support the occurrence of current-driven magnetic-insulator and nonmagnetic-metal nonequilibrium phase transitions by application of a bias voltage, as previously reported. Narrow and short ZGNR are thus good candidates for the fabrication of single nanosized switching devices.

References

[1]. Fischbein, M.D.; Drndić, M.; Electron beam nanosculpting of suspended

graphene sheets. *Applied Physics Letters* 2008, 93 (11), 113107.

[2]. Song, B.; Schneider, G.F.; Xu, Q.; Pandraud, G.; Dekker, C.; Zandbergen, H., Atomic-scale electron-beam sculpting of near-defect-free graphene nanostructures. *Nano Letters* 2011, 11 (6), 2247–2250.

[3]. Krasheninnikov, A.V.; Banhart, F., Engineering of nanostructured carbon materials with electron or ion beams. *Nature Materials* 2007, 6 (10), 723–733.

[4]. Huang, J.Y.; Chen, S.; Ren, Z.F.; Chen, G.; Dresselhaus, M.S., Real-time observation of tubule formation from amorphous carbon nanowires under high-bias joule heating. *Nano Letters* 2006, 6 (8), 1699–1705.

[5]. Meyer, J. C.; Eder, F.; Kurasch, S.; Skakalova, V.; Kotakoski, J.; Park, H. J., et al., Accurate measurement of electron beam induced displacement cross sections for single-layer graphene. *Physics Review Letters* 2012, 108 (19), 196102.

[6]. Wang, Q.; Kitaura, R.; Suzuki, S.; Miyauchi, Y.; Matsuda, K.; Yamamoto, Y., et al., Fabrication and in situ transmission electron microscope characterization of free-standing graphene nanoribbon devices. *ACS Nano* 2016, 10 (1) 1475–1480.

[7]. Huang, J.Y.; Ding, F.; Yakobson, B.I.; Lu, P.; Qi, L.; Li, J., In situ observation of graphene sublimation and multi-layer edge reconstructions. *Proceedings of the National Academy of Sciences* 2009, 106 (25), 10103–10108.

[8]. Jia, X.; Hofmann, M.; Meunier, V.; Sumpter, B.G.; Campos-Delgado, J.; Romo-Herrera, J.M., et al., Controlled formation of sharp zigzag and armchair edges in graphitic nanoribbons. *Science* 2009, 323 (5922), 1701–1705.

[9]. Deng, S.; Berry, V., Wrinkled, rippled and crumpled graphene: an overview of formation mechanism, electronic properties, and applications. *Materials Today* 2016, 19 (4), 197–212.

[10]. Han, M.Y.; Özyilmaz, B.; Zhang, Y.; Kim, P., Energy band-gap engineering of graphene nanoribbons. *Physical Review Letters* 2007, 98 (20), 206805.

[11]. Han, M.Y.; Brant, J.C.; Kim, P., Electron transport in disordered graphene nanoribbons. *Physical Review Letters 2010*, 104 (5), 056801.

[12]. Gallagher, P.; Todd, K.; Goldhaber-Gordon, D., Disorder-induced gap behavior in graphene nanoribbons. *Physics Review B* 2010, 81 (11), 115409.

[13]. Lin, M.-W.; Ling, C.; Agapito, L.A.; Kioussis, N.; Zhang, Y.; Cheng, M.M.-C., et al., Approaching the intrinsic band gap in suspended high-mobility graphene nanoribbons. *Physics Review B* 2011, 84 (12), 125411.

[14]. Son, Y.-W.; Cohen, M.L.; Louie, S.G., Energy gaps in graphene nanoribbons. *Physical Review Letters* 2006, 97 (21), 216803.

[15]. Miyake, T.; Saito, S., Quasiparticle band structure of carbon nanotubes. *Physics Review B* 2003, 68 (15), 155424.

[16]. Bao, W.; Miao, F.; Chen, Z.; Zhang, H.; Jang, W.; Dames, C., et al. Controlled ripple texturing of suspended graphene and ultrathin graphite membranes. *Nature Nanotechnology* 2009, 4 (9), 562–566.

[17]. Yang, L.; Park, C.-H.; Son, Y.-W.; Cohen, M.L.; Louie, S.G., Quasiparticle energies and band gaps in graphene nanoribbons. *Physical Review Letters* 2007, 99 (18), 186801.

[18] Huang, Y.; Wu, J.; Hwang, K. C., Thickness of graphene and single-wall carbon nanotubes. *Physical review B* 2006, 74(24), 245413.

[19]. Lu, Y.; Merchant, C. A.; Drndic, M.; Johnson, A. T., In situ electronic characterization of graphene nanoconstrictions fabricated in a transmission electron microscope. *Nano Letters* 2011, 11 (12), 5184–5188.

[20]. Qi, Z. J.; Rodriguez-Manzo, J. A.; Botello-Mendez, A. R.; Hong, S. J.; Stach, E. A.; Park, Y. W., et al., Correlating atomic structure and transport in suspended graphene nanoribbons. *Nano Letters* 2014, 14 (8), 4238–4244.

[21]. Ezawa, M., Peculiar width dependence of the electronic properties of carbon nanoribbons. *Physics Review B* 2006, 73 (4), 045432.

[22]. Abanin, D.A.; Lee, P.A.; Levitov, L.S., Spin-filtered edge states and quantum hall effect in graphene. *Physical Review Letters* 2006, 96 (17), 176803.

[23]. Son, Y.-W.; Cohen, M.L.; Louie, S.G., Half-metallic graphene nanoribbons.

Nature 2006, 444 (7117), 347–349.

[24]. Hybertsen, M.S.; Louie, S.G., Electron correlation in semiconductors and insulators: Band gaps and quasiparticle energies, *Physics Review B* 1986, 34 (8), 5390–5413.

[25]. Spataru, C.D.; Ismail-Beigi, S.; Benedict, L.X.; Louie, S.G., Excitonic effects and optical spectra of single-walled carbon nanotubes. *Physical Review Letters* 2004, 92 (2004) 077402.

[26]. Onoda, S.; Sugimoto, N.; Nagaosa, N., Quantum transport theory of anomalous electric, thermoelectric, and thermal Hall effects in ferromagnets. *Physics Review B* 2008, 77 (16), 165103.

[27]. Pisani, L.; Chan, J.A.; Montanari, B.; Harrison, N.M., Electronic structure and magnetic properties of graphitic ribbons. *Physics Review B* 2007, 75 (6), 064418.

[28]. Areshkin, D.A.; Nikolić, B.K., I − V curve signatures of nonequilibrium-driven band gap collapse in magnetically ordered zigzag graphene nanoribbon two-terminal devices. *Physical Review B* 2009, 79 (20), 205430.

[29]. Park, C.-H.; Spataru, C.D.; Louie, S.G., Excitons and many-electron effects in the optical response of single-walled boron nitride nanotubes. *Physical Review Letters* 2006, 96 (12), 126105.

Chapter 5 Restructure of graphene nanoribbon under bias voltage

Introduction

This chapter contains the effect of applied bias voltage on monolayer and few layer GNRs such as the restructure of ribbon edge, the sublimation of layer, the reduction of width and the improvement of electrical conductance.

In Chapter 5.1, we show the edge recrystallization of monolayer GNR under the constant bias voltage. In Chapter 5.2, we show the improvement of electrical conductance for monolayer GNR by increasing the bias voltage. In Chapter 5.3, we introduce the layer sublimation and reorganization of few layer GNR by increasing the bias voltage.

5.1 Edge recrystallization of monolayer GNR

It is well known that the rough edges of GNR device lead to carrier scattering, which affects the properties of devices. In this sense, the atomically smooth edges are essential for applications. However, it is difficult to realize it by traditional methods (EBL, FIB, chemical methods and so on).

Here the edge recrystallization is realized by applying a fixed bias voltage of 1.0 V across the ribbon, which result in high local temperature on the ribbon. After rough nano-sculpting, the graphene ribbon of 6.6 nm width had rough edges and a “graphene island” was formed near the left edge as shown in Figure 5.1 (a). By the corresponding FFT pattern, this ribbon was confirmed to be monolayer. The formation of “graphene island” may be caused by the graphitization of amorphous carbon on the surface of GNR during current annealing.[1,2] In the HR-TEM, the left-side edge was observed to be higher contrast than the right-side one, suggesting that the left-side edge was curled or folded after sculpting. Such curl or fold often happened for suspended ribbon by current annealing, as we discussed in Chapter 4.2.4. Fortunately, the right side edge is flat and suspended, which shows very low contrast. Here, we focus on the change of the right side edge structure when holding the bias voltage. The whole process spent 40 min and the duration under the applied constant bias voltage of 1.0 V is shown at the upper right corner in Figure 5.1 (b-d). We found that the edge structure changed from

rough, to mixing of zigzag and armchair and to armchair only as indicated by color lines in Figure 5.1. During all this process, the width of ribbon almost remained unchanged.

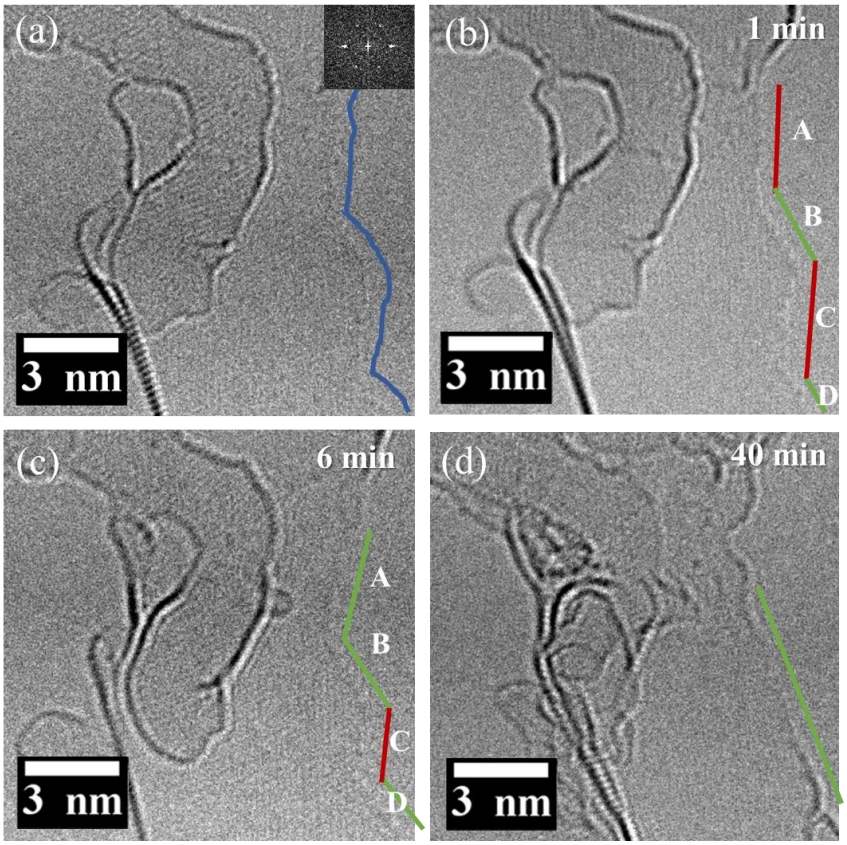

Figure 5.1 Edge recrystallization of monolayer GNR under 1.0 V bias voltage. (a) TEM image of initial GNR with a rough edge (right side) and corresponding FFT pattern obtained near the right edge as insert. (b-d) The TEM images after applying bias voltage for 1, 6 and 40 min, respectively. The colorful lines near the ribbon indicate the different edge structure. Blue, green, and red line indicate rough, armchair and zigzag edge structure, respectively. The edge orientation is identified by the combination of ribbon

direction and corresponding FFT pattern.

In detail, the right edge was initially rough as shown in Figure 5.1 (a). The edge structure changed to mixing of armchair and zigzag edges after only 1 min. In Figure 5.1 (b), the edge structure of right side was observed to separate into four sections, which indicated by different color lines with section A-D. Section A and C shows zigzag edge and section B and D, armchair edge. The preferred edge reconstruction indicate the activation energy of forming zigzag or armchair edges is lower than other structure. After 6 min, section B-D kept the same edge structure, only section A changed from zigzag to armchair edge structure. It should be noticed that, although the zigzag edge direction of section C unchanged, the length reduced from 3.5 to 2.6 nm. It seems the armchair structure is more stable than the zigzag one under 80 kV electron beam radiation, which is in agreement with the previous prediction by density functional tight binding calculation.[3] Then, we kept holding the bias voltages at 1.0 V, after 40 min, the edge all changed to armchair direction, as shown in Figure 5.1 (d). The maximum length of this armchair configuration is ca. 7 nm.

Such reconstruction for the nanoribbons and edges may be contribute to carbon atom vaporization and/or high temperature induced by applied bias voltage.[4] When the current flows along the ribbon with rough edge as shown in Figure 5.1(a), we think that

the rough edge have high temperature locally due to high resistance caused by carrier scattering at the rough edge. It may promote vaporizing the edge atoms or rearrangement of the edge atoms to form zigzag or armchair edges. Also, in Figure 5.2, although the voltage was constant at 1.0 V during this process, the current gradually increased after 20 min. It suggests that the resistance of the graphene ribbon may be reduced by formation of smooth edge. However, as shown in Figure 5.1, the size of ribbon almost unchanged before and after applied the bias voltage, suggesting that the effect of carbon atom vaporization is limited. Therefore, we think that the edge structure change from roughness to smooth by rearrangement of the edge atoms due to the application of a low constant bias voltage. Such smooth edge results in improvement of the electrical conductance property of the graphene nanoribbon.

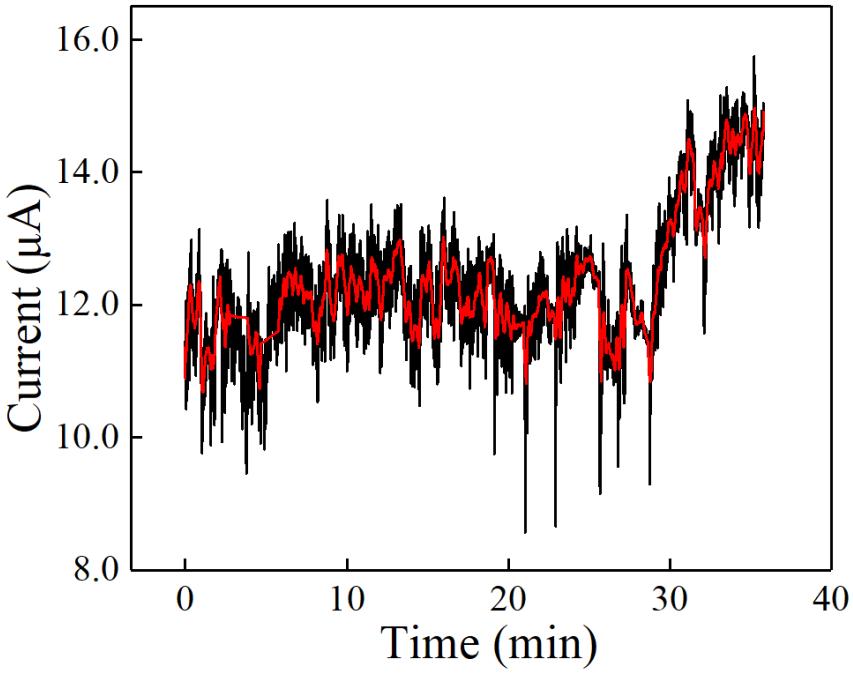

Figure 5.2 The time evolution of current during edge recrystallization. The red line indicated the average value of current without noise.

For investigating the mechanism of edge reconstruction from zigzag to armchair, we analyzed the HR-TEM images taken during this process. Figure 5.3 shows the process that the section A changed from zigzag to armchair edge structure (Figure 5.1 (b) to (c)). The whole process lasted for 5 min. Due to the vibration of suspended GNR during heating, we did not obtain clear atomic TEM images. In Figure 5.3 (b-e), We found that many black dots were shown at the edge of the ribbon as indicated by orange arrows. In a series of the TEM images, the black dots not only changed the positions but also the intensities. Initially, most of them appeared at the zigzag edges (section A

and C), but, after 2 min, they almost moved to the armchair edge (section B). These movable black dots were thought to correspond to migrating carbon atoms. Energetically, the edges of the ribbon must be favorable adsorption sites for such isolated carbon atoms. Interestingly, by comparing between Figure 5.3 (a) and (f), we found that the edge lengths of section B and C changed, although the orientation was the same. The length of section B increased from 1.9 to 2.6 nm, while the length of section C decreased from 3.5 to 2.6 nm. This phenomena could be explained by migrating carbon atoms.

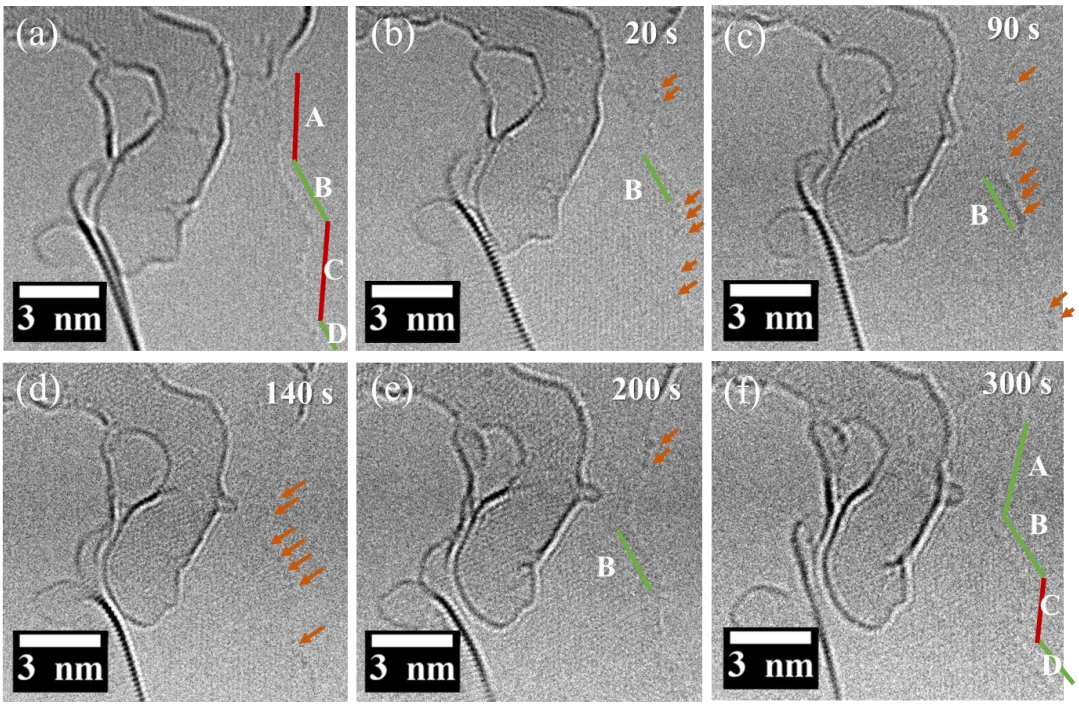

Figure 5.3 Edge restructure from zigzag to armchair edges. From TEM images (a) to (f), the applied bias voltage was fixed at 1.0 V. The orange arrow indicated some black dots formed at the edge of ribbon during this process. Green and red line indicate

armchair and zigzag edge structure, respectively.

5.2 Improvement of conductance for monolayer GNR during reconstruction

For investigating the effect of reconstruction on the transport property of GNR, we varied the bias voltage of a monolayer GNR device.

As shown in Figure 5.4 (a), we started from an initial 6.6 nm wide monolayer GNR. The layer number was identified by FFT pattern from the base part supporting the GNR (red dashed square). The base part was monolayer with some "graphene islands" on the surface, which often formed after current annealing. During the experiment, we gradually increased the bias voltage from 1.0 V to higher values and kept it for 5-10 min; after the edge of ribbon didn't further change, the bias reduced back to 1.0 V and corresponding resistance was measured. During this process, the variation of width and edge structure was observed for the monolayer GNR, this phenomena was also observed for few layer GNR, which will be discussed in Chapter 5.3. In Figure 5.4 (a-e), the width was reduced from 6.1 to 2.2 nm. The narrowest width of monolayer GNR was 2.2 nm, when the bias voltage was 2.2 V. Finally, this GNR was broke at the middle as shown in Figure 5.4 (f), when the bias voltage increased from 2.2 V. In this process, except for variation for the edge structure of GNR, we found the variation of the width. Some "graphene islands" adsorbed on the surface of the base part disappeared, which

may be occurred by evaporation. The width of the narrowest GNR obviously decreased from 6.6 to 2.2 nm as shown in Figure 5.4 (a)-(e). Comparing with the results of Chapter 5.1, which was obtained by the condition under a fix bias voltage 1.0 V, increasing the bias voltage affect not only the edge structure of the GNR but also the width of the narrowest GNR.

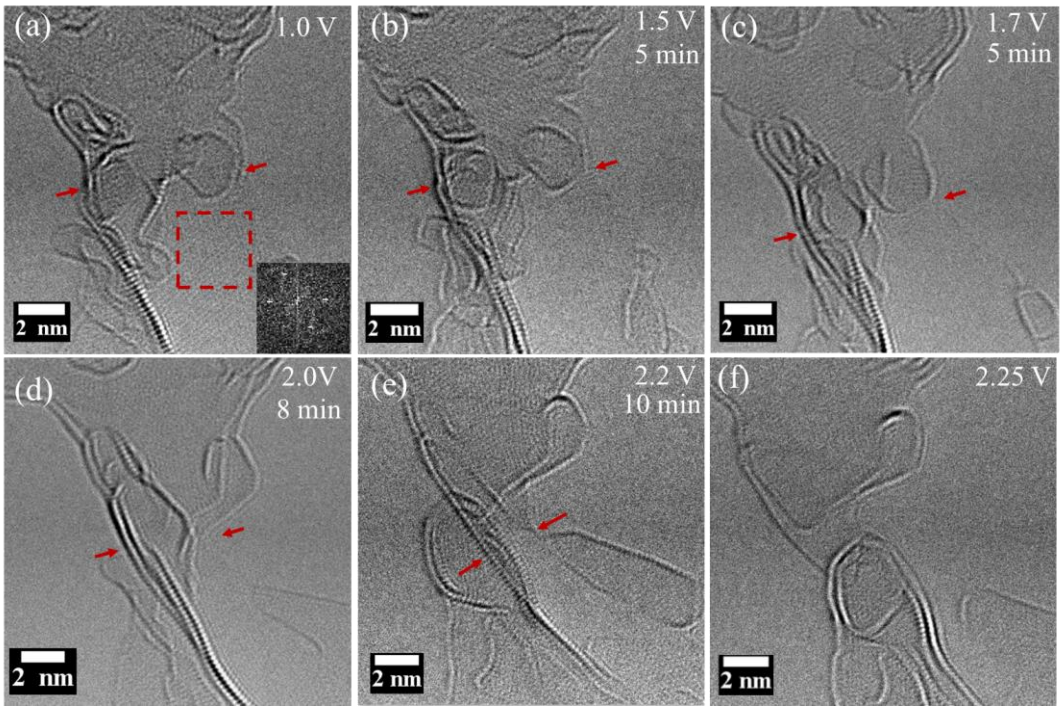

Figure 5.4 Voltage induced thinning process of monolayer GNR device. (a-f) TEM images of monolayer GNR under different bias voltage. The corresponding FFT pattern at the lower right corner from the red dashed square in (a). The narrowest width are indicated by red arrow. The applied voltage and keeping time is shown at upper right corner.

The conductance and current density of ribbon was measured during this process, as shown in Figure 5.5. For avoiding the effect of increasing the bias voltage, all resistance with different width of the graphene ribbon were measured when the bias voltage was set back to 1.0 V. We found that both conductance and current density increased with increasing the width from 6.6 to 3.3 nm (Figure 5.4 (a-d)), which corresponded to the edge recrystallization process of GNR. After that, when the width of GNR reduced from 3.3 to 2.2 nm, the current density kept increased, however, the conductance value decreased a little. It may attribute to the sublimation of "graphene islands" which cover the narrowest GNR. During the whole process, although almost 3 times reduction in the width of the graphene ribbon, the final conductance was 1.4 times larger than the initial one. In addition, when the width of the monolayer GNR reduced to 2.2 nm, it showed a maximum current density is $2.66 \times 10^{13} A/m^2$. That's to say, the structure recrystallization lead to the increase in the conductance of the GNR, even when the width reduced. It can be contribute to the recrystallization which reduced carrier scattering and improved transport.

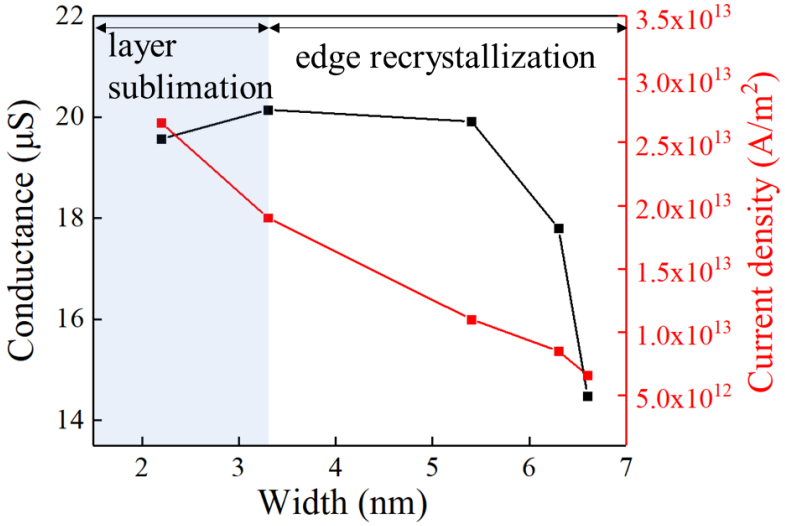

Figure 5.5 Measured conductance (black squares) and current density (red squares) as a function of width for monolayer GNRs under increased bias voltage.

5.3 Layer sublimation and reorganization of few layer GNR

The layer sublimation and recrystallization process of few layer GNR device was investigated by increasing the bias voltage from 1.0 to 2.6 V (200-500 mV/step). Figure 5.6 shows the change of few layer GNR with increasing the bias voltage. In Figure 5.6 (a), this ribbon consisted of few layer graphene with different orientation. When the bias voltage increased to 2.0 V, the reconstruction was firstly observed along the GNR boundary. The restructure of the edge was due to larger electrical resistance in the edge junction, which has discussed in Chapter 5.1. When the voltage reached to 2.4 V, the number of graphene layers reduced obviously, only bilayer GNR left with some separated “graphene islands”. Finally, when the voltage was increased to 2.6 V, the

ribbon suddenly broke at the middle as shown in Figure 5.6 (f).

With increasing the voltage from 1.0 to 2.4 V, we found that both width and thickness reduced. At the beginning, as the current passed through the ribbon, the edge structure changed due to high temperature under applying high bias voltage. Then the thickness of the GNR decreased with the width reduced from 8 to 1.6 nm at the same time. This tendency also can identify through the change of corresponding FFT pattern. Finally, all the graphene layers sublimate and the sample broke at the middle.

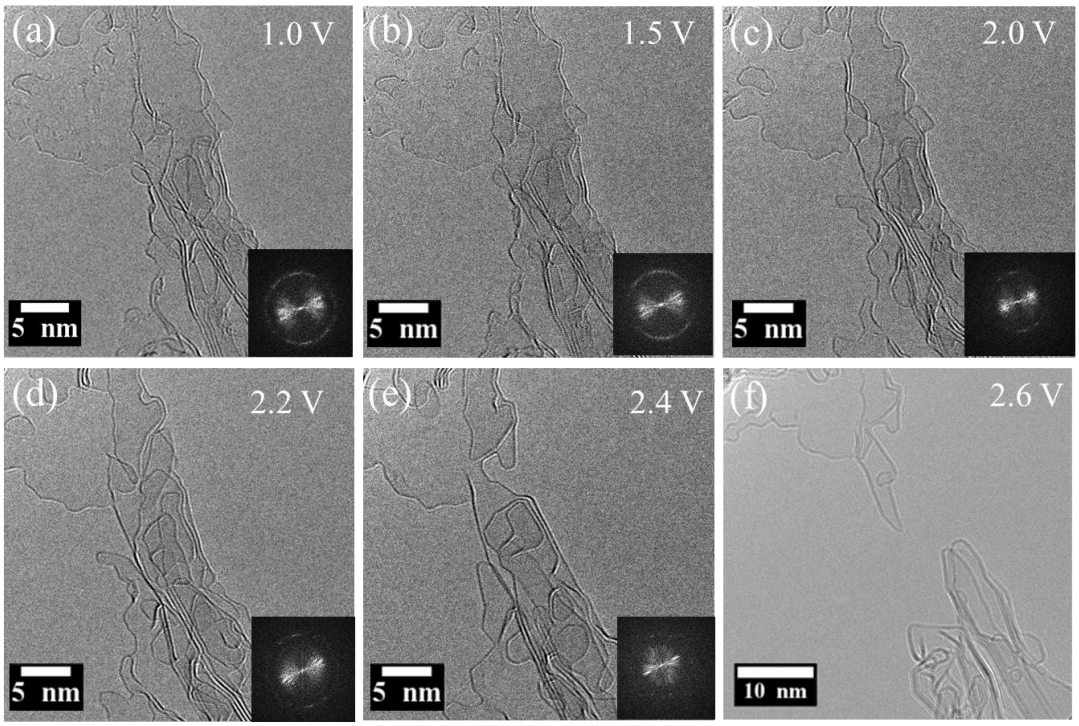

Figure 5.6 Current induced layer sublimation and recrystallization process in few layer GNR device. (a-f) TEM images of few layer GNR under different bias voltage. The applied voltage is shown at upper right corner. The lower right corner shows the

corresponding FFT pattern.

The time evolution of resistance and power are shown in Figure 5.7. The resistance decreased in steps and final reduced to ca. 22 kΩ during the reconstruction process. After the ribbon reduced to 1.6 nm wide bilayer GNR as shown in Figure 5.6 (e), the layer number didn't reduce even when increasing the bias voltage. When the bias voltage reached to 2.6 V, the sample broke down. It indicated that when the layer number of initial few layer GNR reduced to bonded bilayer, it is energetically more favorable to adjust the edges of the ribbon rather than to sublimate the bonded bilayer edge to form a single layer graphene edge.[6,7] This means that the layer sublimation process stops when the graphene is bilayer, and it cannot be used to create single layer graphene ribbons. The power was defined as $P = I^2R$, reached to the maximum value of 140 μW just before breakdown. This value will lead to a high temperature as reported in previous paper.[6,8] At the bilayer GNR's narrowest width of 1.6 nm, the maximum current density is 9.2×10^{13} A/m^2. The improved conductance is contribute to reduce scattering edges during the reorganization of GNR, which has discussed in Chapter 5.2.

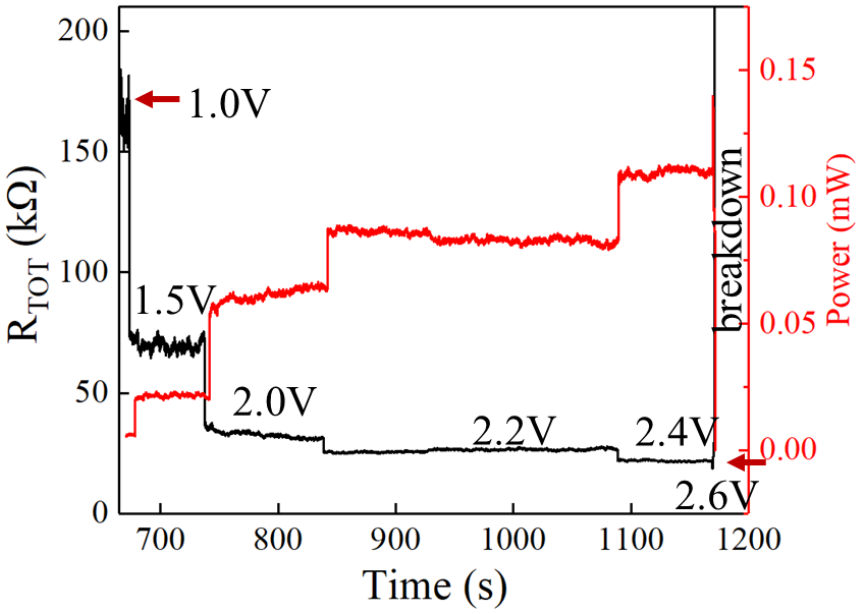

Figure 5.7 Time evolution of GNR device resistance and power during progressively higher bias voltage until device breakdown.

5.4 Conclusion

In this chapter, we investigated the effect of applying bias voltage on monolayer and few layer GNR devices. When we fixed the bias voltage at 1.0 V for a monolayer GNR, the voltage mainly influence the edge structure of ribbon. We observed that a rough edge reconstructed into several straight edges and finally changed to a uniform armchair edge without changing the width. It suggests the possibility to control edge type and improve edge sharpness by applying a fixed bias voltage.

Then, we investigated the effect of increasing the bias voltage on monolayer or few layer GNR. As the increase of voltage, we found that it affect not only the edge structure,

but also the width and layer number of ribbon. Under a high bias voltage, the thickness and width of ribbon shrinks sharply at the same time with the edge restructure. In addition, we measured the conductance and current density of monolayer GNR during such reconstruction process. We found the conductance progressively increased even though the width of ribbon reduced. This results suggest the improvement of conductance could be realize through structure recrystallization under high bias voltage.

All above results provide a method for the fabrication of high-conducting GNR devices by controlling the width, layer number and edge structure.

References

[1]. Westenfelder, B.; Meyer, J. C.; Biskupek, J.; Kurasch, S.; Scholz, F.; Krill III, C. E., et al., Transformations of carbon adsorbates on graphene substrates under extreme heat. *Nano letters* 2011, 11(12), 5123–5127.

[2]. Barreiro, A.; Börrnert, F.; Avdoshenko, S. M.; Rellinghaus, B.; Cuniberti, G.; Rümmeli, M. H., et al., Understanding the catalyst-free transformation of amorphous carbon into graphene by current-induced annealing. *Scientific reports* 2013, 3(1), 1–6.

[3]. Kotakoski, J.; Santos-Cottin, D.; Krasheninnikov, A. V., Stability of graphene edges under electron beam: equilibrium energetics versus dynamic effects. *ACS Nano* 2012, 6 (1), 671–676.

[4]. Jia, X.; Hofmann, M.; Meunier, V.; Sumpter, B. G.; Campos-Delgado, J.; Romo-Herrera, J. M., et al., Controlled formation of sharp zigzag and armchair edges in graphitic nanoribbons. *Science* 2009, 323 (5922), 1701–1705.

[5]. Xu, Q.; Wu, M. Y.; Schneider, Grégory F.; Houben, L.; Malladi, S. K.; Dekker, C., et al., Controllable atomic scale patterning of freestanding monolayer graphene at elevated temperature. *ACS Nano* 2013, 7(2), 1566–1572.

[6]. Huang, J. Y. Y.; Ding, F.; Yakobson, B. I.; Lu, P.; Qi, L.; Li, J. J., In situ observation of graphene sublimation and multi-layer edge reconstructions.

Proceedings of the National Academy of Sciences 2009, 106 (25), 10103–10108.

[7]. Qi, Z. J.; Daniels, C.; Hong, S. J.; Park, Y. W.; Meunier, V.; Drndic, M., et al., Electronic transport of recrystallized freestanding graphene nanoribbons. *ACS Nano* 2015, 9 (4), 3510–3520.

[8]. Barreiro, A.; Börrnert, F.; Rümmeli, M. H.; Büchner, B.; Vandersypen, L. M. K., Graphene at high bias: cracking, layer by layer sublimation, and fusing. *Nano Letters* 2012, 12 (4),1873–1878.

Chapter 6 Summary

In this thesis, we use in-situ TEM observation to characterize suspended graphene nanoribbon devices. The in-situ method enables us not only to clarify the electronic conductance properties of suspended GNR, but also to obtain valuable information to fabricate high quality GNR devices.

Chapter 1 introduces graphene and graphene nanoribbon, which is target material in this thesis. We explain the benefits and methods of using in-situ microscopy to study this material. In addition, a brief overview of recent experimental progress about in-situ electrical measurement of suspended GNR by transmission electron microscopy is shown in final part.

Chapter 2 contains all the experiment setup, the design of TEM holder and custom Si/SiN chip, the fabrication and characterization of suspended GNR devices. Here, the fabrication process is introduced in detail, including the evaporation of metal electrodes, cutting a spatial gap, transfer CVD-graphene and pattering to a ribbon.

Chapter 3 introduces several methods for cleaning the surface of GNR. Including: dry-cleaning with adsorbents (heating with active carbon), thermal annealing in vacuum by heating holder, two-step heating in gas environment (Ar/H_2), and in-situ current annealing (Joule heating), and applied them to our fabricated graphene devices.

Comparing all the methods, current induced-annealing is the most suitable and effective method for cleaning suspended GNR, which is helpful for the measurement of intrinsic electrical conductance properties and further nano-sculpting process.

Chapter 4 shows the nano-sculpting process and in-situ electrical measurements of suspended GNRs in TEM. The sculpting process of ribbon width separate into two steps: rough cutting by converged TEM electron beam (several hundred nanometer to ca.20-30 nm), precise thinning by the application of a high bias voltage (sub-10 nm). Then we investigated structure-dependent electronic properties of suspended GNRs by in situ TEM observation with simultaneous current-voltage curve measurements. During the GNR thinning process, the electrical conductivity changed from metallic to semiconducting behavior. When the width of GNR became very narrow (usually < 4 nm), the transport gap started to be opened. A transport gap of 300 and 700 meV is estimated for 1.5 nm wide AGNR and ZGNR, respectively. Most of important, the I-V curves for the ZGNRs were obviously different from those for the MGNRs and AGNRs, which support the previously reported current-driven magnetic-insulator and nonmagnetic-metal nonequilibrium phase transitions by application of a bias voltage.

Chapter 5 reports the restructure of GNR under applied bias voltage. We investigate the effect of different bias voltage on monolayer and few layer GNR devices. For a stable 1.0 V bias voltage applied on monolayer GNR, the voltage mainly influence the

edge structure of ribbon. The rough and curve edge restructure into straight and smooth edge, without changing the width of ribbon. When the increased high bias voltage was applied to monolayer or few layer GNR, it not only affect edge structure, but also width and layer number of ribbon. Under a high bias voltage, the thickness and width of ribbon shrinks sharply with the edge restructure at the same time. In addition, we found the conductance improved through structure recrystallization during reconstruction process, even with the decrease of ribbon width. This open a way for the fabrication of controlled width, layer number and smooth edge GNR devices with high conductance.

Appendix A

Here we shows the calculation method of the setting parameters of electrical conductivity under symmetric and asymmetric condition for the finite element thermal simulation, which has discussed in Chapter 3.5.4.

Firstly, the resistivity of clean monolayer graphene is calculated by removing the contact conducting from the measured total resistance. As we know, the total resistance (R_{TOT}) of GNR device is mainly consist of the contact resistance (R_C) and the resistance of clean GNR (R_G):

$$R_{TOT} = R_C + R_G \tag{A-1}$$

The resistance of clean GNR can be described as:

$$R_G = \rho_G \cdot \frac{L}{w \cdot d} \tag{A-2}$$

By the combination of (A-1) and (A-2), we obtained the relationship between total resistance and resistivity of clean graphene (ρ_G), as shown in (A-3):

$$R_{TOT} = R_C + \rho_G \cdot \frac{L}{w \cdot d} \tag{A-3}$$

Where R_{TOT} is the measured total resistance of GNR device, R_C is the contact resistance between GNR and Cr/Au electrodes, ρ_G is the resistivity of clean graphene, L and w is the length and width of suspended GNR between electrodes, respectively, d is the thickness of GNR which depend on the layer numbers. As shown in Chapter 4.3,

the value of contact resistance R_C can be obtained from the fitting function. For the sample shown in Figure 4.9 (a), the total resistance is measured as R_{TOT} = 5.2 kΩ, the fitting contact resistance is R_C = 2.8 ±1.4 kΩ, the length, width, thickness of suspended GNR is 123, 243, 0.335 nm, respectively. By this method, the resistivity of clean monolayer graphene is calculated as 1588 Ω·nm.

With this calculated resistivity of clean graphene, we could obtain the contact resistance value of any samples by subtracting the resistance of GNR from measured total resistance. By using this method, the contact resistances between suspended GNR and Cr/Au electrodes are calculated for both symmetric and asymmetric condition. For symmetric sample (Figure 3.12 (b)), the calculated total contact resistance is 18 kΩ. Since the contact condition between left and right side is same, the resistance for both side is 9 kΩ and the corresponding electrical conductivity is 0.198×10^5 S/m, as shown in Figure 3.13. The thermal conductivity of both side use the default value of gold electrodes, 317 W/m·K.[1] For asymmetric condition (Figure 3.12 (c)), the calculated total contact resistance is about 9.2 kΩ. As we assume the contact resistance of left side is 10 times larger than right side, the corresponding electrical conductivity of left and right side is 2.13×10^4 and 2.13×10^5 S/m, respectively. The poor contact condition between left side and GNR lead to the poor thermal diffusion, so the thermal conductivity of left side (31.7 W/m·K) is also set as one-tenth than that of right side

(317 W/m·K). The built model used for asymmetric condition is shown in Figure 3.14.

References

[1]. Sundar, L. S.; Singh, M. K., Convective heat transfer and friction factor correlations of nanofluid in a tube and with inserts: a review. *Renewable and Sustainable Energy Reviews* 2013, 20, 23-35.

Acknowledgements

First of all, I would like to express my deep and sincere gratitude to my supervisor, Prof. Yoshifumi Oshima. Without his strongly support and great encouragement and advice, I cannot finish this work successfully. He is such a kind person who will patiently encourage me to never give up, when my experiment is in trouble. With his care and support, I spend a great time through the doctoral program at JAIST.

Then I would like to express my deep gratitude to Prof. Xiaobin Zhang for strongly support of the operation and experiments in Tokyo Institute of Technology. Her nicely explanation and useful comments are helpful for improving my research.

I also would like to thank Prof. Hiroshi Mizuta and Lecture. Manoharan Muruganathan for kind support and guidance to do the experiment. They have taught me numerical techniques and kindly support related to simulation. Especially for Dr. Sankar in Mizuta lab, who contribute to the simulated temperature distribution of GNR device. Their generous support has had a remarkable influence on my progress in research.

I am thankful for Prof. Masahiko Tomitori for reading and giving me useful comments on my thesis.

I also thanks Prof. Masashi Akabori for supporting the fabrication of the GNR

devices, and assistance with the experimental operation and great experience to do the experiment.

I would like to express my appreciation to Ms. Mizutani and Mr. Okubo for preliminary work in 2016-2018 and Prof. Sannomiya for using R005 in Tokyo Institute of Technology.

I also thanks my fellow lab mates Ms. Chiew, Mr. Chen, Mr. Fukomoto and Mr. Xie for the kindly discussions and useful ideas when working together. Especially, I am greatly thanks to my husband Mr. Zhang for the designing of TEM holder and useful suggestions for improving my experiments.

I especially want to thank China Scholarship Council for financial support during my doctoral course.

I owe my loving thanks to my parents for encouraging and supporting me both economically and spiritually throughout my life.

Finally, I would like to express my gratitude again to all those who supported me to complete this dissertation and help me in life.

List of Publications

Relevant to this thesis

[1] Chunmeng Liu , Jiaqi Zhang, Muruganathan Manoharana, Hiroshi Mizuta, Yoshifumi Oshima, Xiaobin Zhang, “Origin of nonlinear current-voltage curves for suspended zigzag edge graphene nanoribbon.” Carbon. 2020, 165, 476-483.

[2] Chunmeng Liu , Jiaqi Zhang, Xiaobin Zhang, Muruganathan Manoharana, Hiroshi Mizuta, Yoshifumi Oshima, “The fabrication and in-situ electrical measurement of suspended graphene nanoribbon device in Transmission Electron Microscopy. ” (in preparation)

Presentation

- **International Conference (Poster)**

1. Ryo Okubo, Kanako Mizutani, Chunmeng Liu, Xiaobin Zhang, Marek E. Schmidt, Manoharan Muruganathan, Hiroshi Mizuta and Yoshifumi Oshima, "Electrical Conductance Measurement of Graphene Nanoribbons", 19th International Microscopy Congress (IMC19), 9 - 14 September 2018, Sydney, Australia
2. Chunmeng Liu, Ryo Okubo, Xiaobin Zhang, Marek E. Schmidt, Manoharan Muruganathan, Hiroshi Mizuta and Yoshifumi Oshima, "In-situ Electrical Conductance Measurement of Suspended Graphene Nanoribbon by Transmission Electron Microscopy", Asia conference on Nanoscience and Nanotechnology, 2018 (AsiaNANO 2018), 18-21 October 2018, China.
3. Chunmeng Liu, Ryo Okubo, Xiaobin Zhang, Marek E. Schmidt, Manoharan Muruganathan, Hiroshi Mizuta and Yoshifumi Oshima, "In-situ Electrical Conductance Measurement of Suspended Graphene Nanoribbon by Transmission Electron Microscopy", 10th International Conference on Materials for Advance Technologies, 2019 (ICMAT 2019), 23-28 June 2019, Singapore.

- **Domestic Conference (Oral)**

1. 大久保諒、水谷加奈子、刘春萌、張暁賓、シュミットマレク、ムルガナタンマノハラン、水田博、大島義文、“グラフェンナノリボン電気伝導計測のデバイス構造の作製”、日本顕微鏡学会第 74 回学術講演会、29 - 31 May 2018、福岡
2. 大久保諒、刘春萌、張暁賓、シュミットマレク、ムルガナタンマノハラン、水田博、大島義文、“透過電子顕微鏡その場観察によるグラフェンナノリボン電気伝導計測”、2018 年日本表面真空学会学術講演会、 19 - 21 November 2018、兵庫
3. Chunmeng Liu, Ryo Okubo, Xiaobin Zhang, Manoharan Muruganathan, Hiroshi Mizuta and Yoshifumi Oshima, “In-situ Electrical Conductance Measurement of Suspended Graphene Nanoribbon by Transmission Electron Microscopy”, The 80th Japan Society of Applied Physics Autumn Meeting 2019, 18-21 September 2019, Sapporo.
4. Chunmeng Liu, Xiaobin Zhang, Manoharan Muruganathan, Hiroshi Mizuta and Yoshifumi Oshima, “In-situ Electrical Conductance Measurement of Suspended Graphene Nanoribbon by Transmission Electron Microscopy”, Annual meeting of The Japan Society of Vacuum and Surface Science 2019, 28-30 October 2019, Tsukuba.

- **Domestic Conference (Poster)**

1. Chunmeng Liu, Ryo Okubo, Xiaobin Zhang, Marek E. Schmidt, Manoharan Muruganathan, Hiroshi Mizuta and Yoshifumi Oshima, “The Fabrication of Suspended Graphene Nanoribbon for In-situ Transmission Electron Microscopy Observation”, The 66th Japan Society of Applied Physics Spring Meeting 2019, 9-12 March 2019, Tokyo.